

## CHALLENGES IN SCIENTIFIC DATA COMMUNICATION FROM LOW-MASS INTERSTELLAR PROBES \*

DAVID G MESSERSCHMITT,<sup>1</sup> PHILIP LUBIN,<sup>2</sup> AND IAN MORRISON<sup>3,4</sup>

<sup>1</sup>*University of California at Berkeley, Department of Electrical Engineering and Computer Sciences, USA*

<sup>2</sup>*University of California at Santa Barbara, Department of Physics, USA*

<sup>3</sup>*Swinburne University of Technology, Centre for Astrophysics and Supercomputing, Australia*

<sup>4</sup>*Now with Curtin University, Curtin Institute of Radio Astronomy, Australia*

(Received February 2020)

Submitted to ApJ

### ABSTRACT

Near-term exploration of nearby star systems focuses on a swarm of low-mass probes accelerated to relativistic speed using propulsion from a terrestrial directed-energy beam. An optical downlink for the simultaneous return of scientific data from multiple probes at the distance of Proxima Centauri is studied. Transmission time/distance and probe mass are chosen to achieve the best data latency vs volume tradeoff. Challenges in targeting multiple probe trajectories with a single receiver are addressed, including multiplexing, parallax, and target star proper motion. Relevant sources of background radiation, including cosmic, atmospheric, and receiver dark count are identified and estimated. Direct detection enables high photon efficiency and incoherent aperture combining. A novel burst pulse-position modulation (BPPM) beneficially expands the optical bandwidth and ameliorates receiver dark counts. A receive aperture architecture combines minimum transmit power with constrained swarm-probe coverage. Theoretical limits on reliable data recovery and sensitivity to the various BPPM model parameters are applied, including a wide range of receive aperture areas. Such a downlink does not appear feasible with current technology. Enabling innovations include a high peak-to-average power ratio, a large source extinguishing factor, the shortest atmosphere-transparent wavelength to minimize target star interference, adaptive optics for atmospheric turbulence, very selective bandpass filtering (possibly with multiple passbands), very low dark-count single-photon superconducting detectors, and optical phased arrays for sky coverage shaping and coronagraph functionality.

*Keywords:* interstellar space probes, interstellar communication

## NOMENCLATURE

$x^{\{T,S,R\}}$	Design values of metric “ $x$ ” at {transmitter, receiver sub-array, entire receive aperture}
$\xi_{\{A,P\}}^T$	Probe transmitter {average, peak} power-area metric
$\xi_{\{A,P\}}^{TR}$	End-to-end {average, peak} power-area-area metric
$\Lambda_{\{A,P\}}$	Photon detection rate corresponding to {average, peak} signal power
$\Lambda_{\{N,I,D\}}$	Photon detection rate corresponding to background {noise, interference, dark counts}
Others	See Tbl.1 and Tbl.2

## 1. INTRODUCTION

Since exoplanets are commonplace, interest in and concrete efforts toward the scientific exploration of exoplanets are growing. This paper addresses the technology development challenges behind the goal of launching low-mass interstellar space probes to the vicinity of the nearest star system (Alpha Centauri) and returning the acquired scientific data before the end of the 21st century. Prominent among the myriad challenges are propulsion and communication. Here we address the communication of scientific data from a probe at interstellar distances and traveling at a relativistic speed.

First proposed by Robert Forward in 1962 (Forward 1962), a low-mass probe with a sail propelled by directed energy from earth is the only known technological option for close exploration of nearby stars that may be accessible with available or near-term technology, and which completes its mission in a matter of decades. This has led to concrete efforts to validate the concept and its supporting technology in the context of the NASA StarLight and Breakthrough StarShot programs (Lubin 2016; Kulkarni et al. 2017; Lubin et al. 2018a; Parkin 2018).

Such a probe achieves minimum mass (and hence highest velocity) by carrying only a sail for propulsion, scientific instrumentation, a downlink communications system, photon thrusters for attitude control, and an electrical power generator. Coupled with very high power directed energy beaming from earth and a sail that captures the momentum from that beam, it can reach 10-20% of light speed. Following a flyby (likely of Proxima Centauri or other targets within our stellar neighborhood), the probe would transmit the scientific data collected back to a receiver on the earth’s surface, which would consist of a large set of optical sub-arrays with incoherent combining. Location on the earth’s surface (rather than on a space-based platform) is motivated by the large dimensions of the directed-energy and receive infrastructures, and the large energy requirements for the former.

The focus here is on the probe-to-earth communication downlink design with the expectation that any earth-to-probe uplink communication is short-lived and benefits from relative proximity to earth. Relying heavily on a reusable fixed propulsion and communication

infrastructure confined to the earth’s surface, a swarm of multiple probes can be launched with a diversity of scientific instruments capturing images, magnetic field strengths, spectroscopy, etc.

We quantify the tradeoff between probe mass, speed and data rate, with the goal of minimizing the data latency, defined as the time from probe launch to the completion of the data download. As the total data volume is increased, the probe mass and latency necessarily increase, and speed decreases. Later numerical results focus on the lowest-mass “wafer scale” version.

Today most interest in interstellar exploration by space probes resides in the astronomy and astrophysics communities, but some essential knowledge and experience lies with the communications sciences. With the goal of informing all these communities and uniting them around this challenge, we are careful to define terminology and emphasize intuitive explanation rather than detailed derivation of theoretical results.

## 1.1. Goals

As of this writing it is early in the conception of the interstellar mission based on low-mass probes. The goal of this paper is *not* to propose a concrete and fully specified design for such a communication downlink, as there are too many uncertainties, interactions between launch and downlink communication, and questions about the technologies that may be available in the timeframe of the first operational downlink. An initial conclusion is that wavelengths in the visible optical regime are appropriate due to the severe transmit power and aperture restrictions. We propose an architecture that meets operational requirements. Within that architecture we study and quantify the inevitable dependencies and tradeoffs among the different components, and in general attempt to gauge the feasibility of the endeavor.

Because we can use higher power or larger apertures, the laws of physics do not limit the achievable distances or data rates. Rather, practical limitations are due to low probe mass and available technologies and their performance characteristics. Because probes will be launched in a couple decades at the earliest, and the beginning of downlink operation will be delayed for at least five decades (see §2.4), we don’t consider currently available technology to be limiting. Rather we identify the areas of greatest technological challenge, and identify new capabilities that are needed. This mission can leverage general technology advances over the coming decades, but may also require specific technological innovation and development. We also identify and discuss tradeoffs among technologies, and assume that greater advancement in some areas can offset slower advancement in others.

Thus we can identify the specific goals of this paper as:

- Identify the physical limitations on such a mission, especially those related to the space environment

(such as unwanted sources of noise and interference).

- Propose a system architecture, within which we identify the system components and quantify needed capabilities.
- Understand the interactions and tradeoffs among those components.
- Identify components where currently available technology is inadequate and estimate the necessary future capabilities. A more concise summary of these technology inadequacies is available (Messerschmitt et al. 2019).
- Generally assess the feasibility of the endeavor in the envisioned timeframe.

Implementation and practice always brings some bad news. While we attempt to anticipate the greatest challenges that will be encountered, we do not attempt to accurately predict an actual deployed system performance. Thus, the results here always fall on the idealistic side. One of the goals of any subsequent technology development will be to come as close to these ideals as possible.

### 1.2. Related work

Most effort and publication devoted to low-mass probes has emphasized the challenges of propulsion by directed energy and light-sail (Hoang et al. 2017; Heller & Hippke 2017a,b; Heller et al. 2017; Hoang & Loeb 2017; Heller 2017a) and (Hoang 2017; Gros 2017; Forgan et al. 2017; Atwater et al. 2018).

In some ways this challenge mirrors the extensively studied requirements for interplanetary spacecraft communication within our solar system (Hemmati 2006, 2009). The substantial differences include the severe limitations on the probe’s available electrical power, processing, and transmit optics, as well as the much greater propagation loss, different sources of background radiation, ground-based reception with many issues related to atmospheric turbulence, scattering and weather, and the expectation of a swarm of probe downlinks operating concurrently.

Space communication applications have stimulated extensive research and engineering into long-distance free space optical communication. Results most relevant to the present challenge come from JPL’s interplanetary network (IPN) (Dolinar et al. 2012b). This includes an encouraging laboratory demonstration of high photon efficiency in a communication link with insignificant background radiation (Farr et al. 2013).

Interstellar communication differs from terrestrial communication in its emphasis on energy efficiency rather than spectral efficiency. At radio wavelengths, energy-efficient interstellar communication has been studied in the context of METI/SETI (Messerschmitt

2013, 2015). What is different about space probes is the feasibility of transmitter-receiver coordination in the interest of achieving high photon efficiencies to help overcome power/size/mass limitations.

The germane sources of optical-wavelength background radiation for interstellar communication are a current area of research (Lubin et al. 2018a). These background calculations have been independently quantified in (Hippke 2017a), which quantifies the ultimate quantum limits on communication. The present paper addresses what is achievable in practice with existing or foreseeable technologies.

This paper expands and refines our own earlier effort (Lubin et al. 2018c). Here we explore a probe-swarm or single-probe receiver that achieves the minimum transmit power-area product in the interest of minimizing probe mass by operating near the physical limits of the received-signal noise floor. We also explore the implications of varying aperture area over a wide range. A recent paper (Parkin 2019) addresses the same application but addresses only the single probe case (requiring complete receiver duplication for each probe in a swarm) and focuses on minimizing receive aperture area rather than probe mass (see §6.9.1).

## 2. SYSTEM CONCEPT

We now review the overall low-mass system with an emphasis on those components relevant to the communications downlink.

### 2.1. Numerical parameters

Tbl.1 and Tbl.2 are guides to notation combined with numerical values for a nominal design based on a specific modulation coding assumption (see §6.8). We use a superscript notation for the same parameters as measured in the transmitter (a ‘T’) and at two points in the receiver, at the sub-array (an ‘S’) and at the overall receive aperture (an ‘R’) (see §2.9). Assumed numerical parameters are merely reference points and do *not* carry the weight of design objectives. This would be premature, as there are many design and technology issues and interactions among various system components that will weigh heavily on the final design. Consonant with our goals (see §1.1) these choices serve to gauge the realism (or lack thereof) of the system design using an idealized model that ignores many practical challenges that will undoubtedly arise. More importantly, scaling relationships that follow from varying these parameters are emphasized (both theoretically and numerically) to appreciate the implications of changing assumptions.

### 2.2. Scientific objective

Individual probes may carry different types of scientific instrumentation, subject to severe mass limitations. The primary relevance of the scientific objective to the downlink design is the total data volume  $\mathcal{V}$  to be down-

**Table 1.** Scientific data and modulation parameters

	Description	Value
$\mathcal{R}_0$	Nominal data rate immediately following encounter during non-outage periods (b/s)	1.
$R_o$	$R_0$ reduced to account for outages (b/s)	0.432
SBR	Average signal to average background photons during non-outage PPM frames	4
$m$	Bits per PPM frame	12
$M$	Slots per PPM frame	4096
$T_s$	PPM slot duration ( $\mu$ s)	0.1
$T_F$	PPM frame duration (ms)	0.41
$T_I$	Inter-PPM-frame interval (s)	2.2
$J_p$	Probes concurrently transmitting	26
$T_L$	Latency of total data return (yr)	28.
$\mathcal{V}$	Volume of total data (Mb)	28.9
$L$	Volume of data segment (Mb)	1.0
$P_c$	Probability of correct segment recovery	0.99

**Table 2.** Physical parameters and performance metrics

	Description	Swarm	Single
$A_e^T$	Effective transmit aperture area (cm <sup>2</sup> )	100	
$\Omega_A$	Coverage solid angle (arcsec <sup>2</sup> )	10.	0.01
$\zeta$	Probe mass ratio	1.	
$\lambda_0^R$	Received optical wavelength (nm)	400	
$P_W$	Probability of weather outage	0.1	
$P_D$	Probability of daylight outage	0.52	
$\eta$	Optical detector efficiency	1.0	
$K_s^R$	Avg. detected signal photons per PPM slot	0.2	
BPP	Non-outage photon efficiency (b/ph)	10.9	
$P_A^T$	Avg. transmit power (mW)	29.4	0.8
$P_P^T$	Peak transmit power (kW)	638.	17.4
PAR	Peak-to-average ratio	4096.	
$\rho_M$	Reduction in moonlight irradiance relative to full moon	1	
$\Lambda_D^S$	Avg. rate of dark counts referenced to each sub-array (ph/yr)	32.0	
$F_x$	Optical source extinction ratio	$10^{-7}$	
$F_c$	Receive coronagraph rejection	0.01	
SXR	Signal-to-extinction ratio	2441.	
SIR	Signal-to-interference ratio	152.	4.15
SNR	Signal-to-noise ratio	8.3	226.
SDR	Signal-to-dark count ratio	8.2	223.
$A_e^S$	Effective receive sub-array area (cm <sup>2</sup> )	6.8	6807.
$N^S$	Number of receive sub-arrays	$5.9 \cdot 10^7$	$2.2 \cdot 10^6$
$A_e^S N^S$	Total effective aperture area (km <sup>2</sup> )	0.04	1.47
$W_e$	Effective optical bandwidth (MHz)	10.	
$u_0$	Probe speed ( $c$ )	0.2	
$D_{\{0,1\}}$	{Start,end} of downlink propagation distance (ly)	{4.24, 4.66}	

loaded<sup>1</sup> and the reliability with which that data is recovered. These two parameters are certainly related to the type of instrumentation carried by a probe. Early missions are likely to emphasize imaging, so this is the application addressed in our examples.

<sup>1</sup> We measure  $\mathcal{V}$  in bits (b) rather than bytes (B). For example,  $10^6$  bits (125 kilobytes) is written as 1 Mb.

For purposes of reliability, scientific data can be divided into *segments*, each with volume  $L$ . It is the reliability of recovery of each segment at the receiver that is of greatest interest. For example, for an imaging mission a segment would be one image (2-D representation in terms of matrix of pixels), and we assume  $L = 1$  Mb (megabits).<sup>2</sup> A segment is either recovered correctly in its entirety or corrupted in some fashion due to one or more bit errors.<sup>3</sup>  $P_c$  is the probability that a single segment is recovered correctly in its entirety.

### 2.3. Launch and propulsion

The goal of acquiring scientific data from instrumentation in proximity to even nearby stars within the 21st century requires probes that reach a significant fraction of the speed of light  $c$  (Heller 2017b). For example, the distance to the nearest star (Proxima Centauri) is 4.24 ly, and the probe transit time at 20% of  $c$  is 21.2 yr. If a probe transmits data beginning immediately after encounter with that star and its exoplanets, the data would begin to reach earth 25.44 years after launch. We define the *data latency*  $T_L$  as the total time elapsed on earth until the entire data volume  $\mathcal{V}$  is received, which includes the transit time, the transmission time, and the signal propagation time from the farthest reaches of transmission (see §C). Minimizing  $T_L$  subject to a constraint on  $\mathcal{V}$  is a potential approach to determining the best choice of probe mass (see §3).

### 2.4. Timeline

Some significant technology advances are needed to ensure success with something approximating the parameters of Tbl.2. It is fortunate that there is considerable time available to benefit from the ongoing evolution of technology. There is also the opportunity to target certain technologies for faster advances targeted on the needs of this application and interstellar exploration more generally. Transmitter technologies must be finalized before the first launch (perhaps 1-3 decades). An operational receiver need not be deployed to access the initial downloaded scientific data until 25+ years following first launch for a speed of 20% of  $c$ . Thus for the receiver we can assume at least 4-5 decades of technology advancement and development.

#### 2.4.1. A swarm of probes

The project budget will be heavily concentrated in the terrestrial launch and communication infrastructure. The incremental cost of each probe launch is not significant in comparison (Parkin 2018), suggesting the repeated launching of probes. Such a swarm of probes

<sup>2</sup> This will accommodate a  $1000 \times 1000$  set of pixels at one bit per pixel following compression.

<sup>3</sup> After compression, even a single bit in error often propagates across the image and thus has serious consequences.

can increase the scientific return by following different trajectories near the target star, providing redundancy to account for navigational errors on individual probes, and carrying a diversity of scientific instruments.

Because the cost of the receiver system is likely to be large, our primary analysis focuses on a single receiver shared among all the concurrent downlinks. This causes serious complications in the design and operation of the terrestrial receiver infrastructure and is a major concern addressed in the following. Operation of a receiver for a single downlink (or multiple receivers, one for each downlink) is addressed as a special case (as in (Parkin 2019)).

### 2.5. Communications downlink

This paper focuses on the communications downlink returning scientific data to earth. We assume a terrestrial receiver (as opposed to space-based) for cost and operational reasons. The atmosphere is suitably transparent at microwave and visible-infrared optical wavelengths, so we could choose either. Considerations of transmit and receive aperture areas in combination with interstellar distances make optical the only feasible choice (see §4). The large target star emissions adjacent to probe trajectories favor the shortest wavelength for which the earth’s atmosphere is transparent (see §6.8). Thus we assume  $\lambda_0^R=400$  nm in Tbl.2, but also compare this to  $1\ \mu\text{m}$  in the numerical results.

#### 2.5.1. Probe trajectories and receiver coverage

Our receive aperture does not attempt to image the swarm of probes (since their trajectories are similar) but rather captures a superposition of their signals. (In this respect, it can be thought of a single-pixel optical telescope.) The coverage of a terrestrial receiver is defined as the solid angle  $\Omega_A$  over which transmitted probe signals are recovered with nearly equal sensitivity.<sup>4</sup> To accommodate a swarm of probes with a single receiver,  $\Omega_A$  has to be considerably larger than it would be for a single probe. An increase in  $\Omega_A$  results in an inevitable decrease in receiver sensitivity (see §2.10.1).

The trajectories of different probes in a swarm are illustrated in a simplified schematic 2-D form in Fig.1. There are five phases to each individual probe mission: launch of the probe, transit to the neighborhood of the target star, encounter with that star (observations and scientific data collection), downlink operation (transmission of that scientific data to earth), and finally permanent probe silence.

Shown specifically are four probe trajectories at the most extreme angles, taking into account orbital differ-

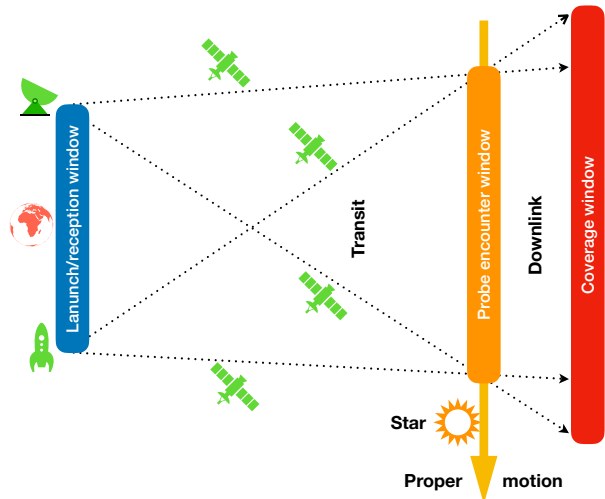


**Figure 1.** A 2-D schematic representation of the 4 most extreme probe trajectories as viewed from earth. The launch/reception window captures the seasonal variation in earth’s position, and the probe encounter window captures the proper motion of the target star. As shown all encounters are assumed to fall on the same side of the target star, which moves away from the encounter positions. Downlink operation follows encounter. Receiver coverage is assumed to cover all concurrently-transmitting probes, and a coronagraph function takes advantage of spatial separation to reject a portion of the target star’s radiation.

ences between launch and reception coordinates as well as the proper motion of the target star (both of which are exaggerated in scale). Of greatest concern for receiver design are the relative variations in the positions of the different probes and the target star, which determine the required spatial coverage of the receiver and the coronagraph rejection (see §2.10.1). There are two primary influences:

- A single probe’s apparent position varies due to the parallax effect of the earth’s orbital motion.
- The target star’s proper motion (movement in relation to the galactic background) implies that different probe encounters are spatially separated (Parkin 2019). These probe encounter positions trail behind the moving star, resembling the tail of a comet.

#### 2.5.2. Source of electric power

A probe launched with directed energy and cruising at constant speed following launch requires no propulsion. Electrical power is nevertheless necessary for probe attitude control, scientific instruments, and downlink communications (Landis 2019). Examples of power sources include a radioisotope thermoelectric generator (RTG)

<sup>4</sup> Coverage is similar to the field-of-view of a single-pixel optical telescope, or the resolution of a single pixel in a multiple-pixel imaging telescope. In contrast to optical telescopes, the coverage that results from the beamforming of an optical phased array can be non-circular in shape.

or forward-edge ISM proton-impact conversion during the cruise phase (before and after encounter) with the possible addition of photovoltaic power from the target star during the encounter. At relativistic speeds the latter will be short-lived (on the order of hours), but may be valuable for scientific instruments, as well as the processing for data compression, outage mitigation (see §10.4) and error-control coding (see §10.3).

### 2.5.3. Multiple-probe multiplexing

The transmit signals from a concurrently transmitting swarm of probes are superimposed during propagation and must be separated on the receive side. This *multiplexing* function is arguably the most critical design choice, since it interacts with virtually every part of the downlink design. The basis for separation can be spatial, wavelength, time, or code (see §8.2).

### 2.5.4. Heterodyne vs direct detection

There are two common ways to detect the optical signal from a probe in the receiver. *Heterodyne* mixes that optical signal with a local oscillator (LO), and optical square-law detection results in components of sum and difference frequencies as well as amplification. The difference-frequency component can fall at a microwave wavelength. Here we adopt (for reasons explained in §2.6) the alternative of *direct detection*, which eliminates the LO and relies on single-photon counting detectors.

Heterodyne would offer some compelling advantages. In addition to amplification as a part of optical detection, channel separation and bandpass filtering can be performed using available microwave technologies. It also opens up a wider class of modulation schemes based on the phase as well as magnitude of the incident wavefront.

At optical wavelengths (where the energy per photon is significantly higher) individual photons can be directly detected, although due to quantum effects the number of photons detected per unit time is only stochastically related to the receive power. The result is signal self-noise (sometimes called *shot-noise* or *quantum noise*). When a large signal-to-background ratio (SBR) is assumed, this shot noise becomes the dominant source of errors in the data recovery. A critical advantage of direct detection is the construction of very large receive apertures based on the incoherent combining of sub-arrays (see §2.10).

### 2.6. High photon efficiency

One motivation for adopting direct detection is the higher photon efficiency that can be achieved, which results in a reduction in the receive aperture total area. This is of practical significance because an aperture will likely be kilometer-scale. If the rate at which data is reliably recovered is  $\mathcal{R}_0$  b/s and the receiver average photon rate is  $\Lambda_A^R$  ph/s, photon efficiency BPP (in b/ph) is

defined by

$$\mathcal{R}_0 = \text{BPP} \cdot \Lambda_A^R. \quad (1)$$

Due to excess shot-noise introduced by the high-power LO, heterodyne cannot achieve a comparable BPP to direct detection. The theoretical limit is  $\text{BPP} < \eta / \log 2 = 1.44\eta$  b/ph for detector quantum efficiency  $\eta$  consistent with reliable data recovery (Gordon 1962), while direct detection introduces no theoretical limit. The assumption in Tbl.2 is  $\text{BPP}=10.9$  b/ph. This is consistent with a laboratory demonstration of  $\text{BPP} = 13$  b/ph (Farr et al. 2013). The significant photon efficiency advantage of direct detection makes it worthwhile to overcome the technological challenges it introduces, which is our focus here.

### 2.7. Probe transmitter

Scientific payload data is embedded in the transmitted optical signal power vs. time by the modulation. We propose *burst pulse-position modulation* (BPPM), which can achieve the required efficiency while compatible with the imposed constraints (see §2.12).

In BPPM a semiconductor laser in the transmitter generates short pulses of light intensity with a duration on the order of 0.1 to 1  $\mu\text{s}$  with a repetition rate of about 1-2 Hz. Scientific data is supplemented by error-correction redundancy and then imposed on the pulses by adjusting their timing (see §2.12 and §10). The average power is  $P_A^T$ , on the order of 1–100 mW, with a peak transmitted power  $P_P^T$  that is about  $10^6$  larger.<sup>5</sup> The intensity-modulated light is emitted in the direction of earth by a transmit aperture with effective area  $A_e^T$  (the concept of effective area is discussed in §B). Accurate attitude control based on photon thrusters is necessary to ensure that the earth-based receive aperture is illuminated with the maximum power (see §8.5).

The probe incorporates processing to compress scientific data and perform the coding side of error-correction coding (ECC, see §10.3). In addition, it performs data interleaving and adds additional redundancy to counter outages resulting from daylight and weather events (and possibly other sources) at the earth-side receiver (see §10.4).

The probe-to-earth distance increases up to 10% during the operation of the downlink, which may last from 2–9 yr (see §3). Accommodation of increasing propagation distance requires the data rate  $\mathcal{R}$  to be reduced by slowing the rate of transmitted pulses and increasing the peak transmitted power (by a maximum of about 20%) to maintain fixed average power.

### 2.8. Background radiation

For a given transmit power and transmit/receive apertures, the initial data rate  $\mathcal{R}_0$  that can be achieved con-

<sup>5</sup> This description is oversimplified, as achieving a  $P_P^T$  this large will require a more complicated optical arrangement (see §9.1).

sonant with a sufficiently high signal-to-background ratio (SBR) is limited by the sources of background radiation. No matter how large SBR, signal shot noise remains as a limitation on the reliability with which the scientific data can be recovered (see §10).

Four distinct types of background radiation can be identified:<sup>6</sup>

- Imperfect *laser extinction* at the transmitter during intervals where zero power is sought will result in unwanted photon counts at the receiver (see §9.1).
- *Noise* is radiation that cannot be separated from the data signal because of its time, wavelength, and spatial overlap. In the current application such radiation is broadband, and must be reduced by limiting the optical bandwidth. Significant sources of noise are the cosmic background radiation, the deep star field, zodiacal radiation, and scattered sunlight and moonlight from the earth's atmosphere.
- *Interference* is unwanted radiation which is distinguishable from the data signal in one or more physical parameters (time, wavelength, or spatial) and can therefore be partially or wholly rejected by technological means. The major interference considered here is radiation from the target star, which is spatially separated from the probes, but which may be challenging to reject because of its close proximity to the probe trajectories.
- *Dark counts* mimic detection of photons originating from sky or cosmic sources, but originate within the receiver and would be present even if all incident light radiation were blocked from the receiver.

Incomplete extinguishment and dark counts generally cannot be limited by bandpass filtering (with the exception of black body radiation in the optics). Numerical calculations suggest that operation during periods of sunlight is not feasible, and with that assumption interference, scattered moonlight, and dark counts are the limiting factors placing a lower bound on the probe's transmit power (see §6.8).

### 2.8.1. Signal-to-background ratio (SBR)

SBR at the receive aperture output is  $\Lambda_A^R/\Lambda_B^R$ , where  $\Lambda_A^R$  is the average rate of signal photons and  $\Lambda_B^R$  is the accumulated average photon rate for all sources of background radiation. Our goal is to achieve an SBR suffi-

ciently large that background radiation has limited impact on data reliability. The impact of SBR is measured by the theoretical effect on BPP (see §E). With the goal of limiting background to a minor impact we choose SBR=4 in Tbl.2. This results in a 5% reduction in the theoretically obtainable BPP as compared to SBR= $\infty$ . Achieving a specific SBR places a lower limit  $\Lambda_A^R > \Lambda_B^R \cdot \text{SBR}$  on the received signal average photon rate  $\Lambda_A^R$ , and hence a lower bound on average transmit power  $P_A^T$ .

### 2.9. Downlink receiver

The major element of the receiver is the receive aperture, which is similar to a single-pixel optical telescope. It consists of a large number of sub-arrays, each with a dedicated optical detector that responds to individual photons from the incident radiation (background as well as signal) and introduces spurious dark counts as well (see §2.10). Thus no coordination or optical phasing of sub-arrays is necessary. It would be advantageous to share optical detectors over multiple sub-arrays if optical interference can be avoided (see §2.10.4). In contrast to an optical telescope, the optical path includes a highly selective optical bandpass filter that eliminates most out-of-band background radiation (see §9.2), and may serve to separate the signals from the individual probes as well (see §8.2.2). Photon detection events are logged at the individual sub-apertures, accumulated over a network, and a post-processing stage interprets the totality of photon events to reliably recover the scientific data. This architecture is now described in greater detail.

### 2.10. Receive aperture

The receive aperture in a direct-detection receiver includes the optics and photonics necessary to capture the power of an incoming electromagnetic wave and convert it to a digital representation of individual photon detection events. The receive aperture will be quite large, and is thus a major capital and operational cost.

The receive aperture must meet some challenging requirements:

- Accurate pointing toward the target star and swarm of probes has to be maintained in the face of earth orbital dynamics and atmospheric refraction.
- Both the total geometric size (physical dimensions) and total collection area are large as required to achieve a receiver sensitivity that accommodates severe limitations on the probe due to its mass restriction; namely, transmit power and transmit aperture size. A distinction between size and area is needed because the receive aperture is not likely to be filled.
- Achieve a coverage solid angle  $\Omega_A$  which is relatively large (but no larger than necessary) and

<sup>6</sup> These are terms commonly used in the communications literature. We adopt them here because (a) they are descriptive of these types of impairments and (b) because design techniques are adopted from the communication literature.

has an atypical elongated shape in the direction of the target star’s proper motion (see §2.5.1).

- It will likely incorporate adaptive optics to compensate for atmospheric seeing conditions (see §7).
- Separation of signals from different probes in the optical domain is required for some approaches to multiplexing signals from different probes, such as WDM (see §2.5.3).
- Whatever means possible should limit the background radiation. This includes optical bandpass filtering (see §9.2), rejection of interference with coronagraph functionality (see §8.6), and modulation design to limit dark counts (see §2.12).

### 2.10.1. Sub-arrays

A large size (kilometer scale) of the receive aperture as a whole is required to achieve low transmit power with adequate signal level to counter shot noise. If such an aperture was single mode (a single optical detector) and diffraction-limited, not only would its coverage solid angle  $\Omega_A$  be too small to cover a swarm of probes, but adequate pointing accuracy to track a single probe would be practically unrealizable. These challenges dictate that the aperture be decomposed into a large number  $N^S$  of smaller sub-arrays as shown in Fig.2. Each sub-array (which is further decomposed into a phased array of sub-aperture’s as described shortly) may have a dedicated optical detector responsible for generating a single stream of photon detection events in response to the incident electromagnetic radiation.

Each sub-array is required to achieve all the objectives of the receive array as a whole except a sufficient photon rate to support the desired data rate. In particular, the sub-array accurately points at the coverage window as pictured in Fig.1, achieves the desired  $\Omega_A$ , and achieves a required SBR.

Sub-array sensitivity is quantified by its equivalent area  $A_e^S$  (defined as the ratio of the intensity of an incident plane wave to detected power). This determines the required transmit power in the probe and the order  $N^S$  of scale-out. Although we like a larger  $A_e^S$ , in fact it is predetermined by the relationship between  $A_e^S$  and coverage<sup>7</sup>  $\Omega_A$ . In §B this relationship is determined in (B6) to be  $A_e^S \propto \Omega_A^{-1}$ . Larger coverage, as dictated by our requirement to service a swarm of probes with a common receiver, implies reduced sensitivity.

Each sub-array is responsible for limiting noise and interference via an optical bandpass filter (see §9.2) and

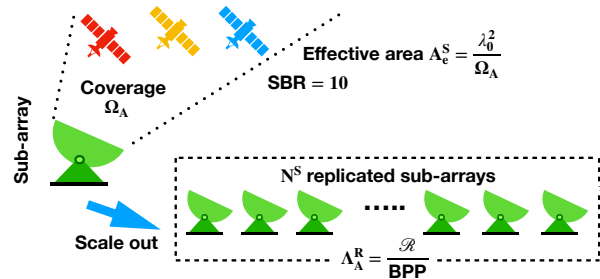


**Figure 2.** The receive aperture is composed as an  $N^S$ -way scaling out of a basic sub-array. The design of a sub-array focuses on achieving the maximum and uniform sensitivity to the signals from all probes in a swarm across a coverage solid angle  $\Omega_A$ , and has effective area  $A_e^S$ . It is also responsible for achieving a sufficiently large SBR to achieve the target BPP, and may also be responsible for separating the signals from different probes. The  $N^S$  sub-arrays independently capture and log photon detection events, with their only coordination a common clock for time stamps. The resulting incoherent accumulation of the incident optical power at each sub-array achieves a sufficient average photon detection rate  $\Lambda_A^R$  to recover the scientific data at rate  $\mathcal{R}$ , while influencing neither the coverage nor SBR.

coronagraph functionality (see §8.6). Accounting for a non-ideal filter, define the *effective bandwidth*  $W_e$  of a bandpass filter as the ratio of output power to input power spectral density (assumed to be constant). If the transfer function is  $H(f)$ , then

$$W_e = \int_0^\infty |H(f)|^2 df, \quad (2)$$

in which case  $W_e = W$  for an ideal bandpass filter with bandwidth  $W$ . More generally  $P \cdot W_e$  is the filter output power for a constant spectral density input  $P$ . The dark count rate for its optical detector should be as small as technology allows (see §9.3). The coronagraph partially rejects interference from the target star by exploiting its small angular separation from the probe trajectories.

Within the context of a specific sub-array design, including particularly sensitivity, coverage, coronagraph rejection, and dark count rates, the probes are responsible for a sufficiently large power-area metric  $\xi_A^T = P_A^T A_e^T$  and pointing accuracy to achieve the desired SBR (see §6.1). There is thus a tradeoff between  $P_A^T$  and transmit aperture effective area  $A_e^T$ .

### 2.10.2. Sub-array scale out

The sensitivity of a single sub-array is limited by its coverage requirement, and thus the average photon rate at the sub-array  $\Lambda_A^S$  will be far too small to support the desired data rate in (1). This limit on sensitivity can be overcome by the  $N^S$ -way replication of sub-arrays as pictured in Fig.2. This is called a *scale out* because the

<sup>7</sup> Each sub-array qualifies as an ‘antenna’ that is subject to the theory of §B assuming it is single mode (has a single optical detector) and diffraction-limited. This sensitivity-coverage relationship is based on the simplifying assumption (which can be approximated in practice) that the sensitivity is uniform over solid angle  $\Omega_A$  and zero elsewhere.

photon counts increase linearly with  $N^S$ .<sup>8</sup> The desired  $\Lambda_A^R$  determines the value of  $N^S$ , which is typically quite large (on the order of  $10^8$ – $10^9$ ).

Since the receive aperture as a whole has  $N^S \gg 1$  optical detectors that are incoherently combined, it is not an antenna in the sense of §B and thus the concept of effective area  $A_e^R$  does not apply. Instead we use area metric  $N^S A_e^S$ , which equals the total effective area accumulated over the sub-arrays, and gives us a sense of the total geometric area.

Scale out does not compromise the objectives in the sub-array design; namely, coverage and minimum SBR. The incoherent accumulation of photon rate across sub-arrays accumulates background photon rates in proportion to  $N^S$ , and thus the aggregate SBR is the same as the SBR at the output of each sub-array. Similarly  $\Omega_A$  is determined by  $A_e^S$  alone, and is unchanged by the incoherent combination of multiple sub-array outputs. If a single optical detector is shared over multiple sub-arrays, optical interference among those sub-array signals must be avoided to prevent inadvertent modifications to the coverage pattern (see §2.10.4).

### 2.10.3. Post processing

A more detailed picture of scale out as well as sub-array decomposition into smaller sub-aperture's is shown in Fig.3. Each sub-array not only detects individual photons, but it logs those photon-detection events as a time-stamp and, if the sub-aperture performs demultiplexing, a probe identifier. There being no need for real-time processing of these events, they can be shared in a common post-processing stage in which timing recovery is performed followed by scientific data extraction from the photon events. A permanent stored log of photon events (probe-number and time-stamps) also constitutes the permanent scientific record of a swarm of probe missions.

The collection of sub-arrays operate independently. There is no attempt to align the phases among individual sub-array's; indeed, the sub-array's each have their own optical detector which captures the power of the incident radiation to that sub-array, so all phase information has been deliberately discarded. This arrangement is colloquially called 'photon buckets'. The relative placement of sub-arrays is somewhat flexible, allowing for geographic distribution and relative placement for the convenience of construction or maintenance, although atmospheric turbulence will penalize a larger size (see §7.3). Placement of sub-arrays divided among a set of one or more independent space platforms is also an intriguing possibility.

<sup>8</sup> 'Scale out' is an engineering term referring to an  $N^S \times$  replication with a performance that increases proportionally to  $N^S$ . In this case 'performance' is measured by sensitivity of the receiver while maintaining fixed coverage and SBR.

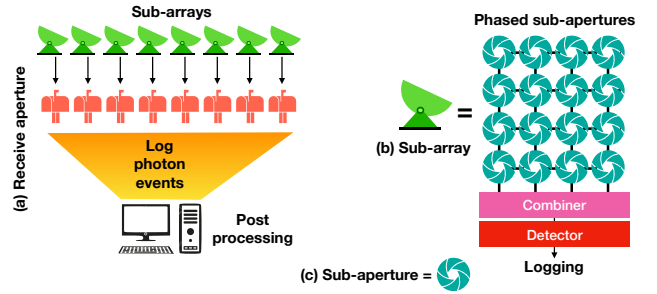


**Figure 3.** A schematic of a three-level receive aperture decomposition. (a) A collection of sub-arrays independently log photon detection events, and in a post-processing stage the aggregate events are processed to recover the scientific data originating in multiple probes. (c) Each sub-array is composed of a set of phased sub-aperture's with a combiner including precision phase shifts feeding a single optical detector. (To contain costs and reduce dark count rates, optical detectors may be shared across sub-array's in such a way that interference is not created, as long as interference between sub-aperture's is avoided.) (c) Each sub-aperture is an optical element (composed of lenses or reflectors).

The sub-arrays all connect to a communication network for distribution of target coordinates (which change at a slow rate), consolidation of photon events for processing, and status updates. The total number of events to be logged across all sub-arrays is of order  $0.1 \text{ s}^{-1}$  for each probe for the parameters of Tbl.2, so the storage and communication requirements are readily achieved.

The synchronization of time stamps across sub-arrays must be maintained, and this requires a common time reference (Messerschmitt 2017). The precision has to be a fraction of  $W_e^{-1}$  where  $W_e$  is the optical bandwidth of the signal. It is likely that the time-distribution service of GPS satellites combined with accurate knowledge of individual sub-array location coordinates would provide sufficient timing precision.

### 2.10.4. Shared optical detectors

One troublesome feature of Fig.3 is the  $N^S$ -way duplication of optical detectors, which multiplies the dark count rate by the same factor and imposes a very strict requirement on individual detector dark counts. Sharing of a single optical detector over multiple sub-arrays would reduce the overall dark count rate, as well as reduce the cost and complexity of the scale-out function. However to avoid any impact on the coverage pattern of the overall receive array, any interference in the optical domain among sub-array signals would have to be avoided (see §9.3).

### 2.10.5. Summary

The two-level hierarchy of sub-arrays combined with scale out to a full aperture is required to *simultaneously* achieve a desired (non-zero) coverage  $\Omega_A$ , a desired SBR, and a desired sensitivity (signal photon rate  $\Lambda_A^R$ ).<sup>9</sup> The consequence of covering multiple probes with a single receiver is inevitably a larger  $\Omega_A$  and hence a higher  $P_A^T A_e^T$  product for each probe. A desirable feature of this architecture is that the difficult technological challenges are confined to the sub-array realization, while the large number  $N^S$  of sub-arrays is primarily a budgetary and operational issue.

### 2.10.6. Phased sub-aperture's

The architecture of Fig.3 anticipates that the sub-arrays are themselves composed of phased sub-apertures. Each sub-aperture is envisioned as an (ideally) diffraction-limited monolithic optical element, which may be constructed from a lens or reflector. Following a combiner, these sub-apertures share an optical detector. Within the combiner the magnitude and phase for each sub-aperture optical signal as it arrives at the detector must be precisely controlled. The relatively small effective area  $A_e^S$  of the sub-array make this technically feasible, and indeed for the values in Tbl.2 it may not even be necessary. Depending on the sub-array dimensions an adaptive-optics component to compensate for atmospheric turbulence may be needed (see §7).

There are several requirements that suggest the use of a phased sub-aperture: A coverage pattern with solid angle  $\Omega_A$  that may be non-circular in shape, a coronagraph function which realizes a null in the overall sensitivity pattern at the angle of the interfering target star, and adaptive optics.

### 2.11. High photon efficiency and peak power

There are two impairments that limit the photon efficiency BPP that can be achieved. The first is background radiation, the impact of which is limited by placing a theoretical lower bound on SBR (see §E). The quantum efficiency  $\eta$  of the entire optical path reduces signal, noise, and interference equally, but does not affect the rate of dark counts. Thus its effect on SBR is only through the dark count component of background, and  $\eta < 1$  renders dark counts relatively more important. Because the  $\eta$  achievable decades from now is uncertain, our nominal assumption is  $\eta=1$  together with a sensitivity analysis.

Once background radiation is rendered insignificant, signal shot noise determines a theoretical upper bound on BPP. High BPP with reliable data recovery is achieved by judicious choice of the mapping from scientific data

to light intensity vs time in the transmitter (see §2.12) and error-correction coding (see §10.3). Regardless of how these are structured, there is a theoretical limit on the shot-noise-limited BPP that can be achieved in conjunction with reliable recovery of the scientific data. For large SBR this limit is

$$\text{BPP} < \log_2 \text{PAR}, \quad (3)$$

where PAR is the peak-to-average power ratio (see §E). Thus to achieve BPP=10.9 in Tbl.2 we must have, at minimum,  $\text{PAR} > 2^{10.9}$ .

High PAR is beneficial to photon efficiency, but it does have implications for the peak transmit power  $P_P^T$  required in the transmitter (see §9.1). A high peak power also requires short-term energy storage and possibly voltage conversion in the probe, since electric power is likely to be generated continuously (see §2.5.2).

PAR and optical bandwidth  $W_e$  are related in a subtle but significant way. A larger PAR is inevitably associated with a larger  $W_e$ , since it requires relatively high-energy pulses with short duration and low duty cycle. A larger  $W_e$  is beneficial in reducing the required selectivity of the receive optical bandpass filters. A larger  $W_e$  would also appear to admit more background radiation to the optical detector, thereby decreasing SBR. This is not entirely the case as now shown.

### 2.12. Burst pulse-position modulation

The modulation has a major influence on photon efficiency. For the purposes of our design exploration we have chosen a novel burst pulse-position modulation (BPPM). Its significant disadvantage is an increase in peak transmit power<sup>10</sup>  $P_P^T$ . However, this is offset by some significant advantages:

- Optical dark counts originating as blackbody radiation in the optical path and in the optical detector are a major issue due to the potentially large number  $N^S$  of optical subsystems and optical detectors. The impact of dark counts in the receiver can be reduced to any degree desired (see §6.7).
- As the propagation distance  $D$  from the probe increases, the data rate  $\mathcal{R}$  has to decrease to accommodate the decreasing signal power reaching the receiver. Similarly probes with different masses or more advanced technology may have greater electrical power available, allowing for an increase in  $\mathcal{R}$ . With BPPM  $\mathcal{R}$  is adjusted very simply by matching the rate at which PPM frames are transmitted to available average transmit power  $P_A^T$ . This is a major theoretical and practical simplification of the design, because no adjustment in

<sup>9</sup> If as in (Parkin 2019) there were a single probe and pointing accuracy is not a consideration, the coverage could be as small as needed to achieve sufficient sensitivity.

<sup>10</sup> In the dark-count dominated regime BPPM doesn't actually increase  $P_P^T$ , because it increases PAR by reducing average power rather than increasing peak power (see Fig.19).

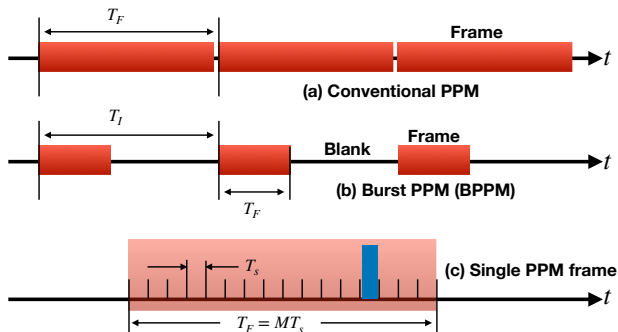


**Figure 4.** An illustration of two forms of pulse-position modulation (PPM). (a) In conventional PPM the time axis is filled with PPM frames and data rate  $\mathcal{R}$  is changed by changing the time duration  $T_F$  of those frames. (b) In burst-PPM (BPPM) the PPM frame duration  $T_F$  is decoupled from the inter-frame interval  $T_I$  allowing for blanking intervals between frames, and  $\mathcal{R}$  is changed by changing  $T_I$  while keeping  $T_F$  fixed. (c) The internal structure of each PPM frame consists of  $M$  time slots, each with duration equal to the slot time  $T_s$ . Both  $\{M, T_s\}$  are kept fixed with changes in  $\mathcal{R}$ .

optical bandwidth, ECC or other aspect of the design is required (see §6.3).

- It is difficult to achieve the desired selectivity in a receiver optical bandpass filter with current technology, and adjustment of bandwidth to a changing data rate is also a challenge. With BPPM the optical bandwidth can be increased to any degree desired, relaxing the selectivity requirement, and can be held fixed across time, distance, and probes with different masses. This accrues without penalty in background radiation (see §6.7).

The structure of the intensity-modulated signal is defined in Fig.4. The signal is divided into *PPM frames*, each with *frame duration*  $T_F$ . Frames are typically interspersed with *blank intervals*, during which no optical power is transmitted. The total time interval between the beginning of successive frames is the *frame interval time*  $T_I$ .

Within each frame, the signal is structured as exactly one pulse of light, which may occur in one of  $M$  short time intervals called *slots*, each with *slot duration*  $T_s$ , so that  $T_F = M T_s$ . This internal frame structure is called *pulse-position modulation* (PPM). PPM is commonly used in optical communications because it trades greater bandwidth (often an ample resource) for improved energy efficiency.

The receiver must synchronize its timing with frames and slots, a function called *timing recovery*.<sup>11</sup> With knowledge of the frame and slot timing, there are three possibilities for how many photons are detected:

- One or more photons are detected within the slot populated at the transmitter, but none in the other slots nor the blanking interval.
- No photons are detected within the entire frame, which is declared a *frame erasure*.
- One or more photons are detected within two or more slots, which is declared a *recognized frame error*.
- One or more photons are detected within exactly one slot not populated at the transmitter. This is an *unrecognized frame error*.

Erasures are a manifestation of signal shot noise and frame errors are attributable to background radiation.

Knowledge of erasures and recognized frame errors is preserved for subsequent processing. We find that to achieve high photon efficiency BPP the rate of erasures must be 80-90%, but the inclusion of substantial error-correction redundancy can overcome these erasures and yield acceptably low error rates in the recovery of the scientific data (see §10).

In the conventional PPM shown in Fig.4a the blank intervals are eliminated, but in the BPPM shown in Fig.4b blank intervals between frames are allowed (conventional PPM is a special case). In this case the *duty cycle*  $\delta = T_F/T_I$  is defined. We can think of BPPM as a higher-data-rate transmission scheme operating with a duty cycle  $\delta < 1$ .

### 3. PROBE MASS TRADEOFFS

A feature of a directed-energy launcher is that, for a fixed launcher infrastructure, a variety of probe versions with different masses can be launched.<sup>12</sup> The probe speed  $u_0$  and initial data rate  $\mathcal{R}_0$  in Tbl.2 are used in the numerical examples here. These are estimates for a lowest-mass “wafer scale” version. The question is, on what basis do we choose a probe mass?.

In terms of scientific outcomes the  $\mathcal{R}_0$  is of only indirect interest. In terms of the scientific mission the performance metrics of direct interest are:

- The total data volume  $\mathcal{V}$  returned.
- The data latency  $T_L$ , which is the time elapsed from probe launch to the return of data volume  $\mathcal{V}$  in its entirety.

<sup>11</sup> Timing recovery is a standard function of all digital communication systems, and will not be addressed further. This is one of the post-processing functions included in Fig.3.

<sup>12</sup> The many uses of a launcher, its deployment, as well as the benefits and issues of various mass missions are discussed in (Lubin et al. 2018a).

**Table 3.** Data latency/volume for planetary missions<sup>a</sup>

Target Mission	Neptune Voyager 2	Pluto New Horizons
Data rate $\mathcal{R}$	$\sim 1$ kbps	$\sim 1$ kbps
Data latency $T_L$	12 yr	10.5 yr
Data volume $\mathcal{V}$	18 Gb	50 Gb

<sup>a</sup> 9000 images were returned from Neptune (Smith et al. 1989) at 2 Mb per image (Ludwig & Taylor 2016). The data rate was programmable and variable. The Pluto scientific data return was 50 Gb (Fountain et al. 2009).

- The reliability with which the data is recovered (see §10).

We now show that there is an optimum mass  $m$  such that  $T_L$  is minimized for a given  $\mathcal{V}$ , or  $\mathcal{V}$  is maximized for a given  $T_L$ . Thus a principled way to choose the mass is to incorporate any constraints on  $T_L$  or  $\mathcal{V}$ . For comparison, estimates of these metrics for two outer-planetary missions are listed in Tbl.3.

### 3.1. Mass scaling approximations

The mass  $m$  strongly influences the probe speed  $u_0$  and the initial scientific data rate  $\mathcal{R}_0$ , which in turn determine  $T_L$  and  $\mathcal{V}$ . We define a set of scaling laws,

$$\begin{aligned} m(\zeta) &= \zeta \cdot m(1) \\ u_0(\zeta) &= \zeta^{-1/4} \cdot u_0(1), \quad \mathcal{R}_0(\zeta) = \zeta^2 \cdot \mathcal{R}_0(1). \end{aligned} \quad (4)$$

The mass ratio  $\zeta \geq 1$  is the factor by which mass is increased. Transmission starts at the target star distance  $D = D_0$  and ends at distance  $D_1 > D_0$ . The data rate starts at  $\mathcal{R}_0$  and decreases with  $D$  in accordance with (11). The scaling of  $\mathcal{R}_0$  in (4) assumes that  $\{P_A^T, P_P^T, A_e^T\} \propto \zeta$  (the detailed scaling depends on the specifics of the probe design). It is shown later (see (6) and (1)) that in this case  $\mathcal{R}_0$  follows (4), with one factor of  $\zeta$  due to increased  $P_A^T$  and another factor of  $\zeta$  due to increased  $A_e^T$ . The scaling ratio for  $u_0$  follows from the launch dynamics, assuming a fixed launch infrastructure (Lubin et al. 2018a).

### 3.2. Latency-volume tradeoff

The relationship between  $\mathcal{V}$  and  $T_L$  parameterized by  $\zeta$  is determined in §C and plotted in Fig.5 for five values of  $\zeta$ . The volume scales as  $\mathcal{V} \propto \mathcal{R}_0(1)$ , so a change in  $\mathcal{R}_0(1)$  would shift all curves horizontally. There are three components of  $T_L$ : transit time, transmission time, and propagation time. The minimum  $T_L$  increases with  $\zeta$  due to the greater transit time. Eventually  $T_L$  increases rapidly with  $\mathcal{V}$  due to the decreasing  $\mathcal{R}$  with  $D$ .

For each  $\mathcal{V}$  there is an optimum choice of  $\zeta$  that minimizes  $T_L$ . The resulting minimum  $T_L$  vs  $\mathcal{V}$  is plotted as the dashed curve in Fig.5 and is also plotted in Fig.6. The latter plot shows the decomposition of  $T_L$  into its three components. The latency-minimizing value of  $\zeta$ , the resulting transmission time, and the distance  $D_1$  at the end of transmission are plotted in Fig.7.

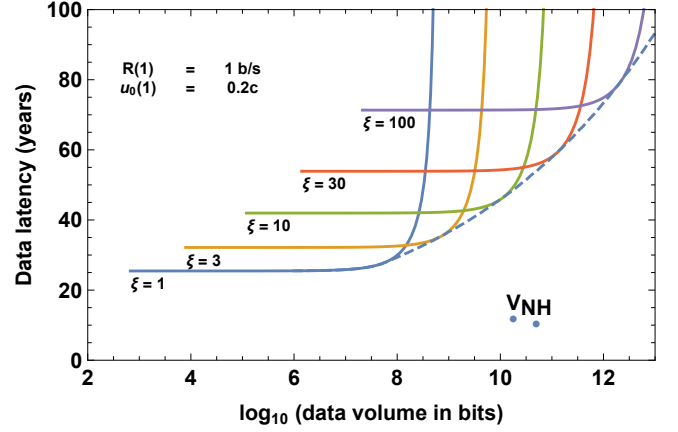


**Figure 5.** Plot of the data latency  $T_L$  in yr vs the logarithm of the total data volume  $\mathcal{V}$  in bits for different values of the mass ratio  $\zeta$  (the curves are labeled with  $\zeta$ ). For example  $\log_{10} \mathcal{V} = 9$  corresponds to  $10^9$  bits or 1 Gb. The dashed line is, for each value of  $\mathcal{V}$ , the minimum  $T_L$  achievable by the optimum choice of  $\zeta$ . It is assumed that for  $\zeta = 1$  (the lowest-mass probe), the speed is  $u_0(1) = 0.2c$ , and the initial transmit data rate is  $\mathcal{R}_0(1) = 1$  b/s. The Voyager (V) and New Horizons (NH) points are obtained from Tbl.3.

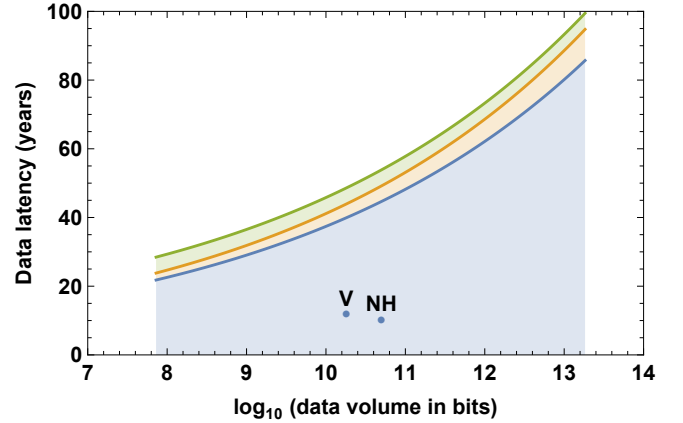


**Figure 6.** A plot of the data latency  $T_L$  vs data volume  $\mathcal{V}$ , where for each value of  $\mathcal{V}$  the latency-minimizing mass ratio  $\zeta$  is chosen. This ranges about 28 to 100 years, where larger  $\mathcal{V}$  is associated with a larger  $\zeta$  and a larger  $T_L$ .  $T_L$  is decomposed into its three components, from bottom to top: Transit time to the star, the transmission time, and the return signal propagation time, all measured by an earth clock. Latency is dominated by the transit time.

If  $\mathcal{V}$  is increased, both the optimum  $\zeta$  and  $T_L$  increase. For the optimum  $\zeta$  the transmission time is always much shorter than the transit time. Obtaining a larger  $\mathcal{V}$  requires increased transmission time, but the distance traveled during transmission remains relatively constant since the probe's speed is lower. For the range of parameters shown, the minimum  $T_L$  falls in the 30 to 80 year

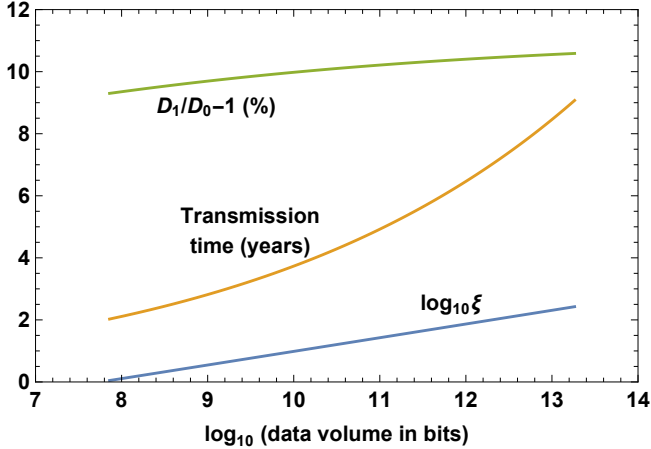


**Figure 7.** Three quantities of particular interest are plotted as a function of data volume  $\mathcal{V}$ . First is the log of the optimum mass ratio  $\zeta$  that minimizes the data latency  $T_L$ . A plot of  $T_L$  vs  $\mathcal{V}$  for this optimum  $\zeta$  is shown in Fig.6. Second is the transmission time component of  $T_L$ , which varies in the range of two to nine years. Third is the distance increase  $(D_1/D_0 - 1)$  expressed as a percentage. The space probe travels a fairly consistent 9% to 10% farther than the target star during downlink transmission.

range for a data volume in the 100 Mb to Tb range. Volumes  $\mathcal{V}$  comparable to the planetary missions are feasible with the assumed  $\mathcal{R}_0(1)$ , but only with  $\zeta \sim 20$  and  $T_L \sim 50$  yr. The  $\mathcal{V}$  and  $T_L$  parameters of Tbl.1 assume that downlink operation is 10% of the probe transit time.

#### 4. CHOICE OF WAVELENGTH

The two spectrum ranges offering atmospheric transparency for a terrestrial receiver are millimeter wave radio and visible optical. This choice affects nearly every aspect of the design. We study the optical case in this paper, but the radio possibility should also be considered.

##### 4.1. Propagation loss

As compared to the outer planets, the propagation losses from the nearest stars approach a factor of  $>10^8$ . This obstacle is overcome by an adjustment to other parameters in Tbl.2, including prominently wavelength, data rate, and receive aperture size.

The appropriate signal level at the receiver is measured differently at radio and optical wavelengths. For radio wavelengths it is the average power  $P_A^R = N^S P_A^S$ , while for optical (assuming direct detection) it is the average rate of detected photons  $\Lambda_A^R = N^S \Lambda_A^S$ . These metrics are affected by the propagation loss and atmospheric effects, with the latter more significant at optical wavelengths (see §7). Neglecting atmospheric absorption and turbulence, these metrics are determined by the average

**Table 4.** For equivalent SNR, scaling of the NH radio downlink to a low mass probe illustrating the impractically large receive aperture size that may be needed.

Parameter	NH	Low mass
Distance $D_0$	4.5 lh	4.24 ly
Wavelength $\lambda_0$	3.6 cm	10 mm
Transmit power $P_A^T$	24 W	0.1 W
Transmit aperture diameter $\sqrt{4A_e^T/\pi}$	2.1 m	10 cm
Receive aperture diameter $\sqrt{4A_e^R/\pi}$	70 m	1652 km
Data rate $\mathcal{R}$	1 kb/s	1 b/s

transmitted power  $P_A^T$  through a link budget,

$$P_A^S = \eta \cdot \frac{A_e^T A_e^S}{\lambda_0^2 D_0^2} \cdot P_A^T \quad (5)$$

$$\Lambda_A^S = \frac{\lambda_0}{hc} \cdot P_A^S = \eta \cdot \frac{A_e^T A_e^S}{hc \lambda_0 D_0^2} \cdot P_A^T \quad (6)$$

(see §B.4.2 and (B8)). The factor  $\lambda_0/hc$  in (6) converts from power to photons per second.

The *efficiency factor*  $0 < \eta \leq 1$  in (6) accounts for non-propagation losses, such as aperture pointing error (see §8.5), as well as attenuation and the quantum efficiency in the receiver. A Doppler red shift in wavelength from transmitter to receiver has also been neglected in (6) by setting  $\lambda_0^R = \lambda_0^S = \lambda_0$  (for  $u_0 = 0.2c$  this shift is about 20%). Relativistic aberration has also been neglected.

##### 4.2. Radio

Although radio is used for deep space missions today, the primary objection to radio at interstellar distances is the large aperture sizes (or alternatively large transmit power). As an order-of-magnitude estimate, factors affecting the link budget for the New Horizons (NH) mission are scaled to accommodate interstellar distances in Tbl.4. Although it would be desirable if transmit power and aperture size could be increased to compensate for the greater distance, they will likely be substantially *decreased* for low-mass probes. In principle these adverse elements can be compensated by a lower data rate, a substantially larger receive aperture area, and/or shorter wavelength. The shortest radio wavelength that consistently penetrates the atmosphere is chosen.

An appropriate link budget for radio is (5). Assuming that there is one single-mode diffraction-limited sub-array which receives signal power  $P_A^S$ , the parameters contributing to this received power  $P_A^S$  are listed in Tbl.4, with reasonable assumptions for the transmit power and aperture size. When substituted into (5) the received power is found to be a factor of  $10^3$  smaller for the low-mass probe. This results in an equivalent signal-to-noise ratio SNR at the receiver for two reasons. First the major noise impairments are isotropic cosmic background radiation and receiver thermal noise, which have the same white power spectral density independent of receive aperture area (see §B.4.3) and assuming equivalent

receiver noise factor. Second for an equivalent modulation and coding scheme the receiver bandwidth can be reduced by a factor of  $10^3$  in the low-mass case due to the lower data rate, thereby reducing the noise component of SNR by the same factor.

The receive aperture is impractically large, especially considering that it is assumed to be diffraction limited. Such an aperture would also require an impractical pointing accuracy, although this requirement could in principle be relaxed by implementing a phased array with equivalent total collection area.<sup>13</sup> A larger transmit aperture, higher transmit power, or lower data rate would reduce the receive aperture area.

### 4.3. Optical

Relative to radio, choosing an optical wavelength yields a factor of  $10^4$  to  $10^5$  in the link budget of (6) (depending on the two wavelengths being compared). This is a considerable advantage, but optical wavelengths also pose substantial challenges. One is atmospheric effects (see §7), with the resulting scintillation (fading in communication terms) and weather-based outages.

One challenge in optical communication with direct detection (see §2.5.4) is a ‘mode shift’ in photon efficiency BPP vs SBR at low values of SBR. This is observed in the theoretical limit on feasible photon efficiency BPP, which is essentially independent of SBR (for fixed peak-to-average ratio PAR) for large values of SBR, but deteriorates rapidly for small SBR (see Fig.29). Intuitively this is due to the effect of modulation and detection based on signal power (photon count), and the effects of square-law detection on background radiation. The case is made in (Toyoshima et al. 2007; Moision & Farr 2014) that a probe receding in distance from earth will suffer a deterioration in SBR due in part to a reduction in data rate and signal power in the face of a fixed (or even growing) background radiation, and as a result the link budget switches dependency from  $D^2$  to  $D^4$ . However, these papers make specific technological assumptions as to modulation and parameter scaling relations with  $D$  (such as holding optical bandwidth fixed even as the signal bandwidth decreases).<sup>14</sup>

A desirable  $D^{-2}$  behavior can be achieved at deteriorating SBR by replacing PPM by a more nuanced modulation and coding (Zwoliski et al. 2018), although this is unproven in practice. Here we use a simpler approach of simply constraining SBR to be relatively large.

<sup>13</sup> The incoherent accumulation of power as in Fig.3 is not acceptable since the NH modulation and coding scheme strongly exploits both signal amplitude and phase. Accurate phasing across constituent apertures is necessary.

<sup>14</sup> There is also one error in (Moision & Farr 2014), with the assumption that isotropic sources of noise increase as the effective area and directivity of the receive aperture is increased to compensate for greater distances. Actually noise due to unresolved sources is independent of directivity because the greater gain of a larger aperture is exactly offset by its smaller coverage (see §B.4.3).

Fortunately for a space mission and its presumed maximum propagation distance  $D = D_1$  this challenge is circumvented by ensuring that SBR is relatively large at distance  $D_1$ . We constrain SBR to a relatively large value at this distance (in our case SBR=4), with a correspondingly large average transmit power  $P_A^T$ . This is assisted by BPPM (see §2.12), which allows us to hold optical bandwidth  $W_e$  fixed (subject to any technological limitations on bandpass filtering) without penalty in SBR as  $D$  increases, although a price is paid in a correspondingly growing peak transmit power  $P_P^T$ .

Our numerical results in §6.8 subject to these assumptions do strongly suggest that communication with low-mass probes at optical wavelengths is not feasible given the current state of technology. We identify here four key technologies that must advance to empower optical communication in this application. These are: achieving relatively high peak powers at the optical detector through pulse compression or other means (see §9.1); more selective optical bandpass filtering (see §9.2); attenuation of interference by a coronagraph function (see §8.6); and receiver optics (including superconducting optical detectors) with very low dark counts (see §9.3).

Since the relative advances in these technologies cannot be anticipated with any degree of certainty, BPPM is chosen as a modulation technique with greater freedom in trading off advances in these four technologies (see §2.12) as one specific goal. Achieving a relatively large and constrained SBR at the greatest distance  $D_1$  is aided by the minimal increase in distance (about 10%) during transmission (see Fig.7). The requirements for these four technologies and related tradeoffs are studied by numerical modeling in §6.8.

### 4.4. Space-based receiver

Although not considered further here, a space-based receiver would be advantageous for the elimination of atmospheric effects and also the possibility of going to ultraviolet (UV) wavelengths (10 to 400 nm). UV would further moderate aperture sizes and substantially reduce the star interference (see §6.8 and (Lubin et al. 2018a)). While UV laser communications is not currently technologically advanced (due primarily to its inability to penetrate the atmosphere) it is an option to consider for the future.

## 5. TRAJECTORIES AND COVERAGE

The coverage  $\Omega_A$  of each sub-array determines the effective area  $A_e^S$ , which in turn influences the transmit power-area product  $P_A^T A_e^T$  necessary to achieve the desired SBR at the receiver. The parameters affecting coverage are (beyond our control) parallax and the star’s proper motion and (under our control) the swarm launch schedule and sophistication of the sub-array beamforming.

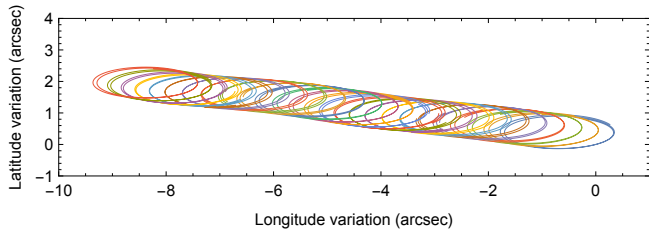


**Figure 8.** The variation in probe coordinates as viewed by a common terrestrial receive aperture. The variation in the longitude and latitude (in arcsec in an ecliptic coordinate system) for 26 probes launched at 30-day intervals is shown. The origin corresponds to the angle of Proxima Centauri when viewed from the initial launch site. Each elliptical trajectory is due to the parallax effect of the receiver orbit about the sun over a period of 2.21 yr, which corresponds to a probe’s travel 10% farther than the star. The general drift of the probe positions is due to the star’s proper motion, presenting a moving target for the various probes.

### 5.1. Concurrent swarm probe communication

The probe trajectories as viewed from Earth are shown in Fig.8 for a specific launch schedule.<sup>15</sup> The chosen parameters, including duration of transmission and interval between launches, result in 26 probes transmitting concurrently, each one operating a downlink for 2.21 yr (see §3.2). For the position of Proxima Centauri relative to the earth’s orbit, the overall longitudinal parallax angular variation ( $\sim 2$  as) is about twice as great as the latitudinal ( $\sim 1$  as).

The star’s proper motion determines the relative position of probes launched at different times. For Proxima Centauri this motion is 368 mas/yr and  $-3775$  mas/yr in declination and right ascension respectively.<sup>16</sup> Fortunately, the largest component of proper motion is aligned with the largest overall parallax (longitude and right ascension). The trajectories of consecutively launched probes will sometimes coincide (unless the inter-launch interval is greater than about eight months) and thus their signals could not be consistently separated spatially.

The coverage implications depend on the refinement in beamforming in each sub-array. Minimizing coverage (maximizing sensitivity) requires beamforming the precise location of each probe, while the simplest beamforming simply captures the full variation in parallax shown in Fig.8 for each probe and also across the rel-

<sup>15</sup> The variation in angle due to parallax does not depend on the chosen coordinate system. To readily capture the earth’s orbit, a heliocentric ecliptic XYZ coordinate system is used. The earth orbit and a fixed star position were obtained from Mathematica<sup>®</sup> `StarData["Heliocoordinates"]` and `PlanetData["Heliocoordinates"]` followed by transformation to spherical coordinates.

<sup>16</sup> Obtained from Mathematica<sup>®</sup> `StarData["ProperMotion"]`.

ative positions of successive probe launches. The numerical results in §6.8 address these disparate cases by considering a range of  $\Omega_A$  values.

At longitude  $l$  and latitude  $b$  the solid angle of coverage is, for small  $\Delta l$  and  $\Delta b$ ,

$$\Omega_A \sim \cos(b) \cdot \Delta b \Delta l \quad (7)$$

Based on Fig.8 for the simplest beamforming we have  $\Delta b \approx 1$  as, and for Proxima Centauri  $\cos(b) = 0.71$ .  $\Delta l$  is dominated by proper motion and is  $\Delta l \sim 10$  as for the assumptions in Fig.8, and thus  $\Omega_A \approx 7.1$  as<sup>2</sup>. To account for the practicalities of sidelobes we assume that  $\Omega_A = 10$  as<sup>2</sup> in Tbl.2.

The coverage can be manipulated by the launch schedule. For example  $\Omega_A$  could be reduced by moving toward a *burst-mode launch schedule*, in which a sub-swarm of probes are launched at closely spaced times interspersed with launch-inactive time periods greater than the individual-downlink operation time (on the order of two years for the parameters of Tbl.2 and Fig.7).

### 5.2. Single-probe communication

At the other extreme, if a receive aperture is dedicated to a single probe and can dynamically compensate for parallax and atmospheric refraction of the signal path, the smallest coverage solid angle  $\Omega_A$  will be determined by the sub-array pointing accuracy. If we assume that with adaptive optics the pointing accuracy of the sub-arrays is  $\approx 0.1$  as, then the coverage can be no smaller than  $\Omega_A \approx 0.01$  as<sup>2</sup> (this the value assumed in Tbl.2).<sup>17</sup> Our goal in the numerical results is to consider this entire range of possibilities.

## 6. TECHNOLOGY TRADEOFFS THROUGH BPPM

Before discussing the key enabling technologies, it is helpful to appreciate the trade-offs available through the choice of parameters of BPPM. BPPM is specifically designed to permit a greater advancement of one technology to offset a lesser advancement of another. This is reflected in the modeling equations for BPPM in Tbl.5, which are now described and then used in an extended numerical example.

### 6.1. Metrics and methodology

Achieving a gram-scale probe mass limit is challenging. For this purpose a useful metric for a design is the product of the transmit {average,peak} power and aperture effective area  $\xi_{\{A,P\}}^T = P_{\{A,P\}}^T A_e^T$ , which should be monotonically related to probe mass due to their impacts on electrical power generation and the transmit

<sup>17</sup> The  $A_e^S = 707$  m<sup>2</sup> assumption in (Parkin 2019) implies  $\Omega_A = 9.4 \cdot 10^{-5}$  and hence a sub-array pointing accuracy on the order of 0.01 arcsec or better. The sub-array sensitivity and the target star interference calculations are strongly dependent on this assumption.

**Table 5.** Receive aperture design equations with BPPM

<b>Parameters:</b>	
<b>Data reliability:</b>	SBR, BPP, $\mathcal{R}_0, W_e, K_s^R, m$
<b>Geometric:</b>	$b, \Delta b, \Delta l, \Omega_A, \lambda^R, D_0$
<b>Physical:</b>	$\eta, F_c, F_x, T_s, \Lambda_{N,I,D}^S$
<b>Transmitter:</b>	
$T_F = MT_s$	$W_e T_s > 1$
$P_P^T T_s = P_A^T T_I$	$T_I \mathcal{R}_0 = K_s^R \cdot \text{BPP}$
$\text{BPP} = \frac{1 - e^{-K_s^R}}{K_s^R} \cdot m$	$M = 2^m$
<b>Sub-array:</b>	
	$\Lambda_P^S = \frac{P_P^T A_e^T A_e^S}{hc \lambda^R D_0^2}$
$K_s^S = \eta \Lambda_P^S T_s$	$K_X^S = \eta F_x \Lambda_P^S T_F$
$K_N^S = \eta \Lambda_N^S W_e T_F$	$K_I^S = \eta F_c \Lambda_I^S W_e A_e^S T_F$
$K_D^S = \Lambda_D^S T_F$	$\text{SBR} = \frac{K_s^S}{K_X^S + K_N^S + K_I^S + K_D^S}$
$A_e^S \cdot \Omega_A = (\lambda^R)^2$	$\Omega_A = \cos(b) \cdot \Delta b \Delta l$
<b>Receive aperture:</b>	$N^S = K_s^R / K_s^S$
<b>Metrics:</b>	$A_e^S, P_A^T, P_P^T, N^S$

aperture size (see §3.1). Fixing a value for  $\xi_{A,P}^T$  admits a tradeoff between transmit power and aperture area without affecting the signal level as seen by the receiver.

Our design methodology is to minimize the average-power-area metric  $\xi_A^T$  subject to reliable recovery of scientific data, constraints on receiver coverage accommodating probe-swarm trajectories, and the physical limitations imposed by background radiation and self-noise in the receiver. This minimization is achieved by operating at the lowest SBR consistent with reliable data recovery, operating near the theoretical limits of photon efficiency, and subject to the fundamental physical constraints on a receive aperture imposed by the desired coverage. A major component of receiver cost is the receive aperture. A metric relating to that cost is the receive aperture total effective area  $A_e^S N^S$ . We do not choose or constrain  $N^S$ , but rather ascertain the value required to achieve reliable data recovery subject to that minimum  $\xi_A^T$ . Subsequently we consider the implications of varying  $N^S$  about this unconstrained choice.

Recognizing a tradeoff between  $\xi_{\{A,P\}}^T$  and receive aperture area, another useful metric for a design is the *end-to-end* power-area-area metric

$$\xi_{\{A,P\}}^{TR} = P_{\{A,P\}}^T A_e^T \cdot A_e^S N^S = \xi_{\{A,P\}}^T \cdot A_e^S N^S.$$

Ascertaining the dependence of  $\xi_{\{A,P\}}^{TR}$  on other parameters quantifies the tradeoff between  $\xi_{\{A,P\}}^T$  and receive aperture total area  $N^S A_e^S$ .

## 6.2. Reliability in scientific data recovery

The design equations of Tbl.5 constrain  $K_s^S$ , the signal photons per slot (which also equals the signal photons per frame) that are detected on average by each sub-array, to achieve the design objective for SBR. Thus the

solution to these design equations yields the minimum  $K_s^S$  (and hence probe metric  $\xi^T$ ) consistent with achieving the target SBR.

The input data reliability parameters in Tbl.5 must be chosen so that the assumed BPP is consistent with the theoretical limits displayed in §E and §F. SBR is the ratio of  $K_s^S$  average received signal photons per PPM frame (and hence one slot) to average background photons during frame duration  $T_F$ , both instrumented at each sub-array. Background photons during BPPM blank intervals are thus ignored. The factor  $A_e^S$  cannot be chosen independently, but rather is determined by coverage solid angle  $\Omega_A$ .

Based on Tbl.5, the end-to-end metrics  $\xi_{\{A,P\}}^{TR}$  defined in §6.1 are

$$\xi_A^{TR} = \xi_A^T \cdot A_e^S N^S = \frac{hc \lambda_0^R D^2}{\eta} \cdot \frac{\mathcal{R}}{\text{BPP}} \quad (8)$$

$$\xi_P^{TR} = \xi_P^T \cdot A_e^S N^S = \frac{hc \lambda_0^R D^2}{\eta} \cdot \frac{K_s^R}{T_s}. \quad (9)$$

$\xi_A^{TR}$  in (8) is a reformulation of the single-sub-array link budget (6) for the architecture of Fig.3. Expressed in terms of  $\Omega_A$ , (8) becomes

$$\xi_A^T = \frac{hc D^2}{\lambda_0^R \eta} \cdot \frac{\mathcal{R}}{\text{BPP}} \cdot \frac{\Omega_A}{N^S}, \quad (10)$$

and a similar relation applies to  $\xi_P^T$ . For fixed coverage there is an expected inverse tradeoff between  $\xi_A^T$  and  $N^S$  governed by the hidden parameter SBR. Increasing SBR requires a larger  $\xi_A^T$  to achieve the higher signal level at the sub-array, and reduces  $N^S$  accordingly (see §6.9.1).

$\xi_A^{TR}$  in (8) and  $\xi_A^T$  in (10) quantifies the adverse effect of achieving a smaller BPP and/or smaller quantum efficiency  $\eta$ , and establishes a linear dependence on scientific data rate  $\mathcal{R}$ . For fixed coverage  $\Omega_A$ , a longer wavelength is advantageous in terms of  $\xi_A^T$  in (10), although this fails to account for the effect of wavelength on background radiation and hence  $N^S$ . Because it is blind to SBR, (10) also fails to capture a reduction in background radiation that follows from reducing BPP (see §6.9.2).

While (8) applies to average transmit power  $P_A^T$ , (9) applies to peak transmit power  $P_P^T$ . It demonstrates the invariance of  $\xi_P^{TR}$  to  $\mathcal{R}$  and BPP, but rather substitutes the parameters  $T_s$  and  $K_s^R$ . Parameter  $K_s^R$  has a major influence on data reliability, since it determines the shot-noise induced rate of PPM frame erasures. To achieve a large BPP, which beneficially reduces  $\xi_A^{TR}$ , it is perhaps surprising that  $K_s^R$  must be very small, resulting in a high probability of frame erasure (see §10.3). A nearly optimum choice across a range of conditions is  $K_s^R \approx 0.2$  (see §10.3.2). This is termed *photon starvation* of the PPM frames, and small  $K_s^R$  beneficially reduces  $\xi_P^{TR}$  as well. On the other hand, the equivalent parameter  $K_s^S$  at a sub-array output is determined by

SBR, and is not directly related to BPP or data reliability. The purpose of the scale-out of sub-arrays by the factor  $N^S = K_s^R/K_s^S$  is to multiply the value of  $K_s$  by incoherently accumulating received photons.

All the parameters and metrics in Tbl.5 neglect the effect of outages (caused by sunlight, weather, receive array maintenance, etc). With outages, the data rate can be reduced to  $\mathcal{R}_a < \mathcal{R}_0$  without compromising data reliability by increasing the redundancy in the ECC, with no other implications to the design (see §10.4).

6.3. *Changes with increasing propagation distance*

The downlink propagation distance  $D$  ranges over  $D_0 < D < D_1$ , where  $D_0$  is the distance to the target star (corresponding to scientific data acquisition) and  $D_1$  is the distance at which transmission is completed. As  $D$  increases in this range, a goal is to hold constant both the average transmit power (which is determined by the electrical generation capacity) and the reliability of scientific data recovery. It follows that the only parameters in the end-to-end metrics that can change are data rate  $\mathcal{R}$  and peak transmit power  $P_P^T$ . Assuming (8) remains fixed, we must have  $\mathcal{R} \propto D^{-2}$ . If the initial data rate at  $D = D_0$  is  $\mathcal{R}_0$  then

$$\mathcal{R}(D) = \mathcal{R}_0 \cdot \left(\frac{D_0}{D}\right)^2. \tag{11}$$

For fixed data reliability we choose to keep  $\{M, T_s, T_F, K_s\}$  fixed with  $D$ . Based on Tbl.5,  $\mathcal{R}$  can be changed simply by adjusting the frame interval  $T_I \propto \mathcal{R}^{-1}$ . In addition, based on (9) the peak transmit power has to be increased as  $P_P^T \propto D^2$ .

In summary, as  $D$  increases  $\mathcal{R}$  is adjusted downward by increasing  $T_I$ , and  $P_P^T$  is increased to maintain a fixed reliability and also a fixed  $P_A^T$ . All ECC parameters and algorithms remain fixed.

6.4. *Coverage*

The sensitivity of the sub-array is determined by  $A_e^S$ , as seen in the relation for  $\Lambda_P^S$ , and thus coverage and sensitivity are inversely related. That is, a swarm of probes received concurrently by a single receive aperture, to the extent that this necessitates a larger  $\Omega_A$ , increases the required  $P_{\{A,P\}}^T$  for each probe (see Tbl.2).

6.5. *Background radiation*

The relevant average detected photon rates at each sub-array are listed in Tbl.6 for each of the four sources of background. These are related to the detected peak photon rate  $\Lambda_P^S$  and the three physical parameters  $\Lambda_{N,I,D}$ , the appropriate units for which are listed in the third column. Like the probe signal, the three incident sources of radiation are affected by detection efficiency  $\eta$ , whereas the dark count rate is intrinsic to the detector and thus is not affected by  $\eta$ . Thus dark

**Table 6.** Constituents of background radiation

Source	Avg. ph/s	$\Lambda_{P,N,I,D}$ units
Source extinction	$\eta F_x \Lambda_P^S$	ph/s
Unresolved noise	$\eta \Lambda_N W_e$	ph/s-Hz
Host star interference	$\eta F_c \Lambda_I A_e^S W_e$	ph/s-Hz-m <sup>2</sup>
Detector dark counts	$\Lambda_D^S$	ph/s

counts become a more significant contributor to SBR as  $\eta$  decreases.

Noise and interference are broadband sources of radiation, and thus as they reach the optical detector are proportional to  $W_e$ , the bandwidth of the receive optical bandpass filter which precedes that detector. The extinction ratio  $F_x < 1$  determines the background following the optical bandpass filter that is related to incomplete extinction of the source.

Noise (due to unresolved sources of radiation) is considered to be isotropic over the coverage solid angle  $\Omega_A$ , and thus the captured photon rate is independent of  $A_e^S$  for a single-mode diffraction limited sub-array. This is because any changes to collection area are offset by the resulting change in coverage solid angle (see §B.4.3).

Interference (originating with the target star) is essentially a point source like the probe transmitter. It can be approximated as a plane wave when it reaches the sub-array, and the captured photon rate is thus proportional to the sub-array effective area  $A_e^S$ . Any rejection of this interference due to it falling outside the coverage angle or other coronagraph functionality is modeled by the coronagraph rejection ratio  $F_c \leq 1$ .

Dark counts are distinctive in being unaffected by either  $W_e$  or  $A_e^S$ .<sup>18</sup> This presents a unique challenge because we cannot limit dark counts originating in the detector (as opposed to receive optics) by optical bandpass filtering.

6.6. *Conditions on extinction ratio*

Returning to Tbl.5, the average photon counts per frame for signal ( $K_s^S$ ) and for incomplete extinction ( $K_X^S$ ) are related to the peak signal power  $\Lambda_P^S$ . This implies an upper limit on the permissible extinction ratio  $F_x$  that is related to the desired SBR. Eliminating  $\Lambda_X^S$  from the equations,

$$K_s^S = \frac{\text{SBR}(K_N^S + K_I^S + K_D^S)}{1 - MF_x \cdot \text{SBR}}. \tag{12}$$

Thus incomplete extinction ( $F_x > 0$ ) results in a compensating increase in the required  $K_s^S$ , which in turn requires an increase in  $P_P^T$ . This increase is unrelated to other sources of background, and since it is not a function of  $T_I$  is also unrelated to the benefits of BPPM (see

<sup>18</sup> This may not be true of dark counts originating as blackbody radiation from the optics preceding the optical bandpass filtering (see §9.3).

§6.7). Based on (12), a feasible design requires

$$F_x < (M \cdot \text{SBR})^{-1}. \quad (13)$$

This conclusion also follows directly from  $\text{SBR} < \text{SXR}$  (since incomplete extinction is one component of SBR) and  $\text{SXR} = 1/MF_x$ .

### 6.7. Opportunities afforded by BPPM

The slot time  $T_s$  plays a central role in Tbl.5. First, choosing a smaller  $T_s$  assists in achieving the targeted SBR by reducing all three of  $K_{\{N,I,D\}}^S$ . This boost in SBR results from ignoring all photon detection events that occur during the blank intervals in Fig.4. The price paid for smaller  $T_s$  is an increase in peak transmitted power  $P_P^T$ .

The reduction in dark counts arising from smaller  $T_s$  is especially advantageous, since dark counts are unabated by bandlimiting. This is significant because the numerical results in §6.8 suggest that dark counts are typically a very significant contributor to overall background radiation for larger coverages  $\Omega_A$ . This parallels radio telescopes, where thermal noise introduced in the receiver electronics typically dominates cosmic sources of noise.

Another important parameter in Tbl.5 that relates to technology issues is the optical bandwidth  $W_e$  imposed at the receiver, since this determines the level of noise and interference reaching the optical detector. The minimum bandwidth is determined by  $W_e T_s \sim 1$ , and it is natural to keep  $T_s$  fixed as distance  $D$  increases as well as across different probes (even if they have differing masses and data rates). As a result, the optical bandpass filter does not require agility or configurability.

The total noise and interference is always proportional to  $W_e T_s$ , and thus remains fixed if  $W_e$  is coordinated with  $T_s$ . Thus BPPM does not help (or hurt) with respect to total noise and interference at the optical detector. A reduction in  $T_s$  to minimize dark counts also increases the optical bandwidth  $W_e$  without increasing background radiation. In terms of optical bandpass filter technology this is desirable since it relaxes the required selectivity. In effect BPPM trades off background suppression (except for dark counts) between the frequency and time domains. Time-domain suppression is technologically preferable because it is simpler to implement and more precise. Thus all considerations (other than peak power) argue in favor of making  $T_s$  smaller.

### 6.8. Numerical results

We now justify the choice of parameters in Tbl.1 and Tbl.2, followed by a study of the sensitivity of these parameters to changing assumptions.

#### 6.8.1. Choice of nominal parameters

The choice of  $\mathcal{R}_0 = 1$  b/s is a convenient (but rather arbitrary) choice affecting average power  $P_A^T$ . This is the

scientific data rate during periods of non-outage, but for the chosen daylight and weather outage probabilities the net data rate is  $\mathcal{R}_a = 0.432$  b/s (see §10.4).

The reliability parameters in Tbl.1 must be self-consistent based on available theoretical bounds on the achievable BPP consistent with reliable recovery of scientific data. First, neglecting background radiation (that is  $\text{SBR}=\infty$ ), the choice  $m=12$  places an upper bound  $\text{BPP}<12$  b/ph based on (3). This is true of any possible modulation coding scheme. For the specific case of PPM, the theoretical upper bound is  $\text{BPP}<10.9$  b/ph for the chosen  $m$  and  $K_s$  based on (18). Second, taking into account background radiation, for this value of  $\text{PAR} = M$ , the choice  $\text{SBR}=4$  results in the theoretical bound  $\text{BPP}\leq 11.1$  b/ph for any photon-counting detector (see §E). Thus all available theoretical bounds are consistent with the assumption  $\text{BPP}=10.9$  in Tbl.2. Concrete ECC methods are not expected to quite achieve these theoretical bounds, so this BPP can be considered mildly optimistic.

A rather arbitrary choice is the dark count rate  $\Lambda_D^S=32$  yr<sup>-1</sup>, because we don't know what value may be feasible in the future. Assuming nighttime-only operation of the downlink (see §6.8.4), the two most significant sources of background (for the shorter wavelength) are moonlight and dark counts. The value  $\Lambda_D^S$  is chosen so that these two sources are about equal ( $\text{SNR} \approx \text{SDR}$ ) at the largest coverage ( $\Omega_A=10$  as<sup>2</sup>). Thus, a larger (or smaller)  $\Lambda_D^S$  will render dark counts (or moonlight) the dominant source of background radiation under these specific conditions.

The choice of transmit aperture effective area  $A_e^T$  is also rather arbitrary, choosing an area that seems consistent with a low-mass probe. Both the transmit powers  $P_{\{A,P\}}^T$  are inversely proportional to  $A_e^T$ , so measures to increase this area are directly beneficial in terms of power.

From (13)  $F_x < 6 \times 10^{-5}$  for the parameters in Tbl.2. A 77 dB extinction ratio ( $F_x=2 \times 10^{-8}$ ) has been achieved in bench testing (Farr et al. 2013). The  $F_x=10^{-7}$  value in Tbl.2 thus appears feasible today, and renders incomplete extinction a relatively minor contributor to the background.

The effect of changes to wavelength  $\lambda_0^R$  are multifaceted. If the coverage  $\Omega_A$  is held fixed, effective area  $A_e^S$  is proportional to  $(\lambda_0^R)^2$  and thus the signal power increases in proportion to  $\lambda_0^R$  in (6), the interference increases in proportion to  $(\lambda_0^R)^2$  from Tbl.6, and hence overall there is increased interference. For a red-dwarf star such as Proxima Centauri the interference is magnified further because of the wavelength-dependence of the star black body radiation (see Tbl.7). Increasing the wavelength to  $\lambda^R=1$   $\mu\text{m}$  in Tbl.1 causes interference to replace moonlight and dark counts as the dominant component of background radiation, and results in a substantial increase in transmit power (to  $P_A^T=562$  mW and

$P_P^T=12.2$  MW) for the swarm case in Tbl.2. This larger interference could be mitigated by a larger coronagraph rejection (smaller  $F_c$ ).

Reduction in  $\Omega_A$  from the swarm to single-probe case in Tbl.2 beneficially reduces the transmit powers due to the larger effective area  $A_e^S$  of the sub-array, but increases the total receive aperture area  $A_e^S N_S$ . Thus, reducing  $\Omega_A$  yields the expected tradeoff between a larger receive aperture and reduced transmit powers. Similarly a larger transmit aperture effective area  $A_e^T$  can be directly traded for smaller transmit powers.

We will find that generally the required  $P_P^T$  cannot be achieved by available semiconductor lasers. Some ideas for potentially circumventing this issue, none of them currently qualified, are discussed §9.1.

Each PPM frame in BPPM represents  $K_s^R \cdot$  BPP bits of scientific data on average, and since this equals the number of scientific data bits  $T_I \mathcal{R}_0$  in each frame, it follows that  $T_I \propto K_s^R$ . This implies that in the photon starvation regime where  $K_s \ll 1$  the rate at which frames are transmitted  $T_I^{-1}$  is relatively large. For example, for the parameters in Tbl.1 we have  $T_I = 2.2$  s/frame, and only 2.2 scientific data bits are represented by each frame on average. When  $m=12$  each PPM frame actually represents 12 bits, which we infer represents 2.2 scientific data bits and 9.8 bits of redundancy. This redundancy is exploited by ECC to achieve reliability in the face of a high rate of frame erasures (see §10.3). ECC achieves reliable data recovery by simultaneously mapping a large number of scientific data bits into a large number of PPM frames, thereby statistically averaging over the random frame erasures (see §10.3).

We now give an extended numerical example based on the design relations in Tbl.5 with the goal of more fully appreciating the tradeoffs inherent in a BPPM design.<sup>19</sup> This numerical tradeoff is idealized, neglecting some material degradations in performance from other factors such as sub-array pointing inaccuracy and atmospheric effects (refraction and turbulence).

6.8.2. Sub-array effective area

The area  $\log_{10} A_e^S$  is plotted in Fig.9 for two wavelengths of interest as a function of the coverage solid angle  $\Omega_A$  over the range bracketed by the swarm and single-probe cases in Tbl.2. This tradeoff is straightforward as it does not involve other factors such as background radiation. Choosing a shorter wavelength reduces  $A_e^S$  (and therefore sub-array sensitivity) for fixed coverage. Increased coverage also reduces sub-array sensitivity at a fixed wavelength.

6.8.3. Background radiation

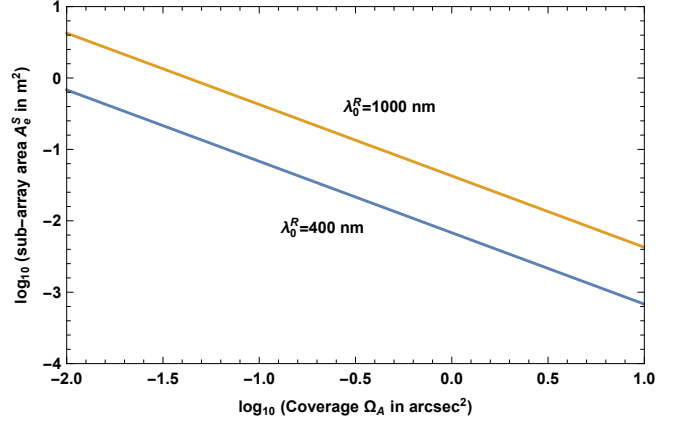


Figure 9. A log plot of the effective area  $A_e^S$  of a sub-array vs coverage solid angle  $\Omega_A$ . This assumes an idealized sub-array that achieves a uniform sensitivity over  $\Omega_A$ .

Table 7. Assumed numerical values for background photon rates following a single-mode diffraction-limited sub-array.

Radiation source	Units	400 nm	1.0 $\mu\text{m}$
<b>Point-source interference</b>			
Proxima Centauri $\Lambda_I$	ph/s-m <sup>2</sup> -Hz	$8.0 \cdot 10^{-10}$	$2.0 \cdot 10^{-7}$
<b>Unresolved sky noise</b>			
Zodiacal light $\Lambda_{N,zodi}$	ph/s-Hz		
90 degrees to ecliptic		$2.0 \cdot 10^{-16}$	$1.0 \cdot 10^{-14}$
Faint-star light $\Lambda_{N,star}$	ph/s-Hz	$2.0 \cdot 10^{-16}$	$1.0 \cdot 10^{-14}$
<b>Atmospheric scattering</b>			
Daylight $\Lambda_{N,sun}$	ph/s-Hz	$4.1 \cdot 10^{-8}$	$5.0 \cdot 10^{-7}$
Fullmoon $\Lambda_{N,moon}$	ph/s-Hz	$1.0 \cdot 10^{-13}$	$1.3 \cdot 10^{-12}$

The physical parameters characterizing the noise and interference used in the following numerical calculations are listed in Tbl.7.<sup>20</sup> The values given apply to a *single* sub-array in the architecture of Fig.3, since each sub-array has a single optical detector and thus qualifies as a single-mode ‘antenna’ in the sense of §B.<sup>21</sup> The units in Tbl.7 are consistent with Tbl.6.

Two wavelengths are compared in Tbl.2, 1  $\mu\text{m}$  (near infrared) and 400 nm (blue visible). The latter is of interest because of the substantially smaller interference from Proxima Centauri, which as a red dwarf star with a power spectrum weighted toward the red. The total noise contribution to background radiation during nighttime operation is

$$\Lambda_N = \Lambda_{N,zodi} + \Lambda_{N,stars} + \rho_{moon} \cdot \Lambda_{N,moon} .$$

While  $\Lambda_{N,moon}$  assumes a full moon, the factor  $0 \leq \rho_{moon} \leq 1$  can adjust for the lower radiance dur-

<sup>20</sup> Zodiacal noise is adopted from (Hauser et al. 1998) and the sky noise and star interference are adopted from (Lubin et al. 2018a; Lubin 2020). The atmospheric scattering values are justified in §7.1.

<sup>21</sup> This applies even if an optical detector is shared among multiple sub-arrays as described in §2.10.4 as long as optical interference among sub-arrays is avoided.

<sup>19</sup> An online spreadsheet is available at [tiny.cc/BPPMmodel](http://tiny.cc/BPPMmodel) for design exploration based on the model of Tbl.5.

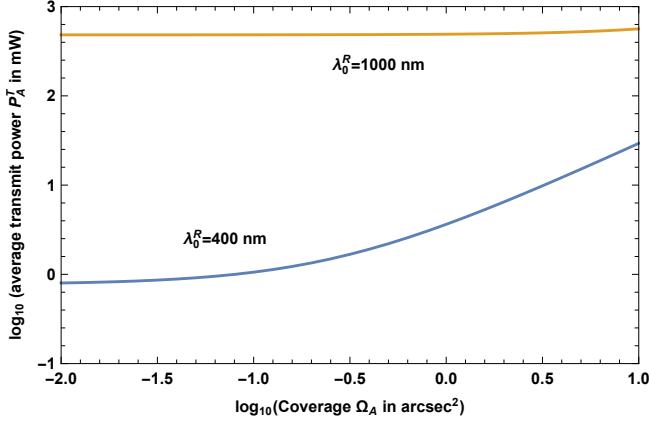


**Figure 10.** A log plot of the average transmit power  $P_A^T$  in mW against the coverage solid angle  $\Omega_A$ , with all other parameters taken from Tbl.1 and Tbl.2. Two wavelengths are plotted, and for small  $\Omega_A$  the required transmit power is much larger at the longer wavelength due to the greater relative sub-array sensitivity to interference and additionally the larger irradiance of a red-dwarf star.

ing other phases of the moon. Generally  $\Lambda_{N,moon}$  is the dominant sky noise source. Note that assuming  $\rho_{moon} < 1$  implies that some nighttime periods (with a brighter moon) are considered outages, and the actual data rate  $R_a$  will be correspondingly lower.<sup>22</sup>

#### 6.8.4. Daylight outage assumption

As is evident from Tbl.7, daylight would have a major impact on background radiation. For the swarm case in Tbl.2 the transmit power would be impractically large to achieve daylight operation ( $P_A^T = 5.8$  kW and  $P_P^T = 126$  GW). For this reason, the metrics in Tbl.2 and the following calculations assume nighttime (fullmoon) sky radiance. The value  $\rho_{moon} = 1$  in Tbl.2 and the following numerical calculations assume the entire nighttime is a non-outage condition, barring weather events. Since the receiver is aware of day-night and weather conditions, it can force complete erasures during daytime and weather events, and these become outage conditions in the sense of §10.4. Knowledge of the receiver's day-night or weather conditions is fortunately not necessary at the probe transmitter.

#### 6.8.5. Average transmit power

The average transmit power  $P_A^T$  is plotted in Fig.10 as a function of coverage solid angle  $\Omega_A$ . This shows that the shorter wavelength is quite advantageous, es-

<sup>22</sup> Strictly speaking when  $\rho_{moon} = 0$  there will be some black body atmospheric radiation, but this is neglected since this irradiance is dominated by Zodiacal radiation  $\Lambda_{N,zodi}$  from the solar system. This case is also uninteresting since there would be 100% outages.

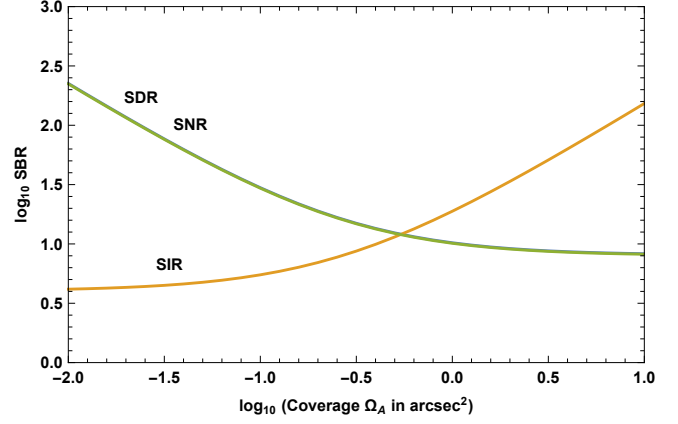


**Figure 11.** As an aid to understanding the small-coverage behavior exhibited in Fig.10, the log of the three components of  $SBR=4$  are plotted vs coverage solid angle  $\Omega_A$  for  $\lambda = 400$  nm. For small coverages SIR is the smallest, and hence interference is the dominant source of background radiation.

pecially so at smaller coverages (where interference is more significant).

The differing behavior at the two wavelengths can be better understood by comparing three components of SBR: Interference (SIR), noise (SNR), and dark counts (SDR). The smallest component is the dominant source of background radiation. At the shorter wavelength (see Fig.11)  $\Lambda_D^S$  was chosen so that noise and dark counts are equal contributors to background radiation, and hence  $SNR \approx SDR$  for all coverages (since neither noise nor dark counts are dependent on sub-array effective area). Interference is an insignificant contributor compared to moonlight and dark counts at the larger coverages.

At the longer wavelength (see Fig.12) interference becomes the dominant contributor to SBR at all coverages. As a result, the dark count target could be considerably relaxed without a substantial impact on overall performance metrics, but of course that performance would be considerably degraded relative to the shorter wavelength.

#### 6.8.6. Number of sub-arrays

SBR is determined by the design of the sub-array and the choice of  $P_A^T$ , and remains fixed during the scale-out to the entire receive aperture. The purpose of sub-array replication in scale-out is to increase the average detected photons per slot  $K_s^R$  to the value needed to achieve reliable recovery of scientific data in the face of shot noise. The value of  $K_s^R$  and hence the number of sub-arrays  $N^S$  does not depend on the data rate  $\mathcal{R}_0$ . The resulting  $N^S$  is very large, as plotted in Fig.13.

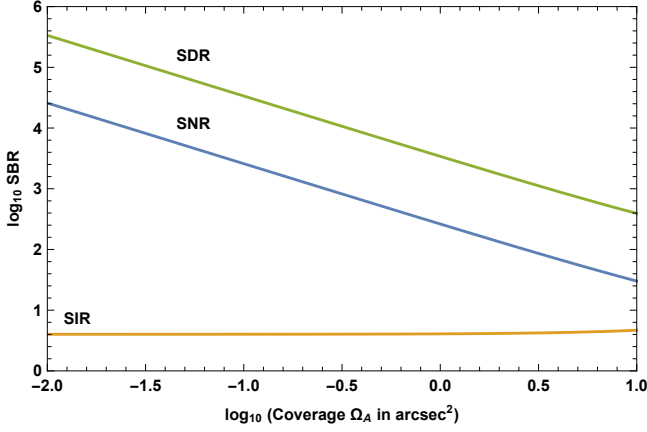


**Figure 12.** Fig.11 is repeated for  $\lambda = 1 \mu\text{m}$ . The interference becomes dominant for all coverages.

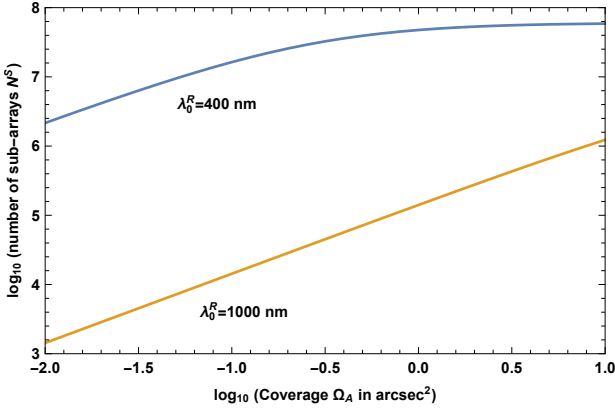


**Figure 13.** A log plot of the number  $N^S$  of sub-arrays under the same conditions as Fig.10. It is significantly larger at the shorter wavelength, which is due to (a) the smaller-area sub-array and (b) the smaller peak transmit power  $P_P^T$ .

The metric  $N^S A_e^S$ , which is a measure of the total effective area across all sub-arrays,<sup>23</sup> is plotted in Fig.14. It is significantly larger at the shorter wavelength, with the compensating benefit that the probe's average transmit power is lower (see Fig.10).

#### 6.8.7. Dark counts

To see the effect of changing dark-count rates,  $P_A^T$  is plotted in Fig.15 and Fig.16 as a function of dark counts, coverage angle, and wavelength. This quantifies the obvious conclusion that the shorter wavelength and a very low rate of dark counts are advantageous in achieving low average transmit power. Reducing the solid angle of coverage is also advantageous.

<sup>23</sup> This is not the effective area of the receive aperture as a whole, which is not defined since the receive aperture is not single-mode and not diffraction-limited.

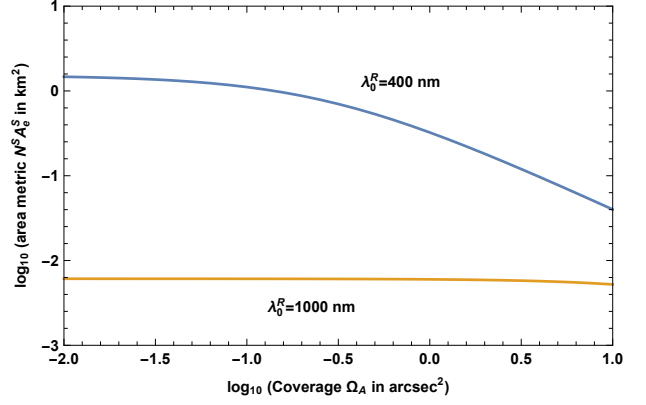


**Figure 14.** Based on the sub-array effective area  $A_e^S$  in Fig.9 and the number  $N^S$  of sub-arrays in Fig.13, a log-plot of their product  $N^S A_e^S$  in  $\text{km}^2$  as a function of the coverage. Generally it is less than a  $\text{km}^2$  under these ideal conditions, except for very small coverages.

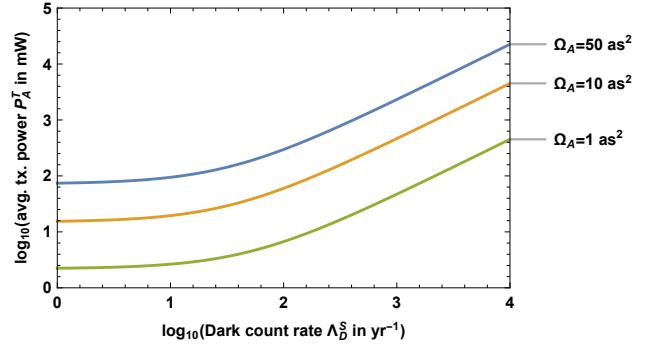


**Figure 15.** A log-log plot of the average transmit power  $P_A^T$  for  $\lambda = 400 \text{ nm}$  vs the average dark counts  $\Lambda_D^S$  per year (when referenced to individual sub-array optical detectors). Sharing optical detectors across multiple sub-arrays may be helpful in reducing  $\Lambda_D^S$  (see §2.10.4). Idealized performance is assumed for other physical characteristics like quantum efficiency, pointing accuracy, and atmospheric refraction and turbulence. The different curves illustrate the benefit of reducing the coverage angle. The highest dark count rate  $\Lambda_D = 10^4 \text{ yr}^{-1}$  corresponds to  $1.14 \text{ hr}^{-1}$ .

#### 6.8.8. Coronagraph

The effect of changing the coronagraph rejection is illustrated in Fig.17. The value of  $F_c$  makes a substantial difference at low dark count rates because that is where interference dominates.

#### 6.8.9. Slot time and average transmit power

In BPPM reducing the slot duration parameter  $T_s$  reduces the effective dark count rate (by reducing the duty cycle  $\delta$ ). The resulting benefit of  $T_s$  on reducing average transmit power  $P_A^T$  is illustrated in Fig.18. There is, however, a point of diminishing returns as interference becomes the dominant source of background radiation.

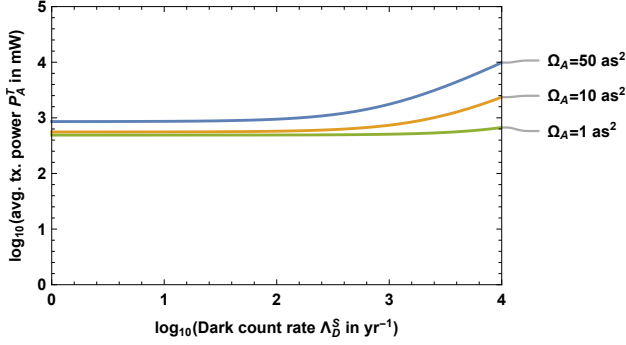


**Figure 16.** Fig.15 is repeated for  $\lambda = 1 \mu\text{m}$ . A floor in transmit power appears because interference becomes the dominant contributor to SBR for small dark count rate  $\Lambda_D^S$ . (see Fig.10 and Fig.12).

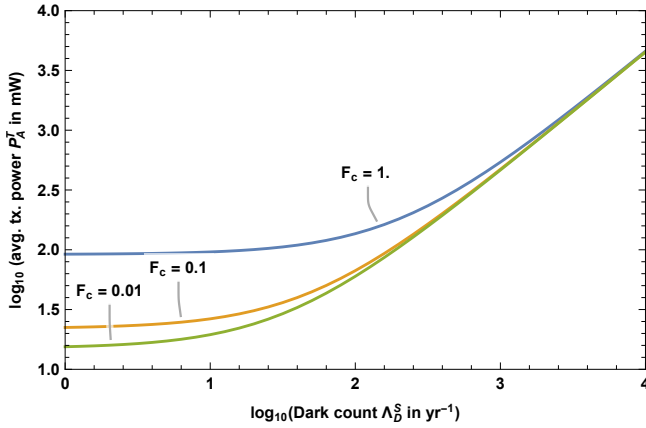


**Figure 17.** Fig.15 is repeated with three different values for the coronagraph rejection  $F_c$ . At low dark count rates the interference becomes the dominant source of background radiation.

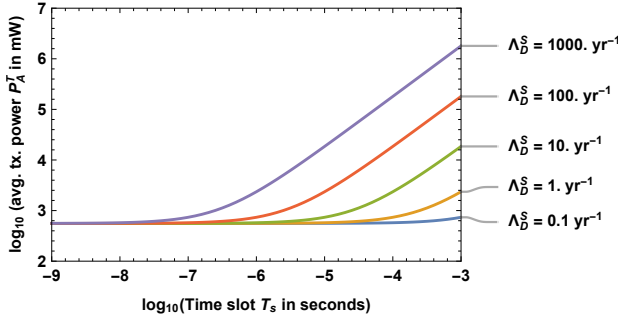


**Figure 18.** A log-log plot of the average transmit power  $P_A^T$  vs slot time  $T_s$  (between 1 ns and 1 ms) and different values of dark count rate  $\Lambda_D^S$  in  $\text{yr}^{-1}$ . The largest feasible value (at  $\delta=1$ ) is  $T_s=0.98$  ms. Reducing  $T_s$  also reduces  $P_A^T$  due to its beneficial limiting of dark counts. However, the benefit saturates at small  $T_s$  as interference dominates there.

#### 6.8.10. Slot time and peak transmit power

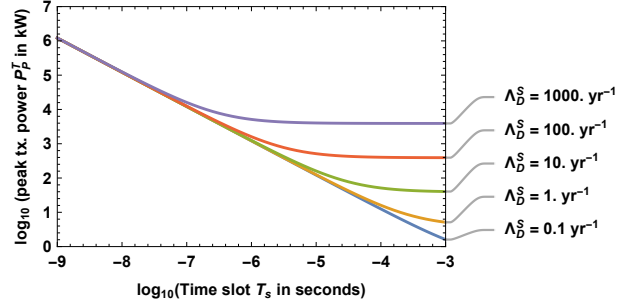


**Figure 19.** Fig.18 repeated for peak transmitted power  $P_P^T$ .

As seen in (9), the peak transmit power  $P_P^T$  is not dependent on  $\mathcal{R}_0$  or BPP, but rather is determined by the BPPM parameter  $T_s$  and data reliability parameter  $K_s^R$ . The effect of  $T_s$  on peak transmit power  $P_P^T$  is shown in Fig.19. Increasing  $T_s$  reduces  $P_P^T$  because the pulse energy  $P_P^T T_s$  remains relatively fixed. This effect saturates at larger  $T_s$  because the increase in  $P_A^T$  seen in Fig.18 indirectly offsets any reduction in  $P_P^T$ . The peak power increases for smaller  $T_s$  (where dark counts have been largely suppressed) because the average power is relatively constant in this interference-dominated regime.

For the other parameters chosen in Fig.19, the best choice of slot time is  $T_s \sim 1 \mu\text{s}$ . Any smaller  $T_s$  than this and  $P_P^T$  increases, and any larger  $T_s$  results in an increase in  $P_A^T$ . However this tradeoff is influenced by the assumed dark count rate  $\Lambda_D^S$ .

#### 6.8.11. Moonlight variation

The assumed outage probability assumes that the downlink operates during all moon phases. There is an opportunity to reduce the transmit powers if operation is restricted to reduced moonlight by choosing  $\rho_{\text{moon}} < 1$ , but of course the outage probability will also increase. This effect on transmit power is quantified in Fig.20.

#### 6.8.12. Excess optical bandwidth

If it is necessary for some reason to choose a  $W_e$  that is significantly larger than the minimum value  $T_s^{-1}$ , the noise and interference (but not dark count) contributions to background at the optical detector are increased. In this event probe transmit power has to be increased to maintain the desired SBR, and dark counts become relatively less important. The effect of increasing  $W_e$  on average transmit power  $P_A^T$  is plotted in Fig.21.

#### 6.8.13. Quantum efficiency

The preceding results assume ideal quantum efficiency  $\eta = 1$ . A quantum efficiency  $\eta < 1$  has two effects. First it will always increase  $N^S$  (and hence total receive aperture size) to achieve the required average photon rate  $\Lambda_A^R$ . Second, it will increase the relative importance of

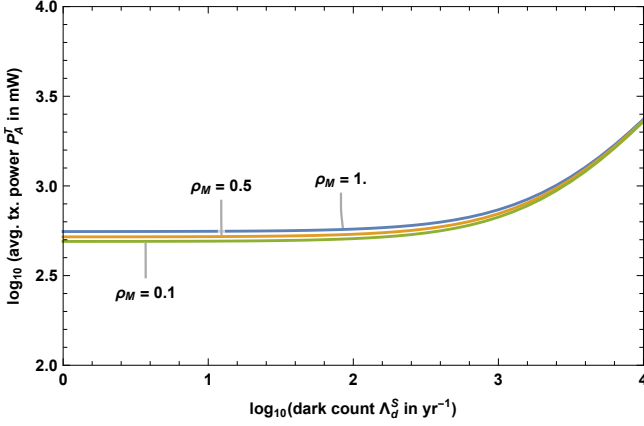


**Figure 20.** Fig.15 is repeated with all parameters held constant except the maximum moonlight irradiance parameter  $\rho_{moon}$ . Note that reducing  $\rho_{moon}$  implies a larger outage probability and hence a lower post-outage data rate  $\mathcal{R}_a$ . For larger  $\Lambda_D^S$  a smaller  $\rho_{moon}$  has little benefit since dark counts are the dominant source of background radiation.

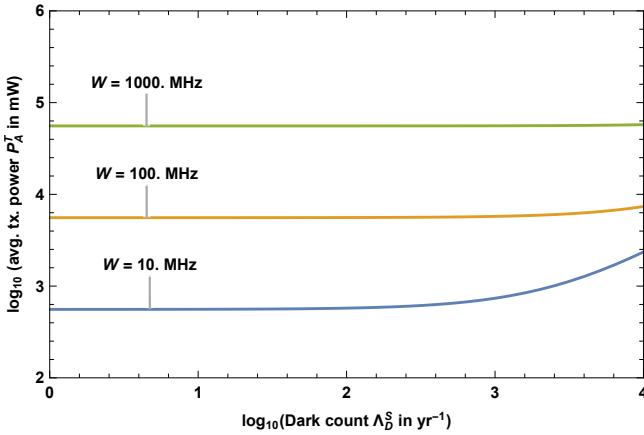


**Figure 21.** Fig.15 is repeated while varying the receive optical bandpass filter bandwidth  $W_e$  and keeping  $T_s$  fixed. The minimum is  $W_e=10$  MHz corresponds to  $W_e T_s = 1$ . In the interference-dominated regime the average transmit power is increased (in proportion to  $W_e$ ), and in principle this could be compensated by a higher coronagraph rejection ratio.

dark counts to SBR, and require an increase in transmit average power  $P_A^T$  in the regime of large dark count rates. This latter effect is illustrated in Fig.22.

### 6.9. Adjustments to power and aperture area

The nominal design presented thus far has focused on achieving the absolute minimum transmit power-area metric  $\xi_A^T = P_A^T A_e^T$  subject to a coverage  $\{\Omega_A, A_e^S\}$  constraint and photon efficiency BPP assumption. Relative to this nominal design, it may be of interest to reduce the number of sub-arrays  $N^S$  for budgetary or operational limitations, which would have to come at the expense of larger transmit power at the probe. Or it may be of in-

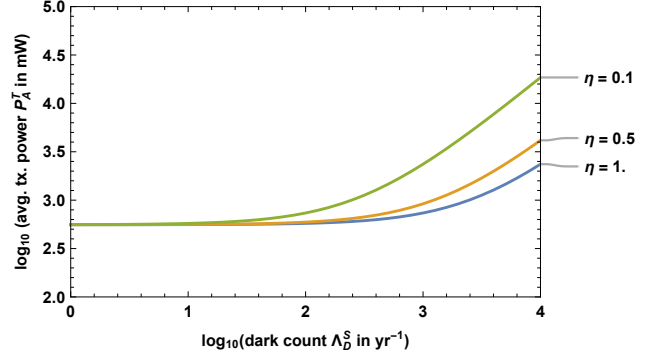


**Figure 22.** Fig.15 is repeated with all parameters held constant except the optical efficiency  $\eta$ . The average transmit power  $P_A^T$  has to be increased to maintain a fixed SBR at higher dark count rates  $\Lambda_D^S$  since received power is reduced but  $\Lambda_D^S$  is unaffected. The adverse impact of  $\eta$  on  $P_A^T$  is reduced for very small  $\Lambda_D^S$  since in that regime noise and interference (as well as signal) are reduced and thus SBR is relatively unaffected.

terest to further reduce the transmit power-area metrics  $\xi_{A,P}^T$  to reduce the probe mass, which would somehow have to come at the expense of increasing  $N^S$ . Ideally in both cases the changes would be efficient, as instrumented by unchanging end-to-end metrics  $\xi_{A,P}^{TR}$  (see §6.1). We now explore each of these possibilities. In summary,  $N^S$  can be simply reduced (at the expense of larger  $\xi_{A,P}^T$ ) by increasing the assumed SBR, and increasing  $N^S$  (with the benefit of smaller  $\xi_{A,P}^T$ ), albeit somewhat inefficiently, follows from a reduction in the assumed BPP.

#### 6.9.1. Reducing number of sub-arrays

$N^S$  can be reduced by increasing the signal level at the sub-array, which is indirectly represented by the parameter  $K_s^S$ . The previous results have minimized  $K_s^S$  by choosing it to just achieve the desired SBR. Increasing  $K_s^S$ , and thereby reducing  $N^S = K_s^R / K_s^S$ , can be accomplished by increasing the SBR objective. This doesn't affect  $\xi_A^{TR}$  in (8), and thus reduces  $N^S$  at the expense of increasing  $\xi_A^T$ . This is illustrated by (Parkin 2019), where the design methodology focuses on minimizing the receive aperture area (by constraining  $N^S=1$  without regard to the adverse impact on transmit power).<sup>24</sup> As observed in (10), for the typical values of  $N^S$  in Fig.13 the impact of constraining  $N^S=1$  on the transmit power-area metric  $\xi_{\{A,P\}}^T$  is in the range of three to eight orders of magnitude (depending on wavelength and coverage).

<sup>24</sup> The minimum-SBR value of  $N^S$  is determined by both the choice of SBR and the details of the background radiation model and assumptions, both of which differ substantially in (Parkin 2019). Thus a numerical comparison is not attempted.

In effecting this tradeoff, SBR is constrained on both ends:

- On the downside, SBR has to be large enough that the expected BPP can be achieved (see §E). The nominal SBR=4 in Tbl.2 is chosen with this in mind.
- Since we must have  $N^S \geq 1$ , it follows that  $K_s^S \leq K_s^R$ , placing an upper bound on SBR. For our nominal design (ignoring the extinguishment factor<sup>25</sup> (13)) this bound is  $SBR \leq 2.4 \cdot 10^8$ .

### 6.9.2. Further reducing transmit power

Heretofore and in Tbl.2 we have assumed a high photon efficiency BPP. The primary motivation for a large BPP is a smaller total area for the receive aperture, because the assumed data rate  $\mathcal{R}_0$  can be achieved with fewer photon detection events and hence with fewer sub-arrays  $N^S$ . Is a lower BPP ever advantageous? Surprisingly the answer is yes. Based on (8), lowering BPP increases  $\xi_A^{TR}$  and thus adversely impacts the overall end-to-end efficiency. However, as we will now see it also reduces  $\xi_A^T$ , which can be helpful in reducing probe mass, inefficiently trading this off against a larger receive aperture area  $A_e^S N^S$ .

In PPM, BPP is controlled by adjusting the bits per PPM slot  $m$ , with BPP  $\approx 0.9m$  for the nominal value of  $K_s$ . For conventional PPM, reducing  $m$  also beneficially increases time-slot duration  $T_s$ , and thus reduces optical bandwidth  $W_e$  and thus  $\Lambda_{I,N}^S$  in Tbl.6. For BPPM, holding  $T_s$  and  $W_e$  fixed imply that  $\Lambda_{I,N}^S$  remains fixed, but the frame duration  $T_F$  is proportional to  $2^m$  and thus reducing  $m$  has the effect of reducing background photon counts  $K_{X,I,N,D}^S$  in Tbl.5. Thus in both cases reducing  $m$  beneficially reduces the background and permits a commensurate reduction in  $\xi_A^T$  for fixed SBR.

The dependence of some key performance metrics on  $m$  (based on Tbl.5) are listed in Tbl.8, with all other parameters (and in particular  $\mathcal{R}$ ,  $A_e^S$ , and  $T_s$ ) remaining fixed.<sup>26</sup> The peak and average transmit powers as a function of  $m$  are plotted in Fig.23, and the total receive aperture effective area is plotted in Fig.24, in each case for two coverage solid angles  $\Omega_A$  (the solid and dashed curves). Note that reducing  $m$  has a larger effect in reducing peak power than average power because of the decreasing peak-to-average ratio PAR. For small  $m$  the receive aperture area becomes truly gigantic, particularly for the smaller coverage case, because the lower BPP must be compensated by a larger receive aperture.

<sup>25</sup> As the signal level grows, SXR becomes the dominant contribution to SBR. However, as long as SXR is sufficiently large on its own accord, it is safe to assume  $F_x=0$  for the purpose of calculating SBR.

<sup>26</sup> Some metrics have a more complicated dependence on  $m$  when  $F_x \neq 0$ , so it has been assumed in Tbl.8 that the optical source completely extinguishes, or  $F_x=0$ .

**Table 8.** Dependence of performance metrics on photon efficiency as represented by bits per PPM slot

Metric		Dependence
Photon efficiency	BPP	$m$
Average transmit power	$P_A^T$	$2^{m-1}/m$
Peak transmit power	$P_P^T$	$2^{m-1}$
Number of sub-arrays	$N^S$	$2^{1-m}$
Transmit average power-area metric	$\xi_A^T$	$2^{m-1}$
Transmit peak power-area metric	$\xi_P^T$	$2^{m-1}/m$
End-to-end average power-area metric	$\xi_A^{TR}$	$1/m$
End-to-end peak power-area metric	$\xi_P^{TR}$	1

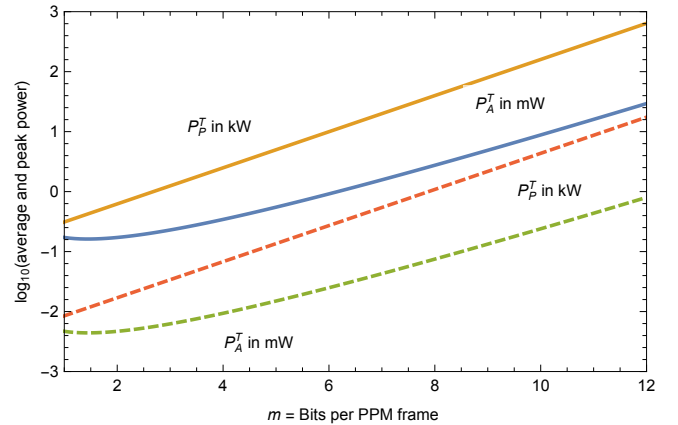


**Figure 23.** The dependence of peak and average transmit power on the bits per PPM frame  $m$ . A smaller  $m$  results in smaller transmit powers (both average and peak) due to the shorter PPM frame durations and the resultant decrease in background radiation events. The solid curves are for a larger coverage ( $\Omega_A=10. \text{ as}^2$ ) and the dashed curves for a smaller (single-probe) coverage ( $\Omega_A=0.01 \text{ as}^2$ ). For the latter the greater sub-array sensitivity results in smaller transmit powers.

## 7. ATMOSPHERIC EFFECTS

For a receive aperture located on the earth's surface, the interaction between signal and the earth's atmosphere at optical wavelength introduces several significant impairments (Biswas & Piazzolla 2006; Piazzolla 2009). Nighttime sky irradiance is a contributor to the total background radiation, and was incorporated into the numerical results of §6.8. The other significant atmospheric impact is a contribution to outage time due to daytime solar scattering and weather, which together reduce the rate of reliable scientific data recovery (see §6.2 and §10.4).

### 7.1. Daytime sky irradiance

During the daytime, sunlight scattered through the atmosphere into the receive aperture is a source of background radiation that can be considered isotropic within the coverage of a highly directive aperture. In Tbl.7

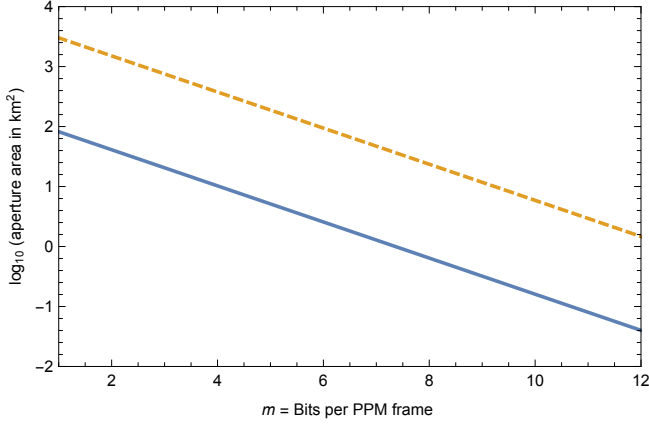


**Figure 24.** The total effective receive aperture area  $A_e^S N^S$  is plotted under the same conditions as Fig.23. Reducing  $m$  results in a larger area commensurate with the lower transmit powers. For a smaller coverage, the smaller transmit power is traded against a larger receive aperture area. Overall a reduction in  $m$  trades a larger receive aperture area for smaller transmit powers, but per Tbl.8 this tradeoff is inefficient in the sense that the end-to-end average power-area metric  $\xi_A^{TR}$  increases as  $m$  decreases.

the sky irradiance at the sub-array can be inferred from Fig.8.16 in (Piazzolla 2009):

$$P_N^S = 3 \times 10^{-3} \text{ W}/(\text{cm}^2\text{-sr-}\mu\text{m}) @ \lambda_0^R = 1\mu\text{m}$$

$$\Lambda_N^S = P_N^S \cdot \frac{\lambda_0^R}{hc} \cdot \frac{W_e(\lambda_0^R)^2}{c} \cdot (\lambda_0^R)^2 \text{ ph/s-Hz.}$$

The factors in the conversion from  $P_N^S$  to  $\Lambda_N^S$  are (1) the power to photon rate conversion, (2) the bandwidth expressed in terms of frequency rather than wavelength, and (3) the  $A_e \Omega_A$  product given by (B5). The value of  $P_N^S$  is about  $8 \times$  larger at  $\lambda_0 = 400 \text{ nm}$  and a factor of  $4 \times 10^5$  smaller for a full moon as compared to daylight.

This irradiance decreases with greater angular separation from the sun itself, and it helps that there is a large minimum angular separation between Alpha Centauri and the sun.<sup>27</sup> Although the solar radiance is maximum at 475 nm (corresponding to black body radiation at 5800 K), the sky irradiance is smaller at 400 nm than at 1  $\mu$  largely due to the smaller value of  $A_e \Omega_A$ . The resulting numerical values are listed in Tbl.7.

Unfortunately the full daylight sky irradiance in Tbl.7 is more than four orders of magnitude larger than the other sources of noise background. The significance of this depends on the relative intensity of interference and dark counts, but generally operation during daylight hours would require significantly higher probe transmit

<sup>27</sup> In heliocentric coordinates the latitudinal separation is approximately fixed at 44.7 degrees and the longitudinal separation varies through the year.

peak power. Thus in Tbl.2 (as discussed in §6.8.4) we assume that daylight is an outage situation.

### 7.2. Nighttime sky radiance

If daylight is considered an outage, the sky radiance during nighttime is a limiting factor on the downlink. At night the reflected light from the moon is an indirect source of solar background radiation (except for a new moon or the moon below the horizon). A full moon has a  $4 \times 10^5$  smaller radiance than the sun. In the absence of moonlight, the primary source of irradiance is thermal emissions from the atmosphere, but this will be considerably smaller than cosmic zodiacal radiation for the wavelengths of interest as long as strong emission lines (such as OH or O<sub>2</sub>) are avoided in the choice of wavelength. Thus, the total night sky irradiance as a fraction  $\rho_{moon}$  of the full moon value (as determined by the moon’s phase) is the approximation employed earlier.

### 7.3. Turbulence

Atmospheric turbulence causes a short-term fluctuation in received signal power which is manifested as a scintillation (random variation in signal strength) as well as signal incoherence (wavefront phase aberration across the sub-array area). As the geometric size of a sub-array increases, the variation in signal power due to scintillation decreases, while the power loss due to spatial incoherence increases (Piazzolla 2009).

As the sub-array geometry is determined by coverage considerations, scintillation manifests itself as a variation in erasure probability that can only be compensated by considering high erasure probability as an outage, which is mitigated using interleaving and ECC (see §10.4) rather than adjustment of the sub-array design.

Spatial incoherence is a less severe impairment during nighttime operation, and under some conditions may be deemed an outage. It can in principle be compensated by adaptive optics (the details are discussed in Sec.3.34 of (Biswas & Piazzolla 2006)). As to whether adaptive optics will be necessary depends on the detailed consideration of elevation, declination, and the geometric size of the sub-array (rather than its area), all of which is beyond the scope of this paper. Fortunately, for the larger coverages necessary in the probe-swarm case the sub-array is smaller and thus less susceptible to atmospheric turbulence.

### 7.4. Outages

Periods during which virtually all PPM frames suffer an erasure are considered outages. Generally the transmitter will have no knowledge of when outages occur, but when there is no “fuel” saving from avoiding transmission during outages this has no consequences. The outage mitigation design can assume a worst-case outage probability  $P_E$ , with the consequence that the data rate is reduced by a factor of  $(1 - P_E)$  (see §10.4).

There are two main sources of atmospheric-origin outages are daylight and weather. Weather, including water vapor, clouds, and storms attenuate or block reception at random times. The statistics of weather outages is highly site-dependent. The receiver is aware of either of these conditions and can enforce (and label) outages by arbitrarily enforcing 100% erasures during these periods.

For any point on earth, nighttime lasts for half the hours averaged over one year (actually slightly less due to refraction of sunlight near the horizon). Near the Antarctic Circle nighttime persists for 48% of the total hours in a year (Wikipedia contributors 2019). Thus treating daylight as an outage would reduce the scientific data rate by 52% at this location.

The siting of the receiver will introduce another source of outages if its latitude results in the target star disappearing below the horizon. In the case of Proxima Centauri, continuous view is possible if the receiver is sited at a sufficiently southerly latitude<sup>28</sup>.

## 8. OTHER CHALLENGING DESIGN ISSUES

BPPM addresses principally the technology limitations of optical bandpass filters and detectors. Other issues relating to the design of the physical layer arise that impose profound technological challenges.

### 8.1. Probe motion effects

A low-mass probe is assumed to be traveling (relative to the receiver frame) at relativistic speed, and the receiver is also in motion due to earth rotation and orbit. When referred to baseband, due to the short optical wavelength the resulting Doppler shifts must be accounted for in the design (see §A.1).

#### 8.1.1. Uncertainty in probe velocity

At a speed of  $u = 0.2c$  the combined Doppler shift (about 20%) and effect of time dilation (about 2%) is about 22%. Since the sources of noise and interference do not experience this shift, the shifted wavelength determines the atmospheric effects and interference from the target star. The transmit wavelength can be adjusted toward a shorter wavelength to compensate for the Doppler shift.

Since the swarm of probes will encompass slightly different speed perturbations, the result is relatively large frequency offsets affecting WDM (see §8.2) and TDM (since a common receive wavelength is assumed). If we allow a perturbation  $du$  in speed  $u$ , the resulting per-

turbation  $d\nu_R$  in received frequency  $\nu_R$  is

$$\frac{d\nu_R}{\nu_R} = -\frac{u/c}{1 - (u/c)^2} \cdot \frac{du}{u} = -0.208 \cdot \frac{du}{u} \quad (14)$$

for  $u = 0.2c$  (see §A.2). Thus there is a Doppler shift of  $\pm 1.6$  THz for each  $\pm 1\%$  variation in probe velocity at  $\lambda_0 = 400$  nm.

Achieving a precision in probe velocity that limits the Doppler shift to the order of  $\sim W_e$  seems unlikely. If probe speed cannot be controlled tightly enough, it will be necessary to compensate for variations in probe speed by a coordinated configuration of transmit wavelength following launch. There are at least two possible options:

- Since the transmission of scientific data follows encounter, transmit wavelength configuration can follow encounter and precede downlink operation. Autonomous configuration of transmit wavelength could be based on a sufficiently precise measurement of time to reach the target star, combined with knowledge of target star position. All probes in a swarm will be affected equally by imprecision in knowledge of this position.
- If there is an earth-to-probe communication uplink for a short period following launch (see §8.4), the received wavelength can be measured at the receiver and used to configure the transmit wavelength.

#### 8.1.2. Earth motion and Doppler

The maximum speed of the earth relative to a heliocentric frame due to its orbit about the sun (or revolution about its axis) is 30 km/s (or 1670 km/h at the equator). The Doppler shift is thus bounded by  $\pm 30$  GHz (or  $\pm 464$  MHz) at  $\lambda = 1 \mu\text{m}$ . While this Doppler can be very significant, it is essentially the same for all probes in a swarm and thus does not appreciably affect their relative wavelengths. Accurate positioning of the receiver's optical bandpass filtering does require correction based on accurate knowledge of this motion, and any remaining uncertainty should be accounted for by an increase in bandwidth  $W_e$  with the resulting increase in cosmic sources of background radiation (see §6.8.12).

#### 8.1.3. Gravitational red shift

During flyby of the target star, the stronger gravitational field will result in incremental red shift of the probe's signal. While this effect can be significant for a close-in encounter, it is largely avoided with post-encounter commencement of downlink transmission. In any case downlink operation during encounter is unlikely due to conflicting demands on scientific instrument electrical power and probe attitude adjustment to accommodate scientific observations.

<sup>28</sup> The declination of Proxima Centauri is -62.67 degrees, so a continuous view is achieved by choosing a receiver site with a latitude more southerly than  $(90 - 62.67) = 27.33$  degrees south. However, to avoid significant degradations in link quality when Proxima Centauri is low on the horizon due to increased atmospheric degradation effects, the receiver site should be more southerly than approximately 35 degrees south.

#### 8.1.4. Influence on data rate

Due to the increasing propagation delay and time dilation in the transmitter clock relative to the receiver, the data rate observed by the receiver is smaller by about 22% than the data rate generated at the transmitter. Due to the methodology adopted in §C, which concentrates on the earth's rest frame, the data volumes and latency plotted in Fig.5 account for this.

#### 8.1.5. Relativistic aberration

The high speed of the transmitter moving away from the receiver will have a relativistic effect on the transmit beam and affect the link budget of (6). This small incremental effect is not accounted for in this paper.

### 8.2. Multiplexing options

Multiplexing is the function of separating the signals and data from concurrent probe transmissions (see §2.5.3). Whether there is a single shared receiver or multiple receivers, this function is challenging due to environmental factors like extremely low received power and frequency shifts due to probe motion.

These challenges are magnified as the number  $J_p$  of concurrent transmitting probes increases, yielding strong motivation to minimize  $J_p$ . Available measures include, for each probe, limiting transmission during transit and limiting the downlink operating time. We find in §3 that (for a specific set of scaling laws) the optimum downlink time ranges from 2-9 years. For weekly probe launches this results in  $J_p \sim 100$  to 500.

There are some alternative multiplexing approaches. The multiplexing method affects many other aspects of the downlink design, so it should be established early.

#### 8.2.1. Spatial-division multiplexing (SDM)

SDM takes advantages of angular differences between probe trajectories to separate the signals from the probes. For probes launched at different times of the year, the parallax variation combined with a drift in the launch targets due to proper motion of the target star will spatially separate trajectories save for short-lived periods of exact coincidence (see §5). This opens up the possibility of choosing a receive aperture coverage to attenuate all probe signals save one of interest, with any coincidences treated as an outage (see §10.4). Proper motion of the target star is particularly helpful for spatial separation, as it opens up the possibility of combining SDM with another scheme for separating the signals from probes with nearby launch dates.

An extreme case is to use a separate receive aperture for each downlink, each with a very small coverage solid angle  $\Omega_A$  (as implicitly assumed in (Parkin 2019)). Although extravagant in terms of ground-system cost, an important benefit is the reduction in the required transmitter power-area product  $\xi_A^T = P_A^T A_e^T$  if  $N^S$  is chosen to minimize this value. However, this smaller  $\xi_A^T$  may

come at the expense of a considerably larger total effective area  $N^S A_e^S$  as seen in Fig.14.

An intermediate case would be a more sophisticated single-aperture design that employs time-dependent beamforming to separate probe signals. In effect each sub-array would constitute a multiple-pixel receive optical system, with one pixel dedicated to each probe.

#### 8.2.2. Wavelength-division multiplexing (WDM)

In WDM each probe is assigned a different wavelength at the receiver, with an optical bandpass filter and dedicated optical detector servicing each probe. WDM requires precise transmitter wavelength control, which is a challenge complicated by Doppler shifts (see §8.1.1 and §8.1.2) and implementation of a serial bank of optical bandpass filters to separate signal from different probes (see §9.2).

#### 8.2.3. Time-division multiplexing (TDM)

In TDM probe transmissions are assumed to not overlap one another in time at the receiver. Ideally those transmissions are at a common received wavelength, allowing for a single optical bandpass filter and detector. TDM requires precise transmitter knowledge of time of arrival of its signal at earth, which requires in turn a very precise clock and precise knowledge of its own trajectory (see §8.3).

#### 8.2.4. Random-access multiplexing

This is a variation on TDM in which transmissions have a low duty cycle and are randomized so that the probability of overlapping receptions in the receiver is small (Abramson 1994). This may be natural in combination with BPPM, which trades higher peak power for low duty cycle (see §2.12). Collisions at the receiver could be treated in a similar way to outages (see §10.4), although they would complicate the ECC by causing frame errors rather than erasures.

#### 8.2.5. Code-division multiplexing (CDM)

In CDM probes are assigned mutually orthogonal spreading sequences, which allows their signals to be separated (by cross-correlation with the spreading sequences) in spite of both wavelength- and time-overlap. It is useful to think of CDM as maintaining orthogonality using a different orthogonal basis for signals, where the basis functions do not align with either time or frequency (see §9.1.3).

For equivalent per-probe data rates  $\mathcal{R}$ , to first order WDM, TDM, and CDM all expand the *total* optical bandwidth by a factor of  $J_p$ . In the case of TDM this is because each probe has to transmit at rate  $J_p \mathcal{R}$  during its assigned time slot, and for CDM the spreading sequence expands the bandwidth of each probe's signal by a factor of  $J_p$ . In practice the bandwidth is larger after accounting for guard bands (WDM) and guard times

(TDM) due to imprecise knowledge of wavelength and time at the probes. As illustrated by BPPM, any form of TDM will also increase the peak transmitted power requirement commensurate with  $J_p$ .

### 8.3. Probe navigation

Relative to an (approximate) inertial frame defined by the Solar System and target star, the probe needs to be self-aware of the time and position for both the probe itself and for earth, for a couple of purposes. First the scientific instrumentation and interpretation of its data requires knowledge of the probe trajectory, hopefully with an accuracy less than a fraction of an AU. Second, accurate pointing of the transmit aperture so that the maximum signal power reaches the terrestrial receive aperture requires accurate knowledge of the angle and distance of the earth at the later time of arrival (see §8.5).

For these purposes the probe trajectory is parameterized by the probe elapsed time, the observed probe speed, and the observed angle of the sun's and the target star's position. There at least a couple of sources of imprecision in these estimates. First, after 30 yr the variation in elapsed time measured by a probe clock is 16 min for each one part in  $10^{-6}$  variation in oscillator frequency.<sup>29</sup> Second, at 4 ly and a nominal speed of  $0.2c$  the variation in propagation time is  $\pm 72$  days for each  $\pm 1\%$  variation in probe speed. Thus a speed variation is generally a much bigger issue in accurate pointing toward an orbiting earth than is clock accuracy. Thus a Xtal oscillator without temperature compensation aboard the probe may suffice for onboard estimate of elapsed time, and whatever method is used for speed measurement and compensation for Doppler shifts (see §8.1.1) also applies to estimating propagation time.

### 8.4. Uplink for probe configuration

Both navigation and Doppler shift considerations argue in favor of a communication uplink capability to estimate actual probe speed, which allows configuration of transmit wavelength and more accurate estimation of signal propagation delay. Such a capability may also be needed to actively correct a probe trajectory for flyby sufficiently near the target star.

Following the termination of the propulsion phase, the probe could transmit a signal toward earth, and a broadband receiver could measure both the actual trajectory of the probe and the signal wavelength. Navigation and wavelength correction factors can be transmitted back to the probe using the data uplink. An uplink transmit power can be large with a relatively short the propagation distance, simplifying the probe's uplink receiver. If

<sup>29</sup> Relative to terrestrial events the time elapsed on the probe is about 2% shorter than on earth, but this relativistic effect is known accurately and readily compensated.

a single aperture array is shared between launch, uplink, and reception, launch and uplink time becomes another contributor to downlink outage time for probes that were previously launched (see §10.4).

### 8.5. Probe attitude control

Attitude control of the probe is required for the scientific mission (orientation of instruments) and for communication (aiming the transmit beam back to its terrestrial communication receiver). The pointing accuracy required for the transmission downlink is undoubtedly the most critical requirement. A three-axis closed-loop correction by photon thrusters driven by the probe electrical power source has been proposed (Lubin 2016).

#### 8.5.1. Probe pointing accuracy

Assumptions as to receive aperture size are predicated on precise aiming of the probe's transmit beam to achieve the maximum power transfer. This can be based on probe attitude control or beam angle configuration relative to the probe, or some combination of the two methods. The sun and the target star can serve as references for pointing, requiring an image sensor and a probe attitude control loop. Initial acquisition is a non-trivial challenge not addressed here.

The angular radius of an Airy disk associated with a diffraction-limited transmit aperture is 2.5 arcsec for the parameters assumed in Tbl.2. Due to beam spreading with distance, the most stringent pointing accuracy is required at the closest proximity to earth. Expressed in terms of transverse radius of the presumed Airy beam as it passes through the Solar System, the Airy radius becomes 3.27 au at 4.24 ly distance and  $\lambda_R = 1 \mu\text{m}$ ., decreasing to 1.2 au at  $\lambda_R = 400 \text{ nm}$ .

Particularly at the shorter wavelength the beam must be aimed at the moving position of earth within its orbit at the future date/time of signal arrival, rather than the solar system. A larger transmit aperture (such as that assumed in (Parkin 2019)) would increase the required pointing accuracy accordingly.

#### 8.5.2. Attitude accuracy requirement

The probe attitude adjustment (or beam configuration) has to be controlled with a very tight tolerance. Viewed from an attitude perspective at the probe, the tolerances are very tight. A  $\pm 1$  arcsec tolerance on pointing angle corresponds to transverse alignment of the axis of transmission by  $\pm 4.8 \mu\text{m/m}$ . Primarily this is a burden for the image sensor tracking the sun's position, which must possess a *higher* resolution than for transmission. This suggests sharing a single aperture on the probe between transmission and sensing, with a larger portion of that aperture used for sun tracking than for transmission.

### 8.5.3. Attitude control operation

Fortunately the probe has no moving mechanical parts or fluids that contribute to attitude misalignment, so there are only three identifiable sources of attitude misalignment: motion of electrons within the probe electronics, the momentum transfer from the transmit beam, and (likely most significantly) collisions with interstellar material. This suggests that attitude adjustment and transmission should *not* occur concurrently, for several reasons:

- If attitude misalignment is infrequent the duty cycle of attitude adjustment may be low.
- The sharing of sub-apertures between sensing and transmission is a mass-saving measure that is easier if the two functions are not concurrent.
- Each function can utilize the entire available electrical power, maximizing the data rate and minimizing the time consumed by attitude adjustment.
- During periods of misalignment the data transmission is likely to be unreliable so this becomes an outage condition, whether the probe is transmitting or not.
- Any effect of transmission beam momentum interfering with attitude adjustment is minimized. If thrusters and communications utilize the same electrical source, then downlink transmission exerts an equivalent thruster force on the probe. If transmission occurs only during periods when the attitude is within a tight tolerance, since the probe trajectory is rectilinear the only significant effect of that force is a tiny increase in probe speed.<sup>30</sup>
- Although the suspension of transmission during periods of attitude adjustment slightly reduces the average data rate, the greater electrical energy available during each transmission can compensate for this with a higher nominal data rate.

### 8.6. Coronagraph function

The coronagraph function provides extra attenuation for interference originating at the target star (see §6.8.8). A receive sub-array shared over all transmitting probes in a swarm will have a coverage that includes probes just completing a target star encounter, and thus will have limited or no attenuation of the target star radiation. A requirement on the order of  $F_c=10^{-2}$  to  $10^{-4}$  follows (see §6.8.8), necessitating coronagraph-specific measures other than limiting the coverage angle.

There are various approaches, some of which are:

- Delay download transmission following encounter long enough for proper motion of the star to separate probe trajectories from the star (Parkin 2019).
- Arrange for a sub-array coverage to be limited to a single probe at a time (as assumed in (Parkin 2019)). This is accomplished by duplicating sub-arrays. Or with some forms of TDM, the coverage of a single sub-array can be switched to the single probe whose signal is currently being received.
- For a common sub-array implemented as a phased array of sub-apertures, implement multiple beams directed at the different probes.<sup>31</sup> To avoid a reduction in SBR this would have to be accomplished with high quantum efficiency and without amplification.
- Use techniques similar to those being pursued in the direct imaging of exoplanets, which also requires rejection of target-star radiation. These techniques include coronagraphs and interferometers (Traub & Oppenheimer 2010) and external occulters (also known as starshades) (Cash 2011). For example, a notch (high rejection) permanently located at the target star location might be added to the sub-array by adjusting the phase/magnitude in the combiner, thus creating a spatial filtering function (Lubin et al. 2018b).

The phase and magnitude in a phased-array combiner has to be implemented extremely accurately. Phases also have to be dynamically adjustable to account for parallax and the proper motion of the star (see §5).

A promising direction draws on advances in direct exoplanet imaging. However, some differences inherent to the downlink design challenge should be noted:

- For a ground-based observation platform, dynamic pointing of the aperture due to atmospheric refraction and atmospheric turbulence are issues.
- The optical bandwidth is narrow and the wavelength can be chosen to minimize the target star interference (see §6.8.3).
- A single probe downlink will typically operate for years (see §3) and a swarm of probes correspondingly longer.

## 9. CRITICAL TECHNOLOGIES

The tradeoffs quantified in §6.8 identify three technologies whose stringent requirements play a significant role in success or failure. These are the transmit light

<sup>30</sup> The trajectory curvature due to the target star gravitation will introduce a small momentum component transverse to the trajectory that needs to be accounted for.

<sup>31</sup> Such an approach is being explored at millimeter wavelengths for application to 5G cellular (Roh et al. 2014).

source, the receiver optical bandpass filtering, and the photon-counting optical detectors. It is clear that the current state of source and detector technologies is not consistent with the low-mass probe downlink application. Fortunately they can be expected to advance in the application timeframe (see §2.4), but this introduces considerable uncertainty. Fortunately we have not identified any limiting physical principles that impede future advances. Also, the configurable duty cycle  $\delta$  in BPPM beneficially offers a tradeoff among all three technologies, permitting some flexibility in their relative advancement (see §2.12).

### 9.1. Transmit light source

In an optical direct-detection communication system employing PPM and BPPM, high peak powers are fundamental to achieving high photon efficiency (Jarzyna et al. 2018). This is reflected in the theoretical limit of (3), which predicts a logarithmic relationship between the achievable BPP with reliable data recovery and PAR. High PAR is achieved by reducing slot time  $T_s$  and increasing peak power  $P_P^T$  to keep the pulse energy  $P_P^T T_s$  constant. This relationship of PAR and BPP is discussed in practical terms in §10. However this straightforward approach results in multiple-kilowatt peak powers (see Fig.19). Optical amplification of semiconductor laser outputs can attain Watt-level peak powers, and Q-switched lasers can attain kilowatt-levels but suffer from low electrical-to-optical conversion efficiency (Banaszek & Jachura 2017).

#### 9.1.1. Design parameter adjustment

The required peak power can be reduced by several adjustments in design parameters singly or in combination, although these unfortunately all trigger other issues. Reducing the coverage solid angle  $\Omega_A$  benefits the peak power because of the higher sensitivity of a large sub-array (see Fig.15), but the total receive aperture area is also increased (see Fig.14). Increasing the transmit aperture area  $A_e^T$  is effective if the power-area  $P_P^T A_e^T$  is fixed. Reducing the dark count rate results in lower peak power (see Fig.19), but the effect is limited by the continued presence of moonlight interference. Smaller peak power can be achieved by reducing the photon efficiency BPP and hence lower PAR (see Fig.23), but this requires very large total receive aperture area to compensate for the reduced efficiency (see Fig.24).

#### 9.1.2. Pulse compression

Optical interference can be used in place of emitting high powers directly from an optical source. A straightforward example of this is the ganging of multiple semiconductor lasers in the transmitter with an optical combiner. Unfortunately this approach is expected to be inconsistent with the low-mass objective.

Pulse compression technology is often used to generate narrow high-power optical pulses. It relies on

the observation that for two pulse shapes  $p_1(t)$  and  $p_2(t)$  with the same bandwidth  $W$ ,  $p_2(t)$  can be obtained from  $p_1(t)$  by a linear filter with transfer function  $F(f) = P_2(f)/P_1(f)$ , where  $P(f)$  is the Fourier transform of  $p(t)$ . For example, a pulse with constant envelope  $|p_1(t)| = A$  and approximate time duration  $T \gg 1/W$  can be converted to a pulse  $p_2$  with approximate time-duration  $1/W$  and envelope  $|p_2(t)| = A\sqrt{WT}$  if energy is conserved.<sup>32</sup> This process converts a longer lower-amplitude pulse into a narrower high-amplitude pulse with power gain equal to  $WT$  (the bandwidth-time product).

Pulse compression has to be performed in the optical domain, typically by creating targeted interference with arrangements of diffraction gratings (Treacy 1969) or prisms (Kafka & Baer 1987). This apparatus achieves wavelength-dependent group delays to align shorter- and longer-frequency components in time. A *structured receiver* approach has been proposed that uses more complex long-duration waveforms with matched filtering (Guha 2011). Due to the linearity of Maxwell's equations the pulse-compression filtering could be performed in the receiver, reducing the mass burden on the probe. However, while pulse compression works well in generating picosecond pulses, it would be difficult to generate 10 – 100 ns pulses as required in this application. This is because light travels distance of one meter in  $\sim 3$  ns in a vacuum, and such an optical apparatus would necessarily be physically large. Of course shorter pulses could be generated, but the required reduction in pulse duration and attendant increase in peak power would be counter-productive.

#### 9.1.3. Modulation code layer

The need for short pulses can be attributed to the choice of PPM for the modulation code layer, and it is intriguing to consider alternatives. One approach is to extend the code-division multiplexing idea described in §8.2.5 to the modulation coding layer for a single probe downlink.

Consider a set of  $L$  waveforms  $\{p_i(t), 1 \leq i \leq L\}$ , each bandlimited to  $W$  Hz and confined to time interval  $0 \leq t \leq T$  with the property that

$$\int_{-\infty}^{\infty} p_i(t)p_j^*(t) dt = \begin{cases} A & i = j \\ 0 & i \neq j \end{cases}$$

This requirement can be approximately satisfied whenever  $L \leq WT$ , with increasing accuracy as  $WT \rightarrow \infty$  (Slepian & Pollak 1961).

<sup>32</sup> A function bandlimited to  $W$  cannot be strictly time-limited, and a function time-limited to  $T$  cannot be strictly bandlimited. However these conditions can be approximated if  $WT \gg 1$  (Slepian & Pollak 1961). The narrow pulse  $p_2(t)$  violates this condition and will be only roughly confined to time duration  $1/W$ .

The modulation coding layer can transmit one of the  $L$  waveforms, and at the receiver a parallel set of filters (one matched to each possible waveform) can estimate which waveform was transmitted (Banaszek et al. 2019a). A PPM modulation code is a special case of this scheme with  $L = M \sim W_e T$ , where  $M$  is the number of slots in a PPM frame, and frequency-shift keying (FSK) is another. FSK and other options could intrinsically allow the light source to generate a waveform with constant power with duration  $T$  (rather than duration  $T/M$  as in PPM). However, there is a major disadvantage, and this is the need for  $L$  optical detectors, one for each matched filter, multiplying the total dark count rate accordingly. PPM has the unique property that a single optical photon-counting detector (with its dark counts) is needed.

Intermediate cases are possible. For example if  $M = I \cdot J$  then each candidate transmitted pulse could be confined to one of  $I$  time slots (each with duration  $T/I$ ) and one of  $J$  frequencies. Only  $J < M$  optical detectors would be needed.

### 9.2. Optical bandpass filtering

Bandpass filtering in the optical domain is a critical system component with several requirements that are challenging to achieve individually and collectively. Numerical results in §6.8.9 suggest a BPPM slot time  $T_s \sim 0.1 - 1 \mu\text{s}$ , which implies  $W_e \sim 1 - 10$  MHz. An optical bandwidth  $W_e$  larger than necessary results in larger cosmic source of background (see §6.8.12). At  $\lambda = 1 \mu\text{m}$ ,  $W_e = 1$  MHz results in a Q-factor (ratio of center frequency to bandwidth) of  $3 \times 10^8$ . Such Q's are being approached with recent technology.<sup>33</sup>

There are other requirements on the bandpass filtering. If WDM is used to separate the probe signals (see §8.2.2) we actually need a bank of bandpass filters with nearly adjacent passbands. To avoid signal attenuation, this filter bank has to be serial rather than parallel, with each filter splitting off the optical signal in one band while providing low insertion loss outside this designated passband. Further, the location of these passbands have to be agile to adjust to changing Doppler shift due to the earth's motion (see §8.1.2) and possibly also to adjust for variations in the probe transmit wavelengths (see §8.1.1).

### 9.3. Optical single-photon detectors

The numerical results point to the need for optical detectors with dark count rates that are extremely low (see §6.8.7). Superconducting detectors, which can successfully detect individual photons and have intrinsically low dark count rates, will be necessary.

Dark-count rates of  $\Lambda_D = 10^{-4}$  Hz have been reported for a superconducting nanowire detector (Shibata et al. 2015). This is two orders of magnitude higher than the objective of Tbl.2, which translates to  $\Lambda_D^S = 10^{-6}$  Hz. In (Shibata et al. 2015) the black body radiation from the connecting optics is reported as the major source of dark counts, and this source is substantively different than intrinsic dark counts in the detector itself since the dark count rate is proportional to optical bandwidth in the former and independent of bandwidth in the latter. Low dark count rates were obtained by inserting a cold 100 GHz bandpass filter between optics and the nanowire. However, the signal optical bandwidth in Tbl.2 is four orders of magnitude lower than this, opening an opportunity to further reduce the optics blackbody radiation.

In fact there is an opportunity to locate all the receiver optical bandpass filtering at the output of the optics and input of the optical detector. In this case the dark count rate originating as blackbody radiation in the optics would be comparable between PPM and FSK, since the total bandwidth  $W_e$  for the two modulation schemes are nominally equal (see §9.1.3). This example illustrates the intimate relationship between the design of the modulation coding and physical constraints and characteristics.

Superconducting detectors are intrinsically free of dark counts, but material impurities and external sources of radiation (radioactive decay and cosmic rays) may be an issue. Some other measures can be taken to minimize the dark-count rate, including the following ideas:

- Cryogenic cooling of the optics and other photonic elements.
- Better shielding of optics and detectors from external radiation.
- Many intrinsic dark counts may be manifested by out-of-band (higher-energy) photons, and these events may be recognizable in the electrical pulse amplitude at the detector output.
- Share a single optical detector over multiple sub-arrays, reducing the per-sub-array dark count rate accordingly (see §2.10.4). For example multiple fibers might be attached to a large-area detector. These fibers may need to be optically isolated, or this may be unnecessary at the extremely low photon detection rates expected.
- It is also feasible to operate with  $\text{SBR} < 1$ , although the theoretical photon efficiency falls off rapidly as SBR decreases in this regime. While this would allow for greater dark count rates, all else equal, it would have other negative consequences.

<sup>33</sup> For example cavity-based high-Q optical bandpass filters with  $Q = 8 \times 10^7$  are reported in (Spencer et al. 2014, 2012).

## 10. DATA RELIABILITY

Scientific data, especially after aggressive compression, must be recovered with very high reliability to maintain the integrity of scientific conclusions and outcomes. Achieving this high reliability in the face of impairments like noise and interference, atmospheric turbulence, and outages is a challenge. In the interest of a smaller receive aperture we seek high photon efficiency BPP (see §6.9.2), and this magnifies the challenge. Even after the aforementioned impairments are tamed, signal shot noise (a feature of the laws of quantum mechanics) places theoretical limits on the BPP that can be achieved consistent with reliable data recovery.

### 10.1. Reliability is the hard part

There is no theoretical limit on photon efficiency, if reliability is not demanded. The challenge is in *actually achieving* high reliability in the recovery of scientific data in spite of high photon efficiency. This is easily illustrated using the encoding scheme of PPM, one frame of which was illustrated in Fig.4c. The reliability challenge comes about because even with  $K_s^R$  average detected photons for each occupied slot (one out of  $M$ ), the actual number of photons is *random*. This is a manifestation of the signal shot noise.

Assuming no spurious photon detections from background radiation (this would be another source of randomness to overcome), let the number of detected photons  $Y$  in time interval  $T_s$  be a random variable, which quantum mechanics predicts has a Poisson distribution. If the slot in question is the one containing non-zero average power, and the average number of detected photons in this slot is  $E[Y] = K_s^R$ , then

$$\Pr \{Y = k\} = \frac{(K_s^R)^k e^{-K_s^R}}{k!}. \quad (15)$$

An erasure occurs in a PPM frame when no photons are detected in all  $M$  slots, and this erasure has to be mitigated by ECC. Based on (15), this event  $Y = 0$  occurs with probability  $\Pr \{Y = 0\} = e^{-K_s^R}$ .

Since one PPM frame communicates  $\log_2 M$  bits using an average of  $K_s^R$  detected photons, the photon efficiency is

$$\text{BPP} = \frac{\log_2 M}{K_s^R} = \frac{m}{K_s^R}. \quad (16)$$

Obviously  $\text{BPP} \rightarrow \infty$  as  $K_s^R \rightarrow 0$ , so achieving a large BPP is not an issue. The problem arises when we consider reliability, since a side effect of reducing  $K_s^R$  is  $\Pr \{Y = 0\} \rightarrow 1$  as  $K_s^R \rightarrow 0$ , and thus a large and increasing fraction of PPM frames are erased. Even  $K_s^R = 1$  in the absence of ECC would result in unacceptable reliability, since in that case an erasure occurs in 37% of PPM frames on average, which is not suitable

for scientific data.<sup>34</sup> A more acceptable erasure probability of  $e^{-K_s^R} \approx 10^{-7}$  can be obtained with  $K_s^R=16$ , but this would result in  $\text{BPP} < 1$  for practical values of  $m$ .

Conceptually we can achieve high BPP (albeit in an impractical way) by manipulating  $m$ . For any value of  $K_s^R$ , even a larger value like  $K_s^R=16$ , (16) indicates that any arbitrarily large BPP can be achieved by choosing  $m$  sufficiently large, because this conveys an increasing number of bits at the expenditure of a fixed number  $K_s^R$  average photon detections. However, this quickly becomes impractical due to a vanishing small slot duration  $T_s$ . For example, if we choose the typical values of  $\text{BPP}=10$  and  $K_s^R=16$ , then we infer from (16) that  $m=160$  is required. To achieve a data rate of  $\mathcal{R}_0=1$  b/s with conventional PPM we must map 160 data bits into a PPM frame with duration 160 s, requiring a slot time of

$$T_s = \frac{160 \text{ s}}{2^{160}} \approx 10^{-34} \text{ ps}, \quad (17)$$

which is, needless to say, far beyond the capability of our electronics.

Although impractical, improving BPP by increasing  $m$  does uncover an important principle. Namely, a way to achieve high photon efficiency coincident with high reliability is to increase the PAR (and consequently the bandwidth) of the signal. This is suggested by the theoretical limit of (3) as well. This principle applies at both radio and optical wavelengths.<sup>35</sup> We now illustrate how efficiency and reliability can be achieved in a practical way by greatly moderating the bandwidth requirement.

### 10.2. Modulation and coding architecture

The theoretical bound of (3) suggests that  $\text{PAR} \sim 2^{10}$  is necessary to achieve  $\text{BPP} \sim 10$  b/ph, a value dramatically lower than would ever be achievable by using a ‘raw’ PPM frame to communicate our data as in (16). A practical architecture achieving this lower PAR is shown in Fig.25. It is organized into layers, with each layer split between coordinated functionality in the transmitter and receiver. This architecture, in conjunction with specific choices for the modulation code and error-correction code (ECC) is not only theoretically solid, but  $\text{BPP}=13$  has been achieved in bench testing (Farr et al. 2013).

The physical layer involves all the physical elements of the downlink, including optical source and detector and transmit and receive apertures. Its input is an intensity-

<sup>34</sup> In the physics literature one occasionally sees an analysis of PPM with  $Y \equiv 1$ , claiming a deterministic number of detected photons and a large resulting value of BPP (see (Hippke 2017b) for an example). This analysis is not valid because it neglects the stochastic nature of quantum photon detection, which at  $K_s^R = 1$  results in an unacceptably large erasure probability.

<sup>35</sup> For the radio case, where the channel model is quite different, this principle is described and quantified in (Messerschmitt 2015).

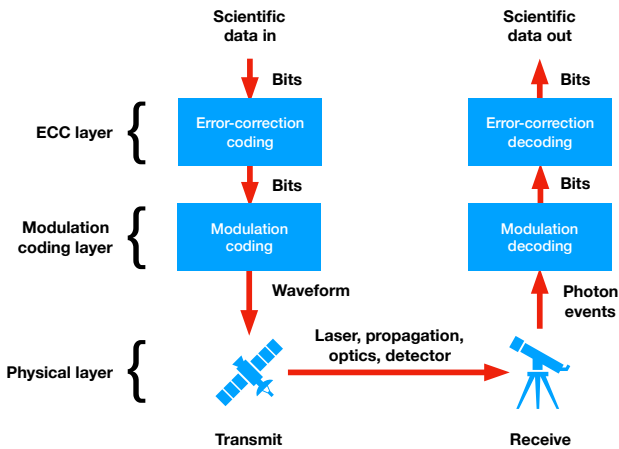


**Figure 25.** Coordinated transmit-receive communications architecture. Functionality is divided into three layers, with each layer divided into a transmit and receive component. Logically each layer in the transmitter is coordinated with its counterpart in the receiver.

vs-time waveform, and its output is a sequence of photon detection events.

The role of the modulation coding layer is to represent discrete data by a continuous-time intensity waveform at the transmitter, and interpret the resulting photon events observed in the receiver in terms of the transmit data (but with poor reliability). For our purposes our modulation code is described by BPPM in Fig.4, which consists of a sequence of PPM frames, each frame representing  $\log_2 M$  bits of data. This simple scheme, operating in conjunction with the ECC layer, allows us to achieve high photon efficiency BPP with high reliability in data recovery.

### 10.3. ECC layer

In contrast to the approach taken in §10.1, the way to achieve a large BPP is to operate the modulation code layer with very poor reliability; that is, choose a small value for  $K_s^R$  (see (18)), which is a photon-starvation mode. The value  $K_s^R=0.2$  chosen in Tbl.2 results in a frame erasure probability  $e^{-0.2}=0.82$ , so approximately 82% of frames are lost to erasures. Although this choice may seem arbitrary, it is further justified in §10.3.4.

The role of the ECC layer is to reconstruct a highly reliable replica of the scientific data. In order to dramatically improve the reliability, the ECC coding layer in the transmitter adds redundancy to the scientific data. In the receiver the ECC decoding layer makes use of this added redundancy (the precise structure of which is known to the receiver) to reconstruct a replica of the scientific data with dramatically improved reliability.

The principle behind the ECC layer can be described abstractly as follows. For BPP=10.9 bits/ph in Tbl.2, each scientific data bit recovery is based on an aver-

age of 0.092 photon detection events. A way (the only way) to achieve reliability in photon-starvation mode is to recover multiple data bits based on a commensurate large number of photon detections, exploiting the law of large numbers to yield less random variability in the number of photon detection events. This can still be accomplished in the context of a PPM modulation coding layer by representing the data bits by pulses with duration  $T_s$ . Thus BPP=10.9 might actually be achieved by exchanging an average of 100 detected photons for 1090 bits. At a data rate of  $\mathcal{R}=1$  b/s this implies an average of 100 photon detection events within 1090 sec (18 minutes), or (almost) equivalently 100 detected pulses on average. There must be  $2^{1090}(\sim 10^{328})$  distinguishable patterns of pulses, one pattern for each possible combination of 1090 bits (compare this to the  $\sim 10^{80}$  atoms in the visible universe). The error-correction decoder examines the random pattern of actual detected pulses, and infers the most likely pattern, and hence the most likely combination of 1090 bits that were represented in the transmitter.

#### 10.3.1. Small codebook example

More concretely, ECC in the context of a PPM modulation coding layer associates  $k > 1$  bits with a group of  $l > 1$  PPM frames, each having  $M = 2^m$  slots. The set of  $2^k$  frame groupings (one for each set of  $k$  inputs bits) is called a *codebook*. Since these  $l$  PPM frames could in principle represent as many as  $lm$  bits, not all the possibilities are included in the codebook as long as  $k < lm$ . This is what we mean by *redundancy*, which can result in dramatically improved reliability by circumventing erasures that have occurred.

This concrete description of the ECC layer can be illustrated as in Fig.26 for three very simple examples. In Fig.26(a)  $k = 1$  bits (2 codewords) are represented in a codebook of  $l = 1$  PPM frame with  $M = 2$  slots, in (b)  $k = 2$  bits (4 codewords) are represented in a codebook of  $l = 2$  PPM frames with  $M = 4$  slots, and in (c)  $k = 4$  bits (16 codewords) are represented in a codebook of  $l = 4$  PPM frames with  $M = 4$  slots. The redundancy in the three cases is zero for (a) and 0.5 for (b) and (c). If the transmit energy per PPM frame remains fixed, the average detected photons per frame has the same value  $K_s^R$  for all cases. Thus, the photon efficiency has the same value ( $\text{BPP} = 1/K_s^R$ ) for all three cases, and thus the probability of a single erasure remains the same.

In Fig.26(a) and (b) all possible erasure events are enumerated (for brevity this is omitted in (c)). In (b) the input data can be inferred even with a single erasure, and data is lost only if there are two erasures. In (c) each pair of codewords agree in at most one PPM frame but disagree in at least three, so one or two erasures (out of a possible four) result in no data loss. We can easily calculate the probability of these events, with the result that for  $K_s = 12$  (BPP = 0.083 b/ph) the probability of data loss is  $6.1 \times 10^{-6}$  for (a),  $3.8 \times 10^{-11}$  for (b), and

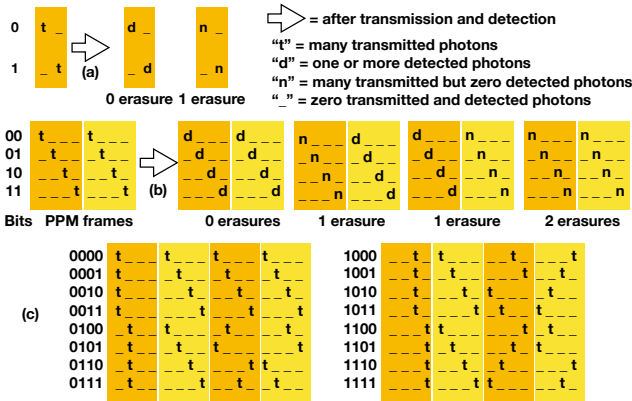


**Figure 26.** An example of the benefits of error-correction coding (ECC) to improve the data-recovery reliability in conjunction with pulse-position modulation (PPM). (a) One scientific data bit is mapped into a single PPM frame with  $M = 2$  slots. The effect of an erasure is shown. (b) Two data bits are mapped into a pair of PPM frames, each with  $M = 4$  slots. The three possible erasure scenarios are shown. (c) Four data bits are mapped into four PPM frames, each with  $M = 4$  slots. Erasure scenarios are not shown. While the photon efficiency is the same in (a), (b), and (c), mapping a larger number of data bits into a larger number of frames results in improved immunity to erasures.

$9.3 \times 10^{-16}$  for (c). The reliability improves dramatically. Increasing the size of the codebook can be beneficial, as in this example, because without any change in BPP the data recovery becomes less susceptible to frame erasures.

### 10.3.2. Theoretical constraint

The photon efficiency for the codebooks displayed in Fig.26 are nowhere near the  $\text{BPP}=10.9$  b/ph that we are seeking. One of the central results of information theory is that under certain conditions the existence of a sequence of ever-larger codebooks is guaranteed, with the desirable property that the probability of data loss decreases to zero. In particular, for the parameters BPP,  $K_s^R$  and  $M$  the condition is (see §F)

$$\text{BPP} < \frac{1 - e^{-K_s^R}}{K_s^R} \cdot \log_2 M < \log_2 M. \quad (18)$$

This is consistent with theoretical bound on (3) presented earlier.<sup>36</sup> This confirms the significance of photon-starvation mode, because BPP in (18) approaches (3) as  $K_s^R \rightarrow 0$  and thus we must choose a very small value of  $K_s^R$  to achieve a BPP near the theoretical maximum for the chosen  $m$ .

<sup>36</sup> The value of BPP assumed in Tbl.5 and in the numerical calculations of §6.8 assume equality in (18). This is recognizably optimistic, but something close to this should be achievable in practice with an appropriate design of ECC accompanied by large processing resources in the receiver.

### 10.3.3. Role of redundancy

We are assured by (18) that photon starvation isn't detrimental to data reliability, as long as ECC overcomes the inherent unreliability at the modulation coding layer. The explanation for this is the inherent redundancy. The average rate of photon detections is  $\mathcal{R}/\text{BPP}$ , and with  $K_s^R$  average photons per PPM frame, the rate of PPM frames is  $\mathcal{R}/K_s^R \cdot \text{BPP}$ . Thus the "raw" bit rate at the input to the modulation coding layer is

$$\frac{m \cdot \mathcal{R}}{K_s^R \cdot \text{BPP}} = \frac{12 \cdot 1}{0.2 \cdot 10.9} = 5.5 \text{ b/s}.$$

Thus, 4.5 b/s of this "raw" bit rate is redundancy, and 1 b/s is scientific data (82 % redundancy and 18% scientific data). According to (18), this redundancy offers a sufficient opportunity to overcome the frequent erasures in PPM frames suffered in the modulation coding layer.

While the theory backing up (18) strongly suggests that a very large ECC codebook is required to obtain high BPP, we have to fall back on best practices in actually choosing such a codebook. For a high SBR, high reliability can be obtained (Farr et al. 2013) using Reed-Solomon coding (Wicker & Bhargava 1999), which is well suited to overcoming frequent erasures.<sup>37</sup> At lower values of SBR more advanced and modern coding techniques have to be adopted, a topic beyond the scope of this paper.

### 10.3.4. Quantum limit

The question arises as to the degree to which the architecture of Fig.25 and the specific choice of PPM for the modulation coding limits performance. Theoretical limits on photon efficiency BPP with reliable data recovery are identified in the Appendices:

- Any physical layer that makes use of electromagnetic transmission is governed by a fundamental quantum limit on reliable data recovery (see §D). This limit is expressed in terms of the photon density PPD (the average number of photons per dimension). There has been some exploration of technologies that may be able to approach this limit (Banaszek et al. 2019b).
- Any physical layer that modulates optical power in the transmitter and performs direct detection (photon counting) in the receiver has, at high SBR, a theoretical limit on BPP with reliable data recovery defined by (3) (see §E).

<sup>37</sup> See (Lubin et al. 2018b) for a description and analysis of Reed-Solomon coding applied to the photon-counting channel using a PPM modulation code. For a laboratory demonstration of high BPP in reliable optical communications, see (Farr et al. 2013). There are also tutorial papers (Lubin et al. 2018b; Messerschmitt 2008) and textbooks (Cover & Thomas 1991; Gallager 2008) that expand on the theoretical basis of ECC.

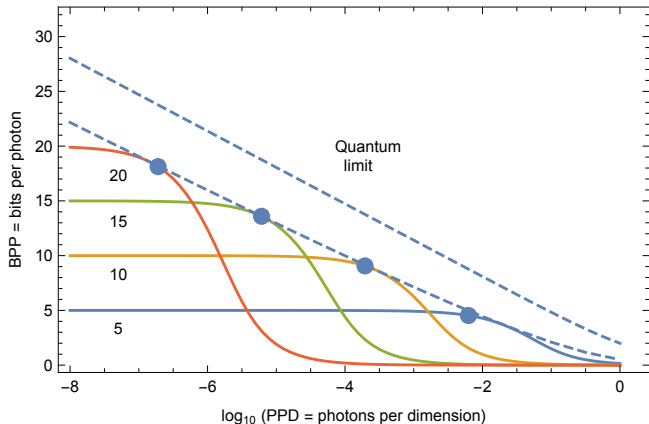


**Figure 27.** A plot of the photon efficiency BPP at the theoretical limit of reliable data recovery (see §F). BPP is plotted against  $\log_{10}(\text{PPD})$ , where PPD is the photon density (average photons per dimension), For PPM we have  $\text{PPD} = K_s/M$ , and PPD is manipulated by varying  $K_s$ . The different curves are for the values  $m \in \{5, 10, 15, 20\}$ , where the number of slots per PPM frame is  $M = 2^m$ . The bottom dashed curve is the largest BPP that can be achieved by PPM (by optimizing the value of  $m$  for each PPD) and the upper dashed curve is the quantum limit on reliable data recovery. The dots correspond to  $K_s = 0.2$ , the nominal value chosen in Tbl.2, which is nearly BPP-maximizing for the  $m$ -range of interest. This displays the gap between PPM and the quantum limit, which shrinks for larger PPD. This gap captures the maximum increase in BPP that may be feasible with future technologies that achieve a more sophisticated manipulation of quantum states.

- The limit of (18) comes arbitrarily close to the photon-counting limit as  $K_s \rightarrow 0$  (see §F).

The shortfall of PPM (and hence photon-counting more generally) to the quantum limit is plotted in Fig.27 (this applies to BPPM equally well). The quantum limit is expressed in terms of PPD, the average photons per dimension, so the BPP for PPM is plotted against the same metric for different values of  $m$ . The specific values of  $\{\text{PPD}, \text{BPP}\}$  for  $K_s = 0.2$  are identified by dots, which fall near the maximum BPP achievable, thus justifying this assumption in Tbl.2 and the previous numerical results.

As  $m$  increases in Fig.27, BPP increases as predicted in (3), since for PPM we have  $\text{PAR} = M$ . The largest BPP achievable by PPM is plotted as the lower dashed curve. Our nominal value  $K_s = 0.2$  approximates this optimum choice. If a larger BPP is desired, it is preferable to increase  $m$  rather than further reduce  $K_s$ .

#### 10.4. Outage mitigation

Outages are characterized by erasures which are not due to signal shot noise, but rather environmental factors experienced by a terrestrial-based receiver such as

sunlight and weather. The data loss due to outages will inevitably reduce the rate at which scientific data is communicated reliably immediately following encounter to  $\mathcal{R}_a < \mathcal{R}_0$ . A simplistic approach to overcoming outages would be to repeat the transmission of scientific data multiple times. We want  $\mathcal{R}_a$  to be as large as feasible, and fortunately there are far more efficient outage mitigation techniques based on a modification to the modulation coding and ECC layers in Fig.25. We can demonstrate theoretical upper limits on  $\mathcal{R}_a$  for a particular statistical model of fully random outages, modify the modulation coding layer to approximate this model, and choose ECC codebooks which come close to these theoretical limits.

##### 10.4.1. Outage characteristics

Outages manifested as frame erasures (rather than frame errors) are simpler to deal with (see §2.12 for the distinction), and since the receiver is aware of daylight and weather conditions it can enforce outages-as-erasures by simply ignoring the received signal during periods of questionable SBR. In this case the receiver will experience daylight and weather outages as contiguous bursts of PPM frame erasures. This distinguishes outage erasures from shot-noise erasures, which are temporally completely random.

##### 10.4.2. Modification to modulation coding layer

In principle the increase in erasure frequency due to outages can be overcome by choosing a more powerful form of ECC. In practice, however, it is very difficult for ECC to deal effectively with temporally highly correlated erasures. Fortunately this challenge can be overcome by adding interleaving to the modulation coding layer as shown in Fig.28a. The interleaver in the transmitter scrambles the order of the bits in the input bit stream, and the de-interleaver in the receiver reverses that operation to recover the original ordering.<sup>38</sup> The modulation-layer decoder outputs a stream of symbols with three possible values  $\{0, 1, E\}$ , where 'E' indicates that this bit is unknown because it experienced an erasure (it was one of  $m$  bits in an erased PPM frame). Whether this erasure was due to shot noise (with probability  $e^{-K_s}$ ) or outages (with probability  $P_W$  for weather and  $P_D$  for daylight) cannot be inferred by the PPM decoder, but nevertheless the knowledge of which bits have suffered an erasure is helpful in the subsequent error-correction decoding.

The interleaver utilizes a deterministic but pseudo-random algorithm with the goal of destroying the correlation of the erasures and make them appear to occur randomly and independently (like a sequence of flips of a

<sup>38</sup> Operating the interleaving and de-interleaving at the bit-level simplifies the following analytical argument. In practice the interleaving may be performed at the PPM frame level.

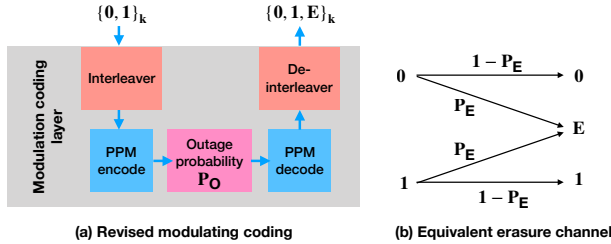


**Figure 28.** Modification to the PPM modulation code layer which converts it to a binary erasure channel. (a) Bit-level interleaving and coordinated de-interleaving convert grouped erasures ‘E’ (due to shot noise, daylight, weather, etc.) into an equal number of pseudo-randomly distributed erasures. The PPM coding/decoding introduces erasures due to shot noise, while the transmission introduces additional erasures due to outages with probability  $P_W$ . (b) Single bit erasure channel with erasure probability  $P_E$ , with transition probabilities  $P_E$  and  $1 - P_E$ . Due to interleaving we assume that successive channel uses are statistically independent.

biased coin). This requires a ‘depth’ of interleaving that is larger than the correlation scale of the frame erasures, which implies longer than the longest outage period (the longest credible weather-outage event). Nominally the number of erasures per error-correction codeword then obeys a binomial probability distribution which is identical for all codewords, yielding a more effective and efficient ECC.

#### 10.4.3. Modification to ECC layer

It is argued in §F.1 that the detected photons per frame  $K_s^R$  and rate of PPM frames  $T_I^{-1}$  should not be changed with the addition of outages. Rather, the reliability of data recovery is theoretically preserved in the presence of outages if the input scientific data rate is reduced from its nominal  $\mathcal{R}_0$  by a factor of  $(1 - P_W)(1 - P_D)$ . That is, the data rate is reduced on average by the fraction of PPM frames that are correctly decoded, which is intuitively the best we could hope for.

Since  $K_s$  should not be changed in response to outages, neither should  $P_P^T A_e^T T_s$ ,  $A_e^S$  or  $N^S$ . Assuming that  $T_I$  is also not changed, neither is the average transmit power  $P_A^T$ . The sole effect of a reduction in data rate to  $\mathcal{R}_a < \mathcal{R}_0$  is an increase in the redundancy in the ECC in order to maintain fixed data-recovery reliability in the face of the added erasures due to outages.<sup>39</sup> Since the data rate is lowered without a reduction in average power, an unsurprising side effect is to reduce the pho-

<sup>39</sup> An example of outage mitigation by means of interleaved ECC is given in (Lubin et al. 2018b), where comparative performance is modeled in the face of different fractions of outage time for a Reed-Solomon ECC code.

ton efficiency BPP by the same factor. Fortunately this has no practical impact for a continuous electrical power source not based on fuel consumption.

If rate  $\mathcal{R}_a$  is unacceptably small, it can always be increased by choosing a larger  $\mathcal{R}_0$ . This of course will have implications throughout the design such as increased average power, increased duty cycle with an attendant increase in the impact of dark counts, etc.

## 11. CONCLUSIONS

The design of a communication downlink from low-mass interstellar probes is extremely challenging. While the downlink violates no laws of physics and appears to be feasible in theory, the challenge arises when the characteristics of available technologies are taken into account. Innovation and invention in both system concepts and in the constituent technologies will be needed.

The primary areas of necessary technology development identified in this paper are:

- Low-mass light sources achieving high peak powers possibly combined with optical pulse compression technology in either transmitter or receiver.
- Low-mass transmit aperture and coordinated attitude adjustment and pointing with sufficient accuracy.
- A feasible multi-probe multiplexing scheme taking into account inaccuracies in the knowledge of time and speed and distance, including Doppler shift.
- Approaches to a near-earth uplink for configuration.
- Optical sub-array possibly incorporating adaptive optics to counter atmospheric turbulence, achieving uniform sensitivity over a relatively large non-circular coverage angle, and with sufficient coronagraph rejection of target star radiation.
- Optical bandpass filters with sufficiently narrow bandwidth, and with agility and configuration capability to accommodate multi-probe multiplexing and uncertainties in Doppler shift.
- Receive optics and optical detectors with very low dark count rates, with possibly detector sharing over multiple sub-arrays.
- Low-mass and low-power processing to realize the requisite compression and error-correction coding on board the probe.

This paper can serve as a roadmap to further investigation and research, and the ultimate outcome depends on the success of those efforts.

PML gratefully acknowledges funding from NASA NIAC NNX15AL91G and NASA NIAC NNX16AL32G

for the NASA Starlight program and the NASA California Space Grant NASA NNX10AT93H, a generous gift from the Emmett and Gladys W. Technology Fund,

as well as support from the Breakthrough Foundation for its StarShot program. More details on the NASA Starlight program can be found at [www.deepspace.ucsb.edu/Starlight](http://www.deepspace.ucsb.edu/Starlight).

## APPENDIX

### A. RELATIVISTIC EFFECTS

Since a low-mass probe travels at relativistic speed, relativistic effects enter.

#### A.1. Transmitter and receiver motion

Assume an inertial frame  $S$  (one approximating a heliocentric coordinate system is convenient). Relative to the trajectory of a photon from probe to receiver, the probe and receiver have a longitudinal component of velocity and a small transverse component (which is neglected). Let the longitudinal components for the probe and a receiver relative to  $S$  be  $u_p$  and  $u_r$ , respectively. The relationship between transmitted wavelength  $\lambda_T$  (observed in the rest frame of the transmitter) and received wavelength  $\lambda_R$  (observed in the rest frame of the receiver) is<sup>40</sup>

$$\xi = \frac{\lambda_R}{\lambda_T} = \frac{\nu_T}{\nu_R} = e(u_p, -1) \cdot e(u_r, +1) \quad (\text{A1})$$

$$e(u, \rho) = \frac{1 - \rho u/c}{\sqrt{1 - u^2/c^2}}. \quad (\text{A2})$$

Thus  $\xi$  is the product of four factors, each of which models a distinct physical effect. The two numerators account for Doppler shifts due to changing propagation delay, while the two denominators model the relativistic time dilations of the transmit and receive clocks. Nearly desired  $\lambda_R$  can be achieved by adjustment of  $\lambda_T$  to compensate for the first factor, while smaller variations in  $u_p$  and  $u_r$  have to be accounted for in other ways (see §8.1.1 and §8.1.2).

##### A.1.1. Probe speed

The systematic red shift due to the nominal probe speed  $u_p = 0.2c$  results in  $\xi = 1.22$  (or a 22% shift). This should be compensated by an adjustment in  $\lambda_T$ . Since the energy of each photon is  $E = hc/\lambda_R$ , the energy of each photon at the receiver is lower than at the probe. Energy seen by an observer in  $S$  is conserved, including this photon energy loss and kinetic energy gains for the probe (the recoil effect) and receiver (photon absorption) (Macleod 2004). The probe transmitter thus acts as a photon engine which continually increases  $u_p$  by a tiny amount. From the perspective of the receive signal,

<sup>40</sup> This relation, including the product law, is derived in (Messerschmitt 2017). Note however that Eq. (17) of that reference is incorrect except at  $\rho = \pm 1$ , with the corrected value given by (A2).

the motion affects wavelength and not photon count, and thus has no effect on the data rate  $\mathcal{R}$  obtainable by a direct-detection receiver.

#### A.2. Uncertainty in probe speed

Assuming that  $u_r = 0$ , based on (A1), any uncertainty in probe speed  $u_p$  relates directly to an uncertainty in received frequency  $\nu_R$ . Differentiating the relation  $\xi\nu_R = \nu_T$  with respect to  $u_p$ , we get

$$\xi \cdot \frac{d\nu_R}{du_p} + \nu_R \cdot \frac{d\xi}{du_p} = 0. \quad (\text{A3})$$

Eq.(14) follows from substituting (A2) in (A3).

### B. ANTENNAS

Certain fundamental principles of antennas or apertures for electromagnetic communication illuminate both opportunities and constraints on our downlink. Our interest here is only in theory that applies to a sub-array, which is where the coverage and the SBR are determined. Our sub-array is assumed to be a diffraction-limited optical aperture with a single optical detector, which is essentially a single-pixel optical telescope. Our receive aperture as a whole is *not* diffraction-limited (it has multiple detectors, and radiation adds incoherently), so the following principles do not apply. However, the coverage and SBR determined at the sub-array level are preserved in the scale-out to  $N$  sub-arrays (see §2.10.2).

#### B.1. Principles

As a consequence of Maxwell's model of electromagnetism, the *reciprocity theorem* states that when one antenna is used for transmission and another for reception, their roles can be reversed without any change to the outcome (see Appendix D of (Wilson et al. 2009)). It is often easier to analyze an antenna in transmit mode, even if it is to be used in receive mode, or *vice versa*.

Suppose a plane wave at wavelength  $\lambda$  and equivalent frequency  $\nu$  has specific intensity  $\mathcal{I}_\nu$  as a function of frequency  $\nu$ , defined as the flux (power per cross-sectional area) per frequency interval (Burke & Graham-Smith 2009). The corresponding intensity in frequency interval  $d\nu$  is  $\mathcal{I}_\nu \cdot d\nu$ . Since the bandwidths of interest are very small for interstellar communication (to eliminate most noise and interference), it is convenient to use  $\nu$  and recognize that any variation in  $\lambda$  can usually be neglected. Thus we assume a fixed wavelength  $\lambda = \lambda_R$ , and simultaneously (and somewhat inconsistently) allow  $\nu$  to vary over a bandwidth  $W_e$ .

For astronomical sources, which can often be considered as isotropic emitters (at least over a finite range of directions of interest) it is often more convenient to use the specific brightness  $\mathcal{B}_\nu$ , which is the power per unit solid angle per frequency interval. At great distances a spherically expanding wave (as from a point source) can be considered a plane wave at the antenna (as long as the difference between a plane and a sphere is a small fraction of a wavelength). In that case, for a spherical wave at a distance  $D$  from the source, the conversion from specific brightness to specific intensity is  $\mathcal{I}_\nu = \mathcal{B}_\nu/D^2$ .

### B.2. Effective area and gain

When a plane wave with specific intensity  $\mathcal{I}_\nu$  impinges on an antenna, we can measure the specific total power  $P_\nu$  delivered to an impedance-matched termination (at radio wavelengths) or an ideal optical detector (at optical wavelengths). The *effective area* of the antenna is defined as  $A_e = P_\nu/\mathcal{I}_\nu$ , which has the units of area.  $A_e$  usually depends strongly on the angle of incidence, and any dependence on  $\nu$  can often be neglected over a small bandwidth  $W_e$ .

Often we are interested in the maximum value of  $A_e$  for the antenna's preferred direction (its "pointing" or "main beam"). For an aperture with geometric area  $A_g$ , in general  $A_e \leq A_g$  with equality when the aperture is diffraction-limited and the direction of propagation of the plane wave is aligned with the pointing.

An isotropic radiator does not favor one direction over another. Its specific brightness  $\mathcal{B}_\nu$  is constant in all directions. For a lossless isotropic radiator and lossless (free-space) propagation, by conservation of energy  $4\pi\mathcal{B}_\nu = P_\nu$ .

The radiation pattern of an antenna of interest is conveniently specified by the ratio of its specific brightness in a particular direction to that of an isotropic radiator with the same power input. This value  $G = 4\pi\mathcal{B}_\nu/P_\nu$  is the *directivity* or *gain* of the antenna in that direction.<sup>41</sup> For a lossless diffraction-limited antenna,  $P_\nu$  equals  $\mathcal{B}_\nu$  integrated over all directions, so

$$P_\nu = \iint \mathcal{B}_\nu \cdot d\Omega \quad \text{or} \quad \frac{1}{4\pi} \iint G \cdot d\Omega = 1. \quad (\text{B4})$$

In words, the gain of any antenna averaged over all solid angles is unity, and identical to the gain of an isotropic radiator in any direction.

It follows from the laws of thermodynamics (Wilson et al. 2009) that for some particular direction, for an antenna with gain  $G$  and effective area  $A_e$  in that direction,

$$G = \frac{4\pi A_e}{\lambda_R^2} \quad (\text{B5})$$

<sup>41</sup> Directivity refers to an ideal antenna, while gain takes any losses in the antenna structure into account. Here we assume an ideal lossless antenna so there is no distinction.

Thus the gain of an antenna (a mostly transmission characteristic) is proportional to effective area (a mostly reception characteristic) expressed in wavelengths. It follows that for an isotropic radiator  $A_e = \lambda_R^2/4\pi$  in all directions.

### B.3. Highly directive antennas

For optical communications and astronomy we are interested in highly directive antennas. Consider an ideal directive antenna that in transmit mode concentrates all its flux uniformly across solid angle  $\Omega_A$  (called its main beam), and there is zero flux outside this solid angle of coverage. Such an antenna is diffraction-limited when the phase shift from optical source to free-space is fixed for all angles within  $\Omega_A$ . Such an antenna used in receive mode has a fixed effective area  $A_e$  for any direction within the main beam. Note that the main beam area need not be circular for this to hold (this is important in our sub-array application).

Then based on (B4) the gain of this antenna is  $G = 4\pi/\Omega_A$ , and substituting into (B5)

$$A_e \Omega_A = \lambda_R^2. \quad (\text{B6})$$

The solid angle covered by this ideal main beam is inversely proportional to effective area, the latter expressed in units of wavelength. As expected, directive antennas with a larger effective area are more directive. This idealized result can be approximated for a practical directive antenna, which introduces sidelobes due to diffraction.

### B.4. Aperture response to different sources

The specific power  $P_\nu$  delivered to a matched termination or absorbent surface by a lossless diffraction-limited aperture is now evaluated for the types of radiation sources of interest in interstellar communication.

#### B.4.1. Interference

Interference from the target star can be approximated as an isotropic point source with constant specific brightness  $\mathcal{B}_\nu$  at all angles. To a receive antenna at great distance  $D_0$  from the target star this will appear as a plane wave with specific intensity  $\mathcal{I}_\nu = \mathcal{B}_\nu/D^2$  and thus

$$P_\nu = A_e \mathcal{I}_\nu = A_e \cdot \frac{\mathcal{B}_\nu}{D^2} \quad (\text{B7})$$

for a receive antenna with effective area  $A_e$  in the direction of the interferer.

#### B.4.2. Probe transmitter

For communications, the optical bandwidth  $W_e$  will always be at least as large as the signal bandwidth. Thus it is more appropriate to leave out the 'specific' in intensity, brightness, and power, and model the total power over all frequencies. At distance  $D$  the average receive

power  $P_A^S$  in a lossless antenna (sub-array) with effective area  $A_e^S$  is

$$P_A^S = \frac{P_A^T}{4\pi} \cdot \frac{4\pi A_e^T}{\lambda_T^2} \cdot \frac{1}{D^2} \cdot A_e^S = \frac{A_e^T A_e^S P_A^T}{\lambda_T^2 D^2} \quad (\text{B8})$$

for transmit antenna with average transmit power  $P_A^T$  and effective area  $A_e^T$ , confirming (5). The four product terms in (B8) are (1) the brightness of the transmitter if its radiation were isotropic, (2) the transmit antenna gain, (3) the translation from brightness to intensity at the receiver, and (4) the receive aperture equivalent area (which converts intensity to power). This is the well-known Friis transmission equation (Schelkunoff & Friis 1952).

Although the transmit and receive wavelengths  $\lambda_T$  and  $\lambda_R$  differ substantially due to Doppler shift (see §A.1),  $P_R$  in (B8) is not dependent on  $\lambda_R$ .

#### B.4.3. Noise

Finally consider noise due to unresolved sources of radiation. From the perspective of the receive antenna, we can consider this to be an isotropic source of radiation. In practice the radiation is never fully isotropic, because it is limited in extent (like Zodiacal radiation in a distant solar system) or is not fully visible to a terrestrial antenna (due to occlusion by the ground). However, if the antenna is highly directional, and its coverage coincides with radiation that is well approximated as uniform with direction, then the isotropic model should be accurate.

Isotropic radiation has constant specific brightness  $\mathcal{B}_\nu$ . For an antenna with gain  $G$  as a function of direction, the received power is

$$P_\nu = \iint G \mathcal{B}_\nu \cdot d\Omega = \mathcal{B}_\nu \cdot \iint G \cdot d\Omega = 4\pi \mathcal{B}_\nu \quad (\text{B9})$$

making use of (B4). The received specific power is independent of the antenna effective area. This is why we can meaningfully speak of a CMB ‘noise temperature’ at microwave frequencies without referring to  $A_e^S$ .

A couple of special cases are of interest. First, if the isotropic specific brightness  $\mathcal{B}_\nu$  were actually generated by an isotropic radiator with power  $P_\nu$ , then we know that  $G \equiv 1$  and  $\mathcal{B}_\nu = P_\nu/4\pi$  consistent with (B9). Second, if a highly directive antenna receives isotropic radiation, then (B9) becomes

$$P_\nu = \iint_{\Omega_A} \frac{4\pi}{\Omega_A} \cdot \mathcal{B}_\nu \cdot d\Omega = 4\pi \mathcal{B}_\nu. \quad (\text{B10})$$

In this case  $P_\nu$  is independent of  $\Omega_A$  (and hence effective area  $A_e$ ) because the total noise power due to the size of the main beam and the gain within that main beam precisely offset.

An alternative interpretation of this last observation is that the received power is proportional to  $A_e^S$  (the conversion factor of input flux to power at the detector)

and also  $\Omega_A$  (the fraction of total isotropic power reaching the detector) (see Eq. (8.76) of (Piazzolla 2009)). This product  $A_e^S \Omega_A$  is constant for a diffraction-limited highly directive antenna (based on (B6)).

#### C. DATA VOLUME VS. LATENCY

Let  $D_0$  be the distance to the target star and  $D > D_0$  the distance to the probe. The total latency (elapsed time since launch) for data transmitted from distance  $D$  is

$$T_L = D \left( \frac{1}{u_0} + \frac{1}{c} \right) \quad (\text{C11})$$

for fixed probe speed  $u_0$ . The terms in (C11) are respectively the elapsed time  $t$  for the probe to reach distance  $D$ , and a photon emitted at distance  $D$  to return to the receiver, both measured relative to the rest frame of the receiver.

The appropriate data rate  $\mathcal{R}$  for purposes of data volume is the transmitted data rate (11). The total data volume transmitted between distance  $D_0$  and  $D$  is

$$\mathcal{V} = \int_{D_0/u}^{D/u} \mathcal{R}(\zeta, u_0 t) dt = \frac{\mathcal{R}_0 D_0}{u_0} \cdot \left( 1 - \frac{D_0}{D} \right). \quad (\text{C12})$$

This entire  $\mathcal{V}$  is decoded at the receiver during time duration  $T_L$ . Eliminating  $D$  from (C11) and (C12), the latency can be expressed directly in terms of the volume,

$$T_L = \frac{D_0}{u_0} + \frac{D_0 \mathcal{V}}{D_0 \mathcal{R}_0 - u_0 \mathcal{V}} + \frac{D_0^2 \mathcal{R}_0}{c(D_0 \mathcal{R}_0 - u_0 \mathcal{V})} \quad (\text{C13})$$

where the three terms are the transit time, the transmission time, and the return propagation time all expressed in terms of an earth-based clock. After substituting for  $\mathcal{R}_0$  and  $u_0$  in terms of  $\zeta$  (see §3), this latency can be minimized over the choice of  $\zeta$ .

For any  $\mathcal{R}_0$ ,  $\mathcal{V}$  approaches a finite asymptote  $\mathcal{V} \rightarrow \mathcal{R}_0 D_0 / u_0$  as  $D \rightarrow \infty$ . This ultimate limit on volume with infinite latency is due to the decreasing data rate with distance. Larger  $\mathcal{R}_0$  and a smaller  $u_0$  help to increase  $\mathcal{V}$ , the latter effect due to the slower  $D$ -related falloff in  $\mathcal{R}$ .

There will also be a small reduction in available electrical power during transmission (due for example the half life of a radioactive source), and this is not taken into account in (C12).

#### D. QUANTUM LIMIT ON DATA RELIABILITY

The actual design of a concrete ECC for the photon-counting channel will not be pursued here, because ECC design is itself an extensive and sophisticated project. An example of carrying out a concrete ECC design is given in our tutorial (Lubin et al. 2018b) for the interested reader. Nevertheless it is important to determine how large a BPP consistent with reliable data recovery might be expected, and also quantify how larger BPP

relates to larger PAR and bandwidth  $W_e$  because those two parameters interact strongly with other aspects of the downlink design.

### D.1. Channel model

A given physical configuration is not generally associated with a theoretical limit on the data rate  $\mathcal{R}$ , because we must also specify other details of the physical layer such as aperture sizes and detection method before such a limit can be established. Any theoretical limit is associated with a specific *statistical channel model*, which specifies, for each possible input (typically a continuous-time or discrete time signal), a probability distribution of the output. Here we find it useful to address three such models: the quantum limit (see §D.3), direct-detection of light (see §E), and direct-detection in conjunction with a PPM modulation layer (see §F).

### D.2. Channel capacity

Communication theory offers a way to establish a theoretical limit on the photon efficiency BPP which can be achieved consistent with reliable data recovery through the concept of *channel capacity*  $\mathcal{C}$ . Channel capacity can be calculated (using statistical techniques beyond our scope) for any specific channel model. A channel model can be discrete-time or continuous time, with any combination of discrete or continuous inputs or outputs. Channel capacity does *not* place a limit on the data rates that can be achieved (see §10.1). What it does reveal is a theoretical limit on what data rate  $\mathcal{R}$  can be achieved with arbitrarily high reliability, applying to the specific channel model in question. The associated photon efficiency is easily inferred from  $\text{BPP} = \mathcal{C} / \Lambda_A^R$ . In particular, capacity reveals that:

- For any  $\mathcal{R} < \mathcal{C}$ , a modulation code and ECC is guaranteed to exist that can achieve data rate  $R$  in conjunction with any arbitrarily stringent reliability requirement. Channel capacity does not reveal any concrete way to achieve  $\mathcal{R} \rightarrow \mathcal{C}$ , as that is an entirely separate issue.<sup>42</sup>
- The existence of capacity does not preclude  $\mathcal{R} \geq \mathcal{C}$  for some concrete implementation, for arbitrarily large  $\mathcal{R}$ . However it asserts that high reliability cannot be achieved at such data rates. Generally the highest achievable reliability will deteriorate as  $\mathcal{R}$  increases.

Capacity is very useful as a tool in the preliminary design of a communication link because it represents an ideal to shoot for; that is, what BPP is possible for reliable data transmission. Also it tells us, for any concrete

<sup>42</sup> Based on decades of research it is generally possible to narrow the gap between  $\mathcal{R}$  and  $\mathcal{C}$ , although attempting to do so may be impractical (due to complexity, storage and processing overhead, PAR, bandwidth, etc.)

implementation, how much further improvement may be possible with the application of additional effort and resources.

### D.3. Holevo capacity

For optical communications, the most general channel model assumes that the transmitter and receiver can manipulate an arbitrarily large number of quantum states directly and simultaneously. The resulting *Holevo capacity* establishes a technology-independent theoretical limit on the data rate that can be achieved with reliable data recovery (Holevo 1998). Since we cannot avoid the randomness inherent in quantum mechanics in any physically meaningful way, Holevo capacity represents an ultimate and theoretical limit to aspire to, and reveals what future progress may be feasible with new technologies not available to us today. Recent research is making some inroads in approaching the Holevo limit (Guha 2011).

PPM makes use of a repeated transmission of PPM frames, each composed of  $M$  timeslots of duration  $T_s$ . Thus it uses temporal modes only (avoiding the use of wavelength, spatial, and polarization modes to convey information). For a fair comparison with Holevo capacity we also limit the Holevo capacity to temporal quantum modes making use of timeslots with the same duration  $T_s$ . Then for average power  $\Lambda_A^R$  the average photon count per timeslot is  $\text{PPD} = T_s \Lambda_A^R$ . The photon efficiency BPP at the Holevo quantum limit is then (Dolinar et al. 2012a)

$$\text{BPP} = (1 + 1/\text{PPD}) \cdot \log_2(\text{PPD} + 1) - \log_2(\text{PPD}). \quad (\text{D14})$$

Of course this must be greater than either the BPP achievable by a direct-detection receiver (see §E) or PPM (see §F). This applies in the absence of background radiation, which suffices for our purposes.

## E. THEORETICAL LIMITS ON DIRECT DETECTION

A practical channel model for today's technology is modulation of optical intensity in the transmitter and direct detection of photons in the receiver.

### E.1. Constraints

If we allow infinite transmit power, any data rate  $\mathcal{R}$  can be achieved reliably. To get practically meaningful results, we must place constraints on the received power. Assume that the intensity (average photons per second) over a finite interval  $T_c$  is  $\Lambda_n(t)$ , which we can think of as a codeword. These are the peak power  $\Lambda_P^R$  and average power  $\Lambda_A^R$  constraints

$$0 \leq \Lambda_n(t) \leq \Lambda_P^R, \quad 0 \leq t \leq T_c$$

$$\frac{1}{T_c} \int_0^{T_c} \Lambda_n(t) \cdot dt = \Lambda_A^R, \quad 1 \leq n \leq N_c.$$

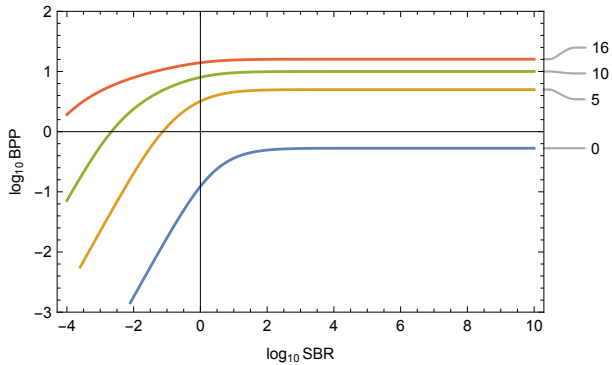


**Figure 29.** For a continuous-time photon-counting channel, a log-log plot of BPP vs SBR with the different curves corresponding to different values of PAR. The curves are labeled by  $\log_2 \text{PAR}$ , so for example 16 corresponds to  $\text{PAR} = 2^{16} = 65,536$ . The axis  $\log_{10} \text{BPP} = 0$  corresponds to a photon efficiency of 1 b/ph. The axis  $\log_{10} \text{SBR} = 0$  corresponds to equal average signal and background power.

We make two simplifying assumptions which have no effect on the capacity  $\mathcal{C}$ . First, each and every codeword is constrained to have the same energy  $T_c \Lambda_A^R$ . Also, every codeword has an ON-OFF character ( $\Lambda_n(t) = \Lambda_P^R$  or  $\Lambda_n(t) = 0$  for  $0 \leq t \leq T_c$ ). Photon rates  $\{\Lambda_A^R, \Lambda_P^R\}$  are referenced to the detector output, taking account of everything that happens in the physical layer (including quantum efficiency). Also assume that there is a fixed background rate  $\Lambda_B$ , and define  $\text{PAR} = \Lambda_P^R / \Lambda_A^R$  and  $\text{SBR} = \Lambda_A^R / \Lambda_B$ .

### E.2. Capacity result

The direct-detection channel is modeled by photon detection events governed by Poisson arrival statistics. This is the most random arrival process, in which inter-arrival times are statistically independent and obey an exponential distribution. The capacity has been determined for this statistical model under the peak and average power constraints described in §E.1. Define two parameters

$$s = \frac{1}{\text{PAR} \cdot \text{SBR}}, \quad q = \min \left\{ \frac{1}{\text{PAR}}, \frac{(1+s)^{1+s}}{e s^s} - s \right\},$$

and then (Wyner 1988)

$$\frac{\mathcal{C}}{\Lambda_A^R} = \text{BPP} = \text{PAR} \cdot \log_2 \frac{(1+s)^{q(1+s)} s^{(1-q)s}}{(q+s)^{q+s}}. \quad (\text{E15})$$

In the limit as  $\text{SBR} \rightarrow \infty$  (or equivalently  $s \rightarrow 0$ ), (E15) simplifies to (yielding (3) for  $\text{PAR} > e$ )

$$\begin{aligned} \text{BPP} &\rightarrow -\text{PAR} \cdot q \log_2 q \\ q &\rightarrow \min \{1/\text{PAR}, 1/e\}. \end{aligned} \quad (\text{E16})$$

### E.3. BPP is unbounded

Notably the capacity  $\mathcal{C}$  is unbounded even for finite average power,

$$\text{BPP} \rightarrow \infty \text{ as } \text{PAR} \rightarrow \infty \text{ for any } \text{SBR} < \infty. \quad (\text{E17})$$

This confirms that a PAR constraint is necessary to prevent infinite BPP, and more importantly indicates that increasing  $\Lambda_P^R$  increases BPP and  $\mathcal{C}$  even as  $\Lambda_A^R$  is held constant. The uncertainty principle will intervene at very high PAR (Butman et al. 1982; Hippke 2018) to render our channel model physically unrealizable.

### E.4. Effect of background radiation

A log-log plot of BPP vs SBR is shown in Fig.29 over a wide range (14 orders of magnitude) of SBR. The value of BPP is nearly constant with the value (3) for large SBR. In the region of low SBR, the highest achievable BPP falls off rapidly. This is clearly a region to be avoided by choosing a sufficiently large transmit power  $P_A^T$ . Notably even in the regime of low SBR, the background can still be overcome by choosing a sufficiently large PAR.

## F. THEORETICAL LIMITS ON PULSE-POSITION MODULATION

Constraining the implementation to the concrete architecture of Fig.25 must necessarily reduce the capacity relative to the direct detection model of §E, which does not constrain the modulation code in any way. We can ascertain the adverse effect of choosing a particular modulation code by associating a new bits-in to bits-out channel model with the modulation code-in to modulation code-out. In the case of PPM this new channel model has bits-in and bits-plus-erasures-out, with an erasure probability  $e^{-K_s}$ . The resulting theoretical limit on reliable data recovery is well known to be (18) (Butman et al. 1982).

One distinction between PPM and the assumptions behind the Holevo capacity is that the  $K_s$  average photons are all isolated in a single timeslot per frame rather than allowed to fall in the available dimensions in any pattern. The other distinction is the direct manipulation of quantum states allowed in Holevo, which lacks a practical realization in today's technology.

### F.1. Effect of outages

The idea of using a de-interleaver to randomize the temporal statistics of outages was introduced in Fig.28a, and for theoretical convenience assumes that erasures occur at the bit level (although in practice they may well occur at the PPM frame level). An ideal *erasure channel* is pictured in Fig.28b. It models a statistical relationship between input bits  $\{0, 1\}$  and output symbols  $\{0, 1, E\}$  in terms of a set of transition probabilities, where  $P_E$  is the probability of a single bit-level erasure (which equals the probability of a PPM frame erasure).

Further, it is assumed that the individual symbols in Fig.28b are statistically independent, a condition that is strongly violated with PPM frame erasures or outages, but that a well-designed interleaver can approximate.

The capacity  $C_u$  of the ideal erasure channel of Fig.28b is well known to be  $C_u = (1 - P_E)$  per channel use, or

$$C_u = (1 - P_E) = (1 - e^{-K_s}) \cdot (1 - P_W) \cdot (1 - P_D)$$

where  $K_s$  is the average detected photons per PPM frame. This assumes that the three sources of erasures (shot noise, weather, and daylight) are statistically independent. Weather outages and daylight may be correlated, in which case  $C_u$  can be adjusted accordingly.

The rate of channel uses in Fig.28b as a model for Fig.28a is  $m/T_I$ , and thus the capacity of the modulation coding layer is  $mC_u/T_I$ . Relative to the case of no outages, this capacity is reduced by a factor of  $(1 - P_W)(1 - P_D)$ , and thus the data rate  $\mathcal{R}_0$  has to

be reduced by the same factor to ensure that reliable data recovery remains possible. Since the average photon detection rate is  $K_s/T_I$ , the upper bound on BPP is changed to

$$\text{BPP} < m \cdot (1 - P_W) \cdot (1 - P_D) \cdot \frac{1 - e^{-K_s}}{K_s}. \quad (\text{F18})$$

This is consistent with (18) for the case  $P_W = P_D = 0$ . As in the outage-free case, for a fixed value of  $m$  the greatest photon efficiency is obtained as  $K_s \rightarrow 0$ , and there is no motivation to modify  $K_s$  to account for outages.

The foregoing is a theoretical limit on  $C_u$  and BPP. For any specific choice of a class of error-correction codes (such as the Reed-Solomon codes), it is appropriate to minimize the error rate by the choice of  $K_s$  and  $T_I$  taking into account the characteristics of this particular code. In this context there may be some dependence of  $K_s$  on  $P_W$  and  $P_D$ .

## REFERENCES

- Abramson, N. 1994, Proceedings of the IEEE, 82, 1360
- Atwater, H. A., Davoyan, A. R., Ilic, O., et al. 2018, Nature materials, 1
- Banaszek, K., & Jachura, M. 2017, in 2017 IEEE International Conference on Space Optical Systems and Applications (ICSOS) (IEEE), 34–37
- Banaszek, K., Jachura, M., & Wasilewski, W. 2019a, in International Conference on Space Optics, Vol. 11180, International Society for Optics and Photonics, 111805X
- Banaszek, K., Kunz, L., Jarzyna, M., & Jachura, M. 2019b, in Free-Space Laser Communications XXXI, Vol. 10910 (International Society for Optics and Photonics), 109100A
- Biswas, A., & Piazzolla, S. 2006, The atmospheric channel, ed. H. Hemmati (John Wiley and Sons)
- Burke, B., & Graham-Smith, F. 2009, An introduction to radio astronomy (Cambridge University Press)
- Butman, S., Katz, J., & Lesh, J. 1982, IEEE Transactions on Communications, 30, 1262
- Cash, W. 2011, The Astrophysical Journal, 738, 76
- Cover, T., & Thomas, J. 1991, Elements of Information Theory (New York: John Wiley and Sons)
- Dolinar, S., Erkmen, B., Moision, B., Birnbaum, K., & Divsalar, D. 2012a, in Information Theory Proceedings (ISIT), 2012 IEEE International Symposium on (IEEE), 541–545
- Dolinar, S., Moision, B., & Erkmen, B. 2012b
- Farr, W. H., Choi, J. M., & Moision, B. 2013, in Free-Space Laser Communication and Atmospheric Propagation XXV, Vol. 8610 (International Society for Optics and Photonics), 861006
- Forgan, D. H., Heller, R., & Hippke, M. 2017, Monthly Notices of the Royal Astronomical Society, 474, 3212
- Forward, R. L. 1962, Missiles and Rockets, 10, 26
- Fountain, G., Kusnierkiewicz, D., Hersman, C., et al. 2009, The New Horizons spacecraft, New Horizons (Springer), 23–47
- Gallager, R. G. 2008, Principles of digital communication (Cambridge, UK: Cambridge University Press)
- Gordon, J. P. 1962, Proceedings of the IRE, 50, 1898
- Gros, C. 2017, Journal of Physics Communications, 1, 045007
- Guha, S. 2011, Physical Review Letters, 106, 240502
- Hausser, M., Arendt, R. G., Kelsall, T., et al. 1998, The Astrophysical Journal, 508, 25
- Heller, R. 2017a, Monthly Notices of the Royal Astronomical Society, 470, 3664
- . 2017b, Monthly Notices of the Royal Astronomical Society
- Heller, R., & Hippke, M. 2017a, The Astrophysical Journal Letters, 835, L32
- . 2017b, The Astrophysical Journal Letters, 835, L32
- Heller, R., Hippke, M., & Kervella, P. 2017, The Astrophysical Journal, 154, 115
- Hemmati, H. 2006, Deep space optical communications, Vol. 11 (John Wiley & Sons)
- . 2009, Near-earth laser communications (CRC press)

- Hippke, M. 2017a, arXiv preprint arXiv:1706.03795
- . 2017b, arXiv:1712.05682
- . 2018, arXiv preprint arXiv:1801.06218
- Hoang, T. 2017, *The Astrophysical Journal*, 847, 77
- Hoang, T., Lazarian, A., Burkhart, B., & Loeb, A. 2017, *The Astrophysical Journal*, 837, 5
- Hoang, T., & Loeb, A. 2017, *The Astrophysical Journal*, 848, 31
- Holevo, A. S. 1998, *IEEE Transactions on Information Theory*, 44, 269
- Jarzyna, M., Zwoliński, W., Jachura, M., & Banaszek, K. 2018, in *Free-Space Laser Communication and Atmospheric Propagation XXX*, Vol. 10524, International Society for Optics and Photonics, 105240A
- Kafka, J., & Baer, T. 1987, *Optics letters*, 12, 401
- Kulkarni, N., Lubin, P., & Zhang, Q. 2017, arXiv:1710.10732 [astro-ph.IM]
- Landis, G. 2019, in *Tennessee Valley Interstellar Symposium*, Wichita, KN
- Lubin, P. 2016
- . 2020, *The Path* (World Scientific)
- Lubin, P., Brashears, T., & Knowles, P. 2018a, *The Path - Directed Energy for Interstellar and Rapid Interplanetary Missions*
- Lubin, P., Messerschmitt, D., & Morrison, I. 2018b, to appear
- Lubin, P., Messerschmitt, D. G., & Morrison, I. 2018c, arXiv preprint arXiv:1801.07778
- Ludwig, R., & Taylor, J. 2016, *Voyager telecommunications* (John Wiley and Sons, Inc)
- Macleod, A. 2004, *Redshift and Energy Conservation*
- Messerschmitt, D., Lubin, P., & Morrison, I. 2019, in *Tennessee Valley Interstellar Symposium*, Wichita, KN
- Messerschmitt, D. G. 2008, *Some Digital Communication Fundamentals for Physicists and Others*, Tech. Rep. UCB/EECS-2008-78, EECS Department, University of California, Berkeley. [www2.eecs.berkeley.edu/Pubs/TechRpts/2008/EECS-2008-78.pdf](http://www2.eecs.berkeley.edu/Pubs/TechRpts/2008/EECS-2008-78.pdf)
- . 2013, End-to-end interstellar communication system design for power efficiency, Tech. Rep. arxiv:1305.4684
- . 2015, *Acta Astronautica*, 107, 20
- . 2017, *Proc. IEEE*, 105, 1511, doi: [10.1109/JPROC.2017.2717980](https://doi.org/10.1109/JPROC.2017.2717980)
- Moision, B., & Farr, W. 2014, Range dependence of the optical communications channel, Tech. Rep. 42-199, NASA IPN. [tmo.jpl.nasa.gov/progress\\_report/42-199/199B.pdf](http://tmo.jpl.nasa.gov/progress_report/42-199/199B.pdf)
- Parkin, K. 2018, *Acta Astronautica*, 152, doi: [10.1016/j.actaastro.2018.08.035](https://doi.org/10.1016/j.actaastro.2018.08.035)
- Parkin, K. 2019, in *International Astronautical Congress*, Washington, DC
- Piazzolla, S. 2009, *Atmospheric channel*, ed. H. Hemmati (CRC Press)
- Roh, W., Seol, J.-Y., Park, J., et al. 2014, *IEEE communications magazine*, 52, 106
- Schelkunoff, S., & Friis, H. 1952, *Antennas: theory and practice*, Vol. 639 (Wiley New York)
- Shibata, H., Shimizu, K., Takesue, H., & Tokura, Y. 2015, *Optics Letters*, 40, 3428
- Slepian, D., & Pollak, H. 1961, *Bell System Technical Journal*, 40, 43
- Smith, B. A., Soderblom, L. A., Banfield, D., et al. 1989, *Science* (New York, N.Y.), 246, 1422
- Spencer, D. T., Bauters, J. F., Heck, M. J., & Bowers, J. E. 2014, *Optica*, 1, 153
- Spencer, D. T., Tang, Y., Bauters, J. F., Heck, M. J., & Bowers, J. E. 2012, in *Photonics Conference (IPC)*, 2012 IEEE (IEEE), 141–142
- Toyoshima, M., Leeb, W., Kunimori, H., & Takano, T. 2007, *Optical engineering*, 46, 015003
- Traub, W. A., & Oppenheimer, B. R. 2010, *Direct imaging of exoplanets*, ed. S. Seager, *Exoplanets* (University of Arizona Press), 111–156
- Treacy, E. 1969, *IEEE Journal of quantum Electronics*, 5, 454
- Wicker, S. B., & Bhargava, V. K. 1999, *Reed-Solomon codes and their applications* (John Wiley and Sons)
- Wikipedia contributors. 2019, *Sunshine duration* — Wikipedia, The Free Encyclopedia. [en.wikipedia.org/wiki/Sunshine\\_duration](https://en.wikipedia.org/wiki/Sunshine_duration)
- Wilson, T. L., Rohlfs, K., & Huttemeister, S. 2009, *Tools of radio astronomy*, Vol. 5 (Springer)
- Wyner, A. D. 1988, *IEEE Transactions on Information Theory*, 34, 1449
- Zwolinski, W., Jarzyna, M., & Banaszek, K. 2018, *Optics express*, 26, 25827